

SEARCH FOR SUPERSYMMETRY
IN TRIMUON FINAL STATES
WITH THE CMS DETECTOR

Zur Erlangung des akademischen Grades eines
DOKTORS DER NATURWISSENSCHAFTEN
an der Fakultät für Physik des
Karlsruher Instituts für Technologie (KIT)

genehmigte

DISSERTATION

von

Dipl.-Phys. Martin Florian Niegel
aus Karlsruhe

Tag der mündlichen Prüfung: 18.12.2009

*Referent: Prof. Dr. W. de Boer
Institut für Experimentelle Kernphysik*

*Korreferent: Prof. Dr. G. Quast
Institut für Experimentelle Kernphysik*

*Wie kann es sein, dass die Mathematik,
die ein von der Existenz unabhängiges Produkt des menschlichen Denkens ist,
so bewundernswert an die wirklichen Dinge angepasst ist?*

Albert Einstein

Contents

1	Introduction	3
2	SUSY	7
2.1	Standard Model	7
2.1.1	Lagrangians	8
2.1.2	Gauge Invariance	9
2.1.3	Lagrangian of the Standard Model	10
2.1.4	Higgs Mechanism	13
2.2	Motivation for Supersymmetry	17
2.2.1	Frontiers of the Standard Model	17
2.2.2	Aspects of Grand Unified Theories	18
2.2.3	Aspects of Supersymmetry	20
2.3	Supersymmetry	21
2.3.1	Particle Spectrum	22
2.3.2	Lagrangian of the MSSM	22
2.3.3	SUSY Mass Spectrum	25
2.3.4	Experimental Constraints	29
3	LHC and the CMS-Experiment	35
3.1	Large Hadron Collider	35
3.2	CMS Experiment	37
3.2.1	Coordinate System	39
3.2.2	Inner Tracking System	41
3.2.3	Electromagnetic Calorimeter	42
3.2.4	Hadron Calorimeter	44
3.2.5	Magnet	45
3.2.6	Muon System	45
3.2.7	Trigger and Data Acquisition	46
3.2.8	CMS Computing Model	47
4	Event Reconstruction and Software Tools	49
4.1	CMS Software Framework	49
4.2	Event Generation	50

4.3	Reconstruction of Physics Objects	52
4.3.1	Muons	52
4.3.2	Jets	54
4.3.3	Missing Transverse Energy	56
4.4	Software Tools	58
5	Trimuon SUSY Search	59
5.1	Trimuon SUSY Signal	59
5.1.1	SUSY Particle Production	60
5.1.2	Prompt Muons in SUSY Particle Decays	61
5.1.3	Trimuon Signature	66
5.2	Standard Model Background	71
5.3	Monte Carlo Datasets	75
5.4	Muon Selection	78
5.4.1	Muon Identification	78
5.4.2	Prompt Muons	79
5.4.3	Fake Muons	80
5.4.4	Fake and Prompt Reference Samples	82
5.4.5	Optimization of the Selection	84
5.5	Trimuon Event Selection	91
5.6	Trigger	96
5.7	Systematic Uncertainties	96
5.8	Data-Driven Background Estimation	98
5.8.1	ABCD Method	99
5.8.2	Z-Candle Method	106
5.8.3	Summary	107
5.9	Discovery Reach	108
5.9.1	Comparison with Tevatron Results	110
5.10	Prospects of an Extended Selection	111
6	Conclusion	117
A	Track Reconstruction Performance	119
B	SUSY Particle Decay Modes	121
	Bibliography	123

Chapter 1

Introduction

The Standard Model (SM) of particle physics has proven to be very successful in describing a large variety of data ranging over many decades of energy. All particles proposed by the SM have been discovered so far, except for the Higgs boson, a scalar neutral particle. The Higgs field is expected to be responsible for the mass of elementary particles. The search for the Higgs boson is one of the major reasons for the construction of the Large Hadron Collider (LHC) and the design of the two general purpose detectors at the LHC, ATLAS and CMS [1,2]. From electroweak precision measurements the mass of the SM Higgs boson has been constrained to a region between $114 < m_H < 194$ GeV at 95% confidence level [3].

There are a few aspects sneaking suspicion that the SM is not the whole story. A problem is the so-called fine tuning problem of the Higgs mass, where self energy corrections of fermions to the Higgs field would naturally tend to make the mass of the Higgs boson much larger than the experimentally observed limits. In order to keep the corrections small, the SM can be only valid up to a finite cut-off scale $\Lambda \sim \mathcal{O}(\text{TeV})$, see e.g. [4]. Furthermore, the SM provides no particles with the right properties to form the dark matter that seems to provide more than 80% of the matter in the universe [5].

A theoretical concept addressing both of these issues is supersymmetry (SUSY), see e.g. [6–11]. Supersymmetry is a symmetry between fermions and bosons, so for each SM particle with spin(j) a SUSY partner with spin($j \pm 1/2$) exists: neutralinos and charginos are the spin(1/2) partner of the neutral and charged gauge bosons and the Higgs bosons, squarks and sleptons are the spin(0) partner of quarks and leptons, respectively, and gluinos are the spin(1/2) partner of gluons. Since experiments have not yet seen any sign of those particles, they are supposed to be heavier than their SM partners. SUSY is an elegant way to solve the fine tuning problem, since opposite sign amplitudes of fermions and bosons in the Higgs self energy corrections cancel each other naturally. The lightest SUSY particle (LSP) is stable, massive and only interacting via gravity and the weak force, thus forming an ideal candidate for explaining the dark matter in the universe. Additionally, in SUSY the spontaneous electroweak symmetry breaking is not assumed ad-hoc as in the SM, but can be induced by radiative corrections, see e.g. [6–11]. Furthermore, SUSY paves the

way for a unification of all forces, since only if the SUSY particles are included in the running of the electroweak and strong coupling constants one obtains unification at about 10^{16} GeV [12].

Apart from searching for the Higgs boson, the search for SUSY or other physics beyond the SM is an additional goal of the LHC. In the low mass SUSY region close to the current limits the cross section of the total SUSY production is tiny compared to the total cross section of the SM processes: $\sigma_{\text{SUSY}} < 10^{-9}\sigma_{\text{SM}}$. Therefore the challenge of searching for SUSY is to distinguish the rare SUSY events from the huge amount of SM background processes. SUSY events can be distinguished by large missing transverse energies (MET), caused by the LSPs which escape detection, and/or by large lepton and jet multiplicities above SM expectations, eventually combined with kinematic edges in the invariant mass spectra.

At the LHC, supersymmetric particles are dominantly produced in strong interaction processes, thus the production of gluinos and squarks ($pp \rightarrow \tilde{g}\tilde{g}, \tilde{g}\tilde{q}, \tilde{q}\tilde{q}$) carries the major fraction of the total SUSY cross section, if kinematically accessible. Neutralino-chargino pairs can be produced directly in the electroweak process $pp \rightarrow \chi_2^0\chi_1^\pm$ and independently in cascade decays of squarks and gluinos. Leptonic decays of neutralinos ($\chi_2^0 \rightarrow l\bar{l}\chi_1^0$) and charginos ($\chi_1^\pm \rightarrow l\nu\chi_1^0$) are the main source of isolated prompt leptons in SUSY events. The production of pairs of a neutralino χ_2^0 and a chargino χ_1^\pm both decaying subsequently to leptons form the trilepton signature. The direct neutralino-chargino production corresponds to the trilepton signature without hard jets and with some missing transverse energy from the escaping LSPs and neutrinos, while in the decays of squarks and gluinos the trilepton signature is accompanied by hard jets.

The trilepton signature is sometimes called the *golden* signature, because of the small intrinsic background from SM processes. In the SM isolated leptons are mostly produced by leptonic decays of gauge bosons ($Z/\gamma, W^\pm$). The larger the number of leptons in the final state, the smaller the SM background. For the trilepton final state there are a few SM channels with small but not negligible cross sections which produce three or more isolated prompt leptons: $pp \rightarrow ZW, ZZ$. However, in addition to this contribution from SM diboson production, isolated fake leptons can also be produced in jets. Therefore also SM processes with less than 3 prompt leptons from boson decays accompanied by fake leptons can mimic the trilepton signature, thus forming a dangerous background for the SUSY trilepton search.

The direct neutralino-chargino production is the dominant SUSY production channel at the Tevatron at $\sqrt{s} = 1.96$ TeV, since here protons and antiprotons are collided, so energetic antiquarks are present. Therefore, the SUSY trilepton signature has been intensively searched for at the Tevatron with negative results so far with an accumulated luminosity of $\mathcal{L}_{acc} \sim 2 \text{ fb}^{-1}$, thus excluding the low mass SUSY region [13, 14]. The search for direct neutralino-chargino production at the LHC, which has been studied in our CMS Note [15]

for operation at $\sqrt{s} = 14$ TeV and an accumulated luminosity $\mathcal{L}_{acc} > 10 \text{ fb}^{-1}$, allows to probe SUSY mass regions well beyond the current limits from Tevatron.

The analysis presented in this thesis has been designed for the first year of LHC running with $\sqrt{s} = 10$ TeV starting in 2010 driven by the idea of searching for SUSY without suffering from the impact of the large experimental uncertainties associated with the measurement of jet energies and MET. The analysis reviews the opportunities of searching for the SUSY trimuon signature using only muons for selection, i.e. any number of jets is allowed, thus being sensitive to both mechanisms of the trimuon production $pp \rightarrow \tilde{g}\tilde{g}, \tilde{g}\tilde{q}, \tilde{q}\tilde{q}$ and $pp \rightarrow \chi_2^0\chi_1^\pm$. Muons are considered as the most robust physics objects, since the muon system of the CMS experiment, which is the outermost detector component, offers a precise measurement of the muon momentum and position as well as a small contamination by misidentified hadrons. The analysis uses data-driven methods to control the detector performance and the SM contribution after the final trimuon event selection. The detector has been extensively tested with cosmic muons during the LHC repair, see e.g. [16–20]. First collisions have been already observed after the restart of the LHC in 2009.

The thesis is organized as follows: After describing the Standard Model and SUSY in Chapter 2, the technical interlude on the LHC and the CMS detector follows in Chapter 3. The reconstruction of physics objects and the CMS software framework are discussed in Chapter 4. Chapter 5 is devoted to the trimuon SUSY search, followed by the conclusion in Chapter 7.

Chapter 2

SUSY

At the current state of knowledge, elementary particle physics approaches to the ideal of explaining nature by a mathematical model based on few fundamental constituents, forces and constants. The Standard Model of elementary particle physics agrees astonishingly well with the results of any present experiments. However, several problems are not solved in the SM, for instance the unification of gauge couplings at large energy scale or the availability of a suitable dark matter candidate. Within the theory of supersymmetry new fundamental constituents are introduced. The formalism is described in the Minimal Supersymmetric extension of the Standard Model (MSSM) and has the capability to solve several problems of the SM. Due to the fact that SUSY has not been discovered so far, the symmetry is supposed to be broken i.e. SUSY particles are heavier than their SM partners.

2.1 Standard Model

At its current state the SM describes nature with two kinds of elementary particles, distinguished by their spin. Fermions are spin(1/2) particles and considered as the fundamental constituents of ordinary matter. The interaction of particles is described by the exchange of bosons, i.e. particles with spin(1). Table 2.1 lists the particle content of the SM.

W and Z bosons mediate the weak force, the mediator of the electromagnetic force is the photon and the strong force is described by the exchange of gluons. Fermions are grouped into two different categories: leptons and quarks. Whereas the up-type leptons, the neutrinos ν , couple only to the weak force, the down-type leptons, (electrons e , muons μ and taus τ) couple to the weak and the electromagnetic force. Both leptons and quarks appear in three generations. Apart from the differences in mass, the particles within the three different generations are not distinguishable e.g. e , μ and τ carry the same electromagnetic and weak quantum numbers and thus obey the electromagnetic and weak interaction in the same way.

Quarks are the only fermions which participate in the strong interaction. The down-

Fermions Spin = 1/2						
	1. Gen.	2. Gen.	3. Gen.	Q	Y	I_3
<i>Quarks</i>	$\begin{pmatrix} u \\ d \end{pmatrix}_L$	$\begin{pmatrix} c \\ s \end{pmatrix}_L$	$\begin{pmatrix} t \\ b \end{pmatrix}_L$	2/3 -1/3	1/3	1/2 -1/2
	u_R	c_R	t_R	2/3	4/3	0
	d_R	s_R	b_R	-1/3	-2/3	0
<i>Leptons</i>	$\begin{pmatrix} \nu_e \\ e \end{pmatrix}_L$	$\begin{pmatrix} \nu_\mu \\ \mu \end{pmatrix}_L$	$\begin{pmatrix} \nu_\tau \\ \tau \end{pmatrix}_L$	0 -1	-1	1/2 -1/2
	e_R	μ_R	τ_R	-1	-2	0
Bosons Spin = 1						
Interaction	Boson		Q	Y	I_3	
Electromagnetic	γ		0	0	0	
Weak	Z^0		0	0	0	
	W^\pm		± 1	0	± 1	
Strong	$g_1 \cdots g_8$		0	0	0	

Table 2.1: Particle spectrum of the Standard Model.

type quarks denoted as d' , s' , b' represent the weak interaction eigenstates. They have been introduced in order to preserve the universality of the weak interaction, i.e. the weak interaction has the same behavior for leptons and quarks. The weak interaction eigenstates are linear combinations of the mass eigenstates d , s , b :

$$\begin{pmatrix} d' \\ s' \\ b' \end{pmatrix} = \begin{pmatrix} V_{ud} & V_{us} & V_{ub} \\ V_{cd} & V_{cs} & V_{cb} \\ V_{td} & V_{ts} & V_{tb} \end{pmatrix} \begin{pmatrix} d \\ s \\ b \end{pmatrix} , \quad (2.1)$$

where the 3×3 matrix is the Cabibbo-Kobayashi-Maskawa (CKM) matrix [21]. The elements V_{ik} of the CKM matrix specify the coupling of quark flavor i to j .

2.1.1 Lagrangians

The fundamental law of motion in classical mechanics can be described in the Euler-Lagrange equations:

$$\frac{d}{dt} \left(\frac{\partial L}{\partial \dot{q}_i} \right) = \frac{\partial L}{\partial q_i} \quad (i = 1, 2, 3) \quad , \quad (2.2)$$

where the Lagrangian L is a function of the space coordinates ($q_1 = x$, $q_2 = y$, $q_3 = z$) and their time derivatives ($\dot{q}_1 = dx/dt$, $\dot{q}_2 = dy/dt$, $\dot{q}_3 = dz/dt$). In classical mechanics the Lagrangian L is derived from an alternative formulation of Newton's second law of motion

$$L = T - U \quad , \quad (2.3)$$

with the kinetic energy $T = \frac{1}{2}mv^2$ of a particle in the scalar potential U , given by $F = -\nabla U$. However, in the SM the interaction of fundamental forces (electromagnetic, weak and strong force) are described in a relativistic field theory. In contrast to the classical calculation of the position of a particle as a function of time, field theory aims to calculate fields as functions of space and time. Hence in a relativistic field theory the Lagrangian \mathcal{L} (Lagrange density) is a function of the fields ϕ_i and their derivatives. In the classical consideration of the Euler-Lagrange equation, the derivatives \dot{q}_i are only time derivatives, whereas a relativistic field theory has to consider space and time derivatives

$$\partial_\mu \phi_i = \frac{\partial \phi_i}{\partial x^\mu} \quad , \quad (2.4)$$

with the space-time coordinates x^μ . Accordingly the Euler-Lagrange equations generalize to

$$\frac{d}{dt} \left(\frac{\partial \mathcal{L}}{\partial (\partial_\mu \phi_i)} \right) = \frac{\partial \mathcal{L}}{\partial \phi_i} \quad (i = 1, 2, 3, \dots) \quad . \quad (2.5)$$

The Lagrangians are constructed such that the Euler-Lagrange formulation leads to the desired field equations.

2.1.2 Gauge Invariance

The Dirac equation of a free particle of spin 1/2 and mass m can be written as:

$$i\gamma^\mu \partial_\mu \psi - m\psi = 0 \quad , \quad (2.6)$$

where ψ is a spinor field. The Lagrangian leading to the previous equation can be written as:

$$\mathcal{L} = i\bar{\psi}\gamma^\mu \partial_\mu \psi - m\bar{\psi}\psi \quad . \quad (2.7)$$

Gauge Invariance for Abelian Groups

In the SM as a basic principle the Lagrangian has to be invariant $\mathcal{L}(\psi') = \mathcal{L}(\psi)$ under a local phase transformation

$$\psi' = U\psi = e^{-i\lambda}\psi \quad , \quad (2.8)$$

where λ is a free phase depending on the space-time coordinate x^μ . Demanding the Lagrangian in Eq. 2.7 to be invariant under such a gauge transformation, the derivative ∂_μ is replaced by the covariant derivative

$$\mathcal{D}_\mu = \partial_\mu + iqA_\mu \quad , \quad (2.9)$$

with the new introduced gauge field A_μ . The gauge field A_μ corresponds to a spin-1 particle and is interpreted as the photon field, the gauge boson of quantum electrodynamics. The introduction of the covariant derivative Eq. 2.9 and the associated extension of the Lagrangian with a new field A_μ requires an additional term corresponding to its energy. Finally, this leads to the Lagrangian of quantum electrodynamics (QED), which describes the interaction of electrons and positrons with photons:

$$\mathcal{L} = i\bar{\psi}\gamma^\mu\partial_\mu\psi - m\bar{\psi}\psi - (q\bar{\psi}\gamma^\mu\psi)A_\mu - \frac{1}{16\pi}F^{\mu\nu}F_{\mu\nu} \quad , \quad (2.10)$$

where the term with $F^{\mu\nu} = \partial^\mu A^\nu - \partial^\nu A^\mu$ represents the Lagrangian for a massless free vector field A_μ . The transformations Eq. 2.8 are combined in the Abelian symmetry group $U(1)$.

Gauge Invariance for Non Abelian Groups

The idea of gauge invariance was further applied to non abelian symmetry groups. Yang and Mills evaluated the impact of gauge invariance for the group $SU(2)$ [22]. In comparison to the previous example where the transformations are represented by scalars (1×1 matrices), the transformations of $SU(2)$ are represented by 2×2 unitary matrices

$$U = e^{-i\tau\alpha} \quad , \quad (2.11)$$

where α is a vector with three free parameters $\alpha_1, \alpha_2, \alpha_3$ and the components of the vector τ are the Pauli matrices defined as:

$$\tau_1 = \begin{pmatrix} 0 & 1 \\ 1 & 0 \end{pmatrix} \quad , \quad \tau_2 = \begin{pmatrix} 0 & -i \\ i & 0 \end{pmatrix} \quad , \quad \tau_3 = \begin{pmatrix} 1 & 0 \\ 0 & -1 \end{pmatrix} \quad . \quad (2.12)$$

Similarly to the introduction of the photon field in the QED, the requirement of the gauge invariance leads to the presence of three vector gauge fields. Finally the Yang-Mills theory describes a Lagrangian of a system of two equal mass Dirac fields interacting with three vector gauge fields. The covariant derivative reads as:

$$\mathcal{D}_\mu = \partial_\mu + i\frac{g}{2}\mathbf{W}_\mu \quad . \quad (2.13)$$

The concepts of Yang and Mills are used in the context of the $SU(3)$ symmetry in the strong interaction and in the weak isospin-hypercharge symmetry $SU(2)_L \otimes U(1)$.

2.1.3 Lagrangian of the Standard Model

In the following the different components of the Standard Model are discussed and the Lagrangian of the SM is introduced.

Strong Component

The existence of the strong interaction has been concluded from the stability of atomic nuclei, which are stable in spite of the repulsive electromagnetic force. The classification of mesons and baryons according to the Eightfold Way predicted a baryon Ω^- [23, 24]. In the quark model this particle is composed of 3 identical quarks (sss), thus violating the Pauli Principle. Therefore the color charge was assigned to quarks, a new quantum number which comes in three colors (red, green, blue). The quark system is described in the $SU(3)_C$ symmetry group. The gauge transformations are represented by unitary 3×3 matrices

$$U = e^{-i\lambda\alpha} \quad , \quad (2.14)$$

where $\lambda_1, \lambda_2, \dots, \lambda_8$ are the Gell-Mann matrices and α_i are free parameters. The corresponding covariant derivative reads as:

$$\mathcal{D}_\mu = \partial_\mu + i\frac{g}{2}\mathbf{G}_\mu \quad , \quad (2.15)$$

where G_μ represent eight vector fields. Thus applying the concept of Yang and Mills to a system of three quark colors with identical masses lead to the occurrence of eight gauge fields in the Lagrangian, the mediators of the strong force, called gluons.

Electroweak Component

The first theoretical consideration of the weak interaction was formulated by Fermi [25]. Although the weak interactions were explained with a very good accuracy, the theory leads to cross section divergences of processes like e.g.

$$e + \nu \rightarrow e + \nu \quad . \quad (2.16)$$

The introduction of a new massive interaction particle resolved the discrepancy. The W^\pm boson was predicted as the interaction particle for the charge currents of the weak interaction. Furthermore, the neutral currents are described by another neutral massive gauge boson, the Z^0 boson. The mass of the W and Z boson corresponds to the short range of the weak force. Both particles have been discovered at the SPS Collider at CERN [26, 27].

Another peculiarity of the weak interaction had to be described by the theoretical concepts: the violation of parity (mirror symmetry) which was first observed in the beta decay of cobalt 60 in the experiment of Wu [28]. The result demonstrated that electrons created in the weak processes are left-handed and the anti-neutrinos are right-handed. The handedness describes the correlation of spin and velocity, left-handed (right-handed) particles have antiparallel (parallel) oriented spin and velocity. The different treatment of left-handed and right-handed particles corresponds to the left-handed (L) and right-handed (R) components

of a Dirac field ψ :

$$\psi_L = \frac{1 - \gamma_5}{2} \psi \quad , \quad (2.17)$$

$$\psi_R = \frac{1 + \gamma_5}{2} \psi \quad . \quad (2.18)$$

Glashow, Weinberg and Salam unified the weak and electromagnetic interaction in the GSW-Model which described the interaction in the $SU(2)_L \otimes U(1)_Y$ symmetry group [29–31]. To get access to the spin formalism, the weak isospin with its third component I_3 was introduced as a new quantum number. Left-handed leptons and quarks were arranged in isospin doublets and right-handed fermions were arranged in singlets, since they do not couple to the W boson.

The generator of the $U(1)$ symmetry group is the hypercharge Y , which depends on the electric charge Q of a particle and its third component of the isospin I_3 as:

$$Q = I_3 + \frac{1}{2}Y \quad . \quad (2.19)$$

The left-handed and right-handed components of the Dirac field are combined with the electromagnetic interaction in the Lagrangian of the $SU(2)_L \otimes U(1)_Y$ symmetry group. The $SU(2)_L$ group for the transformation of the left-handed leptons introduces three vector fields W_μ and the $U(1)$ group leads to an additional single vector field B_μ .

The SM Lagrangian

Finally the Lagrangian of the SM is summarized as a combination of the symmetry group $SU(3)_C$ of the strong interaction and the $SU(2)_L \otimes U(1)_Y$ symmetry group of the unification of the weak and electromagnetic interaction. The corresponding symmetry group is

$$SU(3)_C \otimes SU(2)_L \otimes U(1)_Y \quad . \quad (2.20)$$

The Lagrangian of the SM can be factorized as:

$$\mathcal{L}_{\text{SM}} = \mathcal{L}_{\text{ferm}} + \mathcal{L}_{\text{gauge}} + \mathcal{L}_{\text{Higgs}} + \mathcal{L}_{\text{Yukawa}} \quad , \quad (2.21)$$

where the first term is the gauge invariant free fermion Lagrangian

$$\mathcal{L}_{\text{ferm}}^{\text{free}} = \sum_f \bar{\Psi}_f i \gamma^\mu D_\mu \Psi_f \quad , \quad (2.22)$$

$$\text{with} \quad D_\mu = \partial_\mu + \frac{ig'}{2} B_\mu Y + \frac{ig}{2} \mathbf{W}_\mu \boldsymbol{\tau} + \frac{ig_s}{2} \mathbf{G}_\mu \boldsymbol{\lambda} \quad .$$

The covariant derivative D_μ ensures the gauge invariance. B_μ , \mathbf{W}_μ and \mathbf{G}_μ are the gauge boson fields of the symmetry groups with the coupling constants g' , g and g_s , respectively.

The corresponding generators are $Y/2$, $\tau/2$ and $\lambda/2$.

The free term of the gauge fields reads as:

$$\mathcal{L}_{\text{gauge}} = -\frac{1}{4}(B_{\mu\nu}B^{\mu\nu} + \mathbf{W}_{\mu\nu}\mathbf{W}^{\mu\nu} + \mathbf{G}_{\mu\nu}\mathbf{G}^{\mu\nu}) \quad . \quad (2.23)$$

The last two terms in Eq. 2.21 are related to the mass of fermions and bosons. The requirement of gauge invariance can only be satisfied by the introduction of massless gauge fields in the Lagrangian. But once they are massive, as predicted for the bosons of the weak interaction, the invariance will be lost.

2.1.4 Higgs Mechanism

This dilemma is resolved by the introduction of the Higgs field Φ . The concept of the Higgs mechanism relies on the strategy of spontaneous symmetry breaking [32]. Bosons and fermions get their masses by coupling to the Higgs field. Therefore two additional terms are added to the Lagrangian: the term $\mathcal{L}_{\text{Higgs}}$ describes the Higgs field and the couplings to bosons, whereas the coupling of fermions to the Higgs field is given by the term $\mathcal{L}_{\text{Yukawa}}$.

In the Lagrangian of the SM the term corresponding to the Higgs field reads as:

$$\mathcal{L}_{\text{Higgs}} = (D^\mu\Phi)^\dagger(D_\mu\Phi) - V(\Phi) \quad , \quad (2.24)$$

where D^μ are the covariant derivatives, which ensure that the Lagrangian is invariant under a transformation of the $SU(2)_L \otimes U(1)_Y$ symmetry group. The Euler-Lagrange formula with the first term of the Lagrangian leads to the Klein-Gordon equation of motion describing a free particle of spin 0.

Accordingly the Higgs field Φ is a (complex) scalar field. It can be described as a $SU(2)_L$ -doublet carrying weak hypercharge $Y = 1$, with a charged and a neutral component

$$\Phi = \begin{pmatrix} \Phi^+ \\ \Phi^0 \end{pmatrix} = \frac{1}{\sqrt{2}} \begin{pmatrix} \phi_1(x) + i\phi_2(x) \\ \phi_3(x) + i\phi_4(x) \end{pmatrix} \quad . \quad (2.25)$$

The potential $V(\Phi)$ of the Higgs field in Eq. 2.24 reads as:

$$V(\Phi) = \mu^2\Phi^\dagger\Phi + \lambda(\Phi^\dagger\Phi)^2 \quad , \quad (2.26)$$

with a positive and real parameter λ . The particular feature of the Higgs potential $V(\Phi)$ reveals with a consideration of the minima of the potential, which depends on the sign of μ^2 . Fig. 2.1 shows the one-dimensional shape of the Higgs potential for $\mu^2 > 0$ and $\mu^2 < 0$. Considering $\mu^2 \geq 0$ the energetic ground state of the Higgs field at the minimum of the potential is $\Phi = 0$. Thus the vacuum expectation value considered as the expectation value at the minimum of the Higgs potential disappears:

$$v = |\langle 0|\Phi|0\rangle| = 0 \quad . \quad (2.27)$$

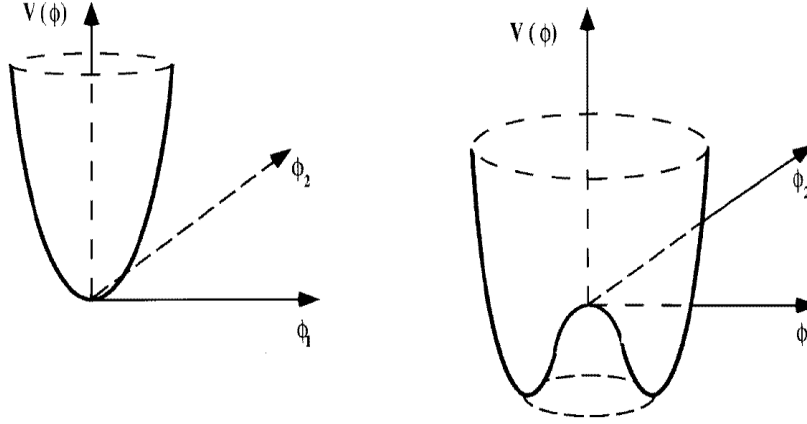


Figure 2.1: Shape of the Higgs potential for $\mu^2 > 0$ (L) and $\mu^2 < 0$ (R). ϕ_1 and ϕ_2 are the real and imaginary parts of the Higgs field [9].

However if μ^2 becomes negative and the configuration of the Higgs field fulfills

$$|\Phi|^2 = \Phi^\dagger \Phi = \frac{1}{2}(\phi_1^2 + \phi_2^2 + \phi_3^2 + \phi_4^2) = \frac{-\mu^2}{2\lambda} \quad , \quad (2.28)$$

the minimum of the potential and thus the vacuum expectation value of Φ corresponds to

$$v = |\langle 0|\Phi|0\rangle| = \sqrt{\frac{-\mu^2}{2\lambda}} \quad . \quad (2.29)$$

Eq. 2.28 shows the degeneracy of the ground state i.e. different field configurations $(\phi_1, \phi_2, \phi_3, \phi_4)$ can realize the ground state of the Higgs field. Though a transformation of the $SU(2)_L \otimes U(1)_Y$ group converts a ground state to another ground state, thus breaking the symmetry. But since the vacuum expectation value stays unchanged also the Lagrangian remains invariant under such a transformation. This mechanism is known as spontaneous symmetry breaking.

In order to obtain the physical interpretation of the Higgs particle, the ground state of the Higgs field is assumed as:

$$\Phi_0 = \begin{pmatrix} 0 \\ v \end{pmatrix} \quad \text{with} \quad v = \sqrt{\frac{-\mu^2}{2\lambda}} \quad . \quad (2.30)$$

Here a neutral ground state ($|\Phi^+| = 0$) is considered, since the vacuum is known to be neutral. Considering an arbitrary $SU(2)$ phase factor, the quantum fluctuations of the Higgs field around the ground state can be written as:

$$\Phi(x) = e^{i\zeta^a(x)\tau^a} \begin{pmatrix} 0 \\ v + h(x) \end{pmatrix} \quad , \quad (2.31)$$

where the fluctuations are splitted according to their direction. The contribution of the fluctuations along the minimum of the potential are emphasized in the fields $\zeta^a(x)$, which are interpreted as three massless Goldstone bosons. The fields $\zeta^a(x)$ have no physical significance, since they can be eliminated by a suitable local gauge transformation

$$\Phi(x) \rightarrow \Phi'(x) = e^{-i\zeta^a(x)\tau^a} \Phi(x) = \begin{pmatrix} 0 \\ v + h(x) \end{pmatrix} . \quad (2.32)$$

They remain as longitudinal polarizations of the massive gauge bosons. The field $h(x)$ can be interpreted as the Higgs particle.

The mass of the gauge bosons are generated by interaction with the Higgs fields. Considering the gauge form of the Higgs field (Eq. 2.32), the first term of the Lagrangian (Eq. 2.24) reads as:

$$(D_\mu \Phi)^\dagger (D^\mu \Phi) = (0, v) \left[\frac{g}{2} \tau \mathbf{W}_\mu + \frac{g'}{2} B_\mu Y \right]^2 \begin{pmatrix} 0 \\ v \end{pmatrix} + h(x)\text{-terms} . \quad (2.33)$$

Using the Pauli matrices (Eq. 2.12) and the weak hypercharge $Y = 1$, this term of the Lagrangian can be separated in a term depending on the fields W_μ^1 and W_μ^2 :

$$\left(\frac{gv}{2} \right)^2 \left((W_\mu^1)^2 + (W_\mu^2)^2 \right) \quad (2.34)$$

and in terms of the fields B_μ and W_μ^3 :

$$(B_\mu^\dagger, W_\mu^{3\dagger}) M \begin{pmatrix} B_\mu \\ W_\mu^{3,\mu} \end{pmatrix} , \quad \text{with} \quad M = \frac{v^2}{4} \begin{pmatrix} g'^2 & +gg' \\ +gg' & g^2 \end{pmatrix} . \quad (2.35)$$

Though the fields $W_\mu^{1,2}$ cannot be interpreted as the gauge bosons fields. The substitution

$$W_\mu^+ = \frac{1}{\sqrt{2}} (W_\mu^1 + iW_\mu^2) \quad (2.36)$$

$$W_\mu^- = \frac{1}{\sqrt{2}} (W_\mu^1 - iW_\mu^2) \quad (2.37)$$

leads to the physical gauge fields of the charged W bosons. Accordingly Eq. 2.34 can be written as:

$$M_W^2 W_\mu^+ W_\mu^- \quad \text{with} \quad M_W^2 = \frac{g^2 v^2}{4} , \quad (2.38)$$

where M_W is interpreted as the mass of the W boson.

The physical gauge fields of the Z boson and the photon occur as mixed states of the fields B_μ and W_μ^3 . The matrix M in Eq. 2.35 can be diagonalized with the unitary matrix

$$U = \frac{1}{\sqrt{g'^2 + g^2}} \begin{pmatrix} g & g' \\ g' & g \end{pmatrix} = \begin{pmatrix} \cos \theta_W & \sin \theta_W \\ -\sin \theta_W & \cos \theta_W \end{pmatrix} , \quad (2.39)$$

i.e. the diagonal form is UMU^{-1} . Here θ_W is known as the Weinberg angle. Substituting the matrix M with $U^{-1}UMU^{-1}U$ in Eq. 2.35 introduces the fields A_μ, Z_μ as a mixture of the fields B_μ and W_μ^3 :

$$\begin{pmatrix} A^\mu \\ Z^\mu \end{pmatrix} = U \begin{pmatrix} B^\mu \\ W^{3,\mu} \end{pmatrix} . \quad (2.40)$$

Hence, Term 2.35 can be written in terms of the new fields as:

$$\frac{1}{2}(A_\mu, Z_\mu) \begin{pmatrix} 0 & 0 \\ 0 & M_Z^2 \end{pmatrix} \begin{pmatrix} A^\mu \\ Z^\mu \end{pmatrix} \quad \text{with} \quad M_Z^2 = \frac{g'^2 + g^2}{4} v^2 , \quad (2.41)$$

where M_Z corresponds to the mass of Z boson.

The coupling constants g, g' , the Weinberg angle θ_W and the electric charge e are related as:

$$g' \cos \theta_W = g \sin \theta_W = e \quad \text{and} \quad \sin^2 \theta_W = \frac{g'^2}{g^2 + g'^2} . \quad (2.42)$$

The relation of the Weinberg angle and the masses of the W and Z gauge bosons are

$$\sin^2 \theta_W = 1 - \frac{M_W^2}{M_Z^2} . \quad (2.43)$$

Also leptons (e, μ, τ) and quarks get mass by interacting with the Higgs field. This is described in the Yukawa terms of the SM Lagrangian $\mathcal{L}_{\text{Yukawa}}$, which reads for the first lepton generation as:

$$\mathcal{L}_{\text{Yukawa}}^e = h^e [\bar{L}\Phi e_R + \bar{e}_R\Phi^\dagger L] , \quad (2.44)$$

where h^e is the Yukawa coupling constant and L is the left-handed isospin doublet. The electron mass term can be obtained by substituting the Higgs field with the vacuum expectation value as:

$$\begin{aligned} \mathcal{L}_{\text{Yukawa}} &= h_e \left[(\bar{\nu}_e, \bar{e})_L \begin{pmatrix} 0 \\ v \end{pmatrix} e_R + \bar{e}_R(0, v) \begin{pmatrix} \nu_e \\ e \end{pmatrix}_L \right] \\ &= h_e v [\bar{e}_L e_R + \bar{e}_R e_L] . \end{aligned} \quad (2.45)$$

This term has the form of a Dirac mass term describing a spin 1/2 particle with mass $m = h_e v$. Therefore the Yukawa coupling h_e is proportional to the mass of the particle. Since h_e describes the coupling of the fermion to the Higgs field, also the Higgs-fermion coupling is proportional to the mass of the fermion. The masses of the down-type quarks are generated in the same way with a new coupling h_d . In this consideration the Lagrangian leads to massless neutrinos. In contrast to the left-handed lepton doublets L , the up-type quarks in the left-handed quark doublets Q are not massless. The masses of the up-type quarks are generated using the charge conjugated Higgs field

$$\Phi^C = -i\tau_2\Phi^* \equiv \begin{pmatrix} -v - h \\ 0 \end{pmatrix} . \quad (2.46)$$

The total Yukawa term of the SM Lagrangian reads as:

$$\mathcal{L}_{\text{Yukawa}} = h_e^i \bar{L}^i \Phi e_R^i + h_d^{ij} \bar{Q}^i \Phi d_R^{ij} + h_u^{ij} \bar{Q}^i \Phi^C u_R^{ij} + h.c. \quad , \quad (2.47)$$

where the indices i, j are related to the three generations. For the quark sector the mass matrix is not diagonal, i.e. the mass eigenstates are not equal to the interaction eigenstates. The mass matrix is diagonalized using the CKM matrix.

2.2 Motivation for Supersymmetry

The physic model of matter as it is described in the Standard Model of particle physics agrees astonishingly with results of experiments, at the moment there is no experimental result which disagrees with predictions of the theory by more than 3.2σ [33]. The SM contains a number of free parameters, which are summarized below:

- α, G_F, M_Z : the fine-structure constant, the Fermi constant and the mass of the Z-boson representing the fundamental constants of the electroweak theory
- α_s : the coupling constant of the strong force defining g_s
- m_e, m_μ, m_τ : the masses the down-type leptons
- $m_d, m_s, m_b, m_u, m_c, m_t$: the masses of the quarks
- 4 parameters of the CKM matrix
- M_H : the mass of the Higgs boson.

These are 18 parameters without the consideration of the neutrino masses. The discovery of neutrino oscillation indicates that neutrinos are massive [34]. Extending the Standard Model with massive neutrinos, at least 3 mass parameters have to be included.

2.2.1 Frontiers of the Standard Model

In spite of the experimental success of the Standard Model, fundamental questions remain unanswered [9]. Some are listed below:

- **Free parameters:** As introduced in the last paragraph, there are at least 18 free parameters, which have to be determined experimentally. The large number of manually introduced parameters prevents the SM from being considered as the ultimate fundamental theory.
- **Gravity:** The theoretical consideration of gravity is missing in the SM. The formulation of a quantum theory of gravity has not been realized so far. At the low energy scale gravity is negligible, but at a very high energy gravity has to be included in the theoretical consideration.

- **Dark matter:** Astrophysical measurements lead to the conclusion that the universe consists of only 5% ordinary baryonic matter described by the Standard Model, whereas the contribution of cold dark matter corresponds to 23% [5]. Within the Standard Model the origin of cold dark matter in the universe can not be explained.
- **Charge quantization:** The SM can not explain why the proton and the electron have exactly the opposite charge.
- **Fine tuning:** The physical mass of the Higgs boson depends on its bare mass and additionally on radiative corrections. Radiative corrections to the Higgs mass are proportional to the mass squared of heavy particles. However this contribution can be canceled in the SM, but needs a very accurate fine tuning.
- **Unification of couplings:** The coupling constants g , g' and g_s depend on the energy scale, which is described by the renormalization group equations. Since the strong and weak couplings decrease with increasing energy, while the electromagnetic coupling increases, a unification of the coupling constants becomes possible and would be a manifestation of the unique origin of three forces. In the frame of Grand Unified Theories (GUTs), which is discussed the next section, the couplings are expected to unify at the unification scale M_{GUT} . Within the SM i.e. without the influence of physics beyond the SM, a unification of the couplings is not possible.
- **Hierarchy problem:** The hierarchy problem arises from the difference of the electroweak scale and a possible unification scale. Why is the electroweak scale so small compared to the GUT scale ($M_{GUT} \gg M_W$)?

2.2.2 Aspects of Grand Unified Theories

This section discusses very briefly the aspects of Grand Unified Theories (GUTs), since some of the problems listed above are resolved in GUTs. In the GUTs the weak, strong and electromagnetic interaction are considered as branches of a unique interaction. For this purpose a larger group G is introduced, assuming that the $SU(3)_C \otimes SU(2)_L \otimes U(1)_Y$ symmetry group is a subset of G . In addition the symmetry group G has to meet the requirement of symmetry breaking below the unification scale $M_{GUT} \approx 10^{16} - 10^{19} GeV$. Among several symmetry groups the $SU(5)$ and $SO(10)$ are the most suitable structures. The coupling α_{GUT} represents the coupling of the unique interaction at the GUT scale. Starting from a unique coupling α_{GUT} , in a $SU(5)$ representation the 15 fermions of the first generation can be written as a $\{\bar{5}\}$ -plet and a $\{10\}$ -plet:

$$\bar{\mathbf{5}} = \begin{pmatrix} d_g^C \\ d_r^C \\ d_b^C \\ e^- \\ -\nu_e \end{pmatrix}_L \quad \mathbf{10} = \begin{pmatrix} 0 & -u_b^C & u_r^C & u_g & d_g \\ u_b^C & 0 & -u_g^C & u_r & d_r \\ -u_r^C & u_g^C & 0 & u_b & d_b \\ -u_g & -u_r & -u_b & 0 & e^+ \\ -d_g & -d_r & -d_b & -e^+ & 0 \end{pmatrix}_L . \quad (2.48)$$

Here the right-handed fermions are considered as charge conjugated left-handed fermions $f_R = f_L^C$ with the charge conjugated index C . Hence, the multiplets are build of a proper helicity.

Some consequences of the theoretical consideration of unification are listed below:

- **Proton decay:** The requirement of gauge invariance leads to $N^2 - 1 = 24$ gauge fields, including the already known 12 gauge fields of the Standard Model. The 12 new gauge fields are denoted as

$$X_\mu^i, Y_\mu^i, X_{i,\mu}^C \text{ and } Y_{i,\mu}^C \text{ with } i = 1, 2, 3$$

and carry electric charge ($Q_X = 4/3 e$ and $Q_Y = 1/3 e$), weak hypercharge and color. Since the baryon and lepton number conservation can be violated, consequently the proton decay is allowed in processes mediated by the new gauge fields. The dominant proton decay mode is $p \rightarrow e^+ + \pi^0$. The lifetime τ of the proton can be estimated from

$$\tau_p \approx \frac{1}{\alpha_{SU(5)}^2} \frac{M_X^4}{m_p^5} . \quad (2.49)$$

However the proton decay has not been discovered yet and the minimal measured lifetime of the proton has been determined to $\sim 10^{33}$ years [3]. The lower limit for the mass of the new bosons M_X is

$$M_{GUT} > 2.4 \times 10^{15} \text{ GeV} .$$

The proton lifetime measurement can exclude minimal SU(5) GUT models, since in those models the unification of the couplings is expected at a scale well below 10^{15} GeV [35].

- **Charge quantization:** In GUTs quarks and leptons are described in a single multiplet. The operators corresponding to the quantum numbers are represented by traceless matrices. Consequently the charge of lepton and quarks are related, since for the 5plet the charge operator Q has to fulfill

$$Tr(Q) = Tr(q_{\bar{d}}, q_{\bar{d}}, q_{\bar{d}}, q_e, q_\nu) = 0 \quad (2.50)$$

$$\Rightarrow 3q_{\bar{d}} + e = 0 . \quad (2.51)$$

Hence, assigning the quarks and leptons to multiplets can predict the charge of d -quark to be $1/3$ of the charge of an electron. In the same way the charge of the u -quark is predicted to be $2/3$ of the positron charge and thus the proton charge (uud) can be explained to be exactly the opposite of the electron charge.

- **Yukawa coupling unification (free parameters):** In addition to the beneficial consequences mentioned above, the multiplet structure of quarks and leptons leads

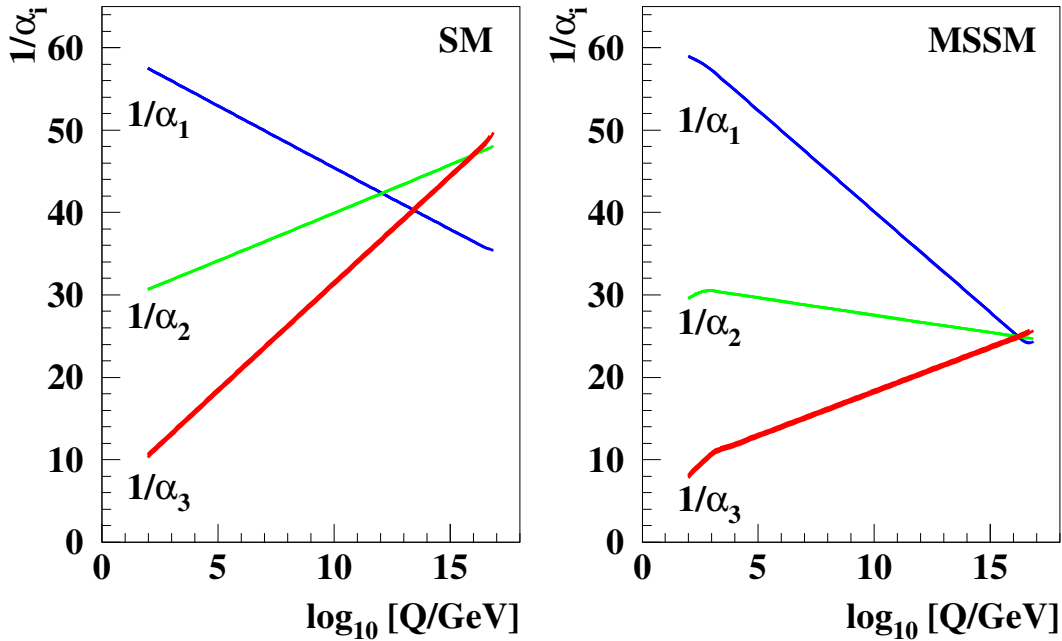


Figure 2.2: Unification of the coupling constants in the SM (L) and MSSM (R) [12].

to a unification of the Yukawa couplings. The Yukawa couplings of the bottom quark and the τ -lepton unify as:

$$h_b = h_\tau = h \quad , \quad (2.52)$$

whereas the couplings of the top quark remains a free parameter. The Yukawa couplings of the bottom quark, top quark and τ -lepton unify at M_{GUT} in $SO(10)$ structures as:

$$h_b = h_t = h_\tau = h \quad . \quad (2.53)$$

A simple Yukawa unification is not possible for the first two generations of quarks and leptons [3]. However the number of free parameters is reduced in GUTs.

2.2.3 Aspects of Supersymmetry

The Minimal Supersymmetric extension of the Standard Model is based on a symmetry of fermions and bosons, where each $\text{spin}(j)$ particle has a supersymmetric partner with $\text{spin}(j \pm 1/2)$. The details of SUSY are discussed in the next chapter. SUSY can resolve some of the problems of the Standard Model mentioned in Section 2.2.1:

- **Unification of couplings:** The contribution of SUSY particles changes the energy dependency of the coupling constants. Fig. 2.2 shows the inverse of the couplings as

a function of the logarithm of the energy for the SM and MSSM [12]. The unification of the coupling constants can only be obtained by including new physics between the electroweak and the Planck scale. If the masses of the supersymmetric particles are in the range of $M_{\text{SUSY}} \sim 1$ TeV, the unification of the couplings is realized within SUSY models.

- **Hierarchy problem:** SUSY models can explain the large differences of the scale of M_W and M_{GUT} . In SUSY models the mechanism of electroweak symmetry breaking is not assumed ad-hoc, but is triggered by radiative corrections from the top-quark Yukawa coupling to the Higgs sector which drives one of the Higgs masses squared negative. The logarithmical energy dependency of the radiative corrections leads to the large differences of the two scales.
- **Gravity:** Within the idea of unification of all forces also gravity has to be included. The graviton is the mediator of the gravitational force. In contrast to the other bosons, the graviton has spin 2 and belongs to different representations of the Poincare-Algebra, which forbids the unification in a single algebra. The only exception is the supersymmetric algebra [36].
- **Fine Tuning:** SUSY particles preserve the mass of the Higgs boson by cancellation of the contributions from boson loops with fermion loops. Hence, the preservation can be achieved without unnatural fine-tuning, but only up to a SUSY breaking scale of $M_{\text{SUSY}} \leq 1$ TeV.
- **Dark Matter:** In R -parity conserving SUSY models, the lightest SUSY particle (LSP) is assumed to be stable and its coupling to normal matter is forbidden. Additionally the LSP is a massive particle. Therefore the lightest neutralino is a perfect dark matter candidate.
- **Unification Scale of GUTs:** Due to the proton lifetime constraint, the minimal consideration (only SM) of GUTs have a unification point well below 10^{15} GeV and are ruled out. The consideration of minimal supersymmetric SU(5) GUT models adjust the unification scale above 10^{15} GeV. Thus SUSY is paving the way to grand unification, which may resolve further problems of the SM.

2.3 Supersymmetry

The supersymmetric extension of the Standard Model assumes a symmetry of fermions and boson. The generator of the SUSY Algebra

$$\mathbf{Q}|\text{Fermion}\rangle \propto |\text{Boson}\rangle \quad \text{and} \quad \mathbf{Q}|\text{Boson}\rangle \propto |\text{Fermion}\rangle \quad (2.54)$$

changes the spin of a particle by 1/2. The generator Q fulfils the relation

$$\{Q_\alpha, Q_\beta\} = 0 \quad \text{and} \quad \{Q_\alpha, \bar{Q}_\beta\} = 2\sigma_{\alpha\beta}^\mu P_\mu \quad , \quad (2.55)$$

where P_μ is the momentum four vector and σ^μ are the Pauli matrices. The Minimal Supersymmetric extension of the Standard Model has only one generator Q and is considered as a $N = 1$ SUSY model. The MSSM assigns a SUSY partner particle to each SM particle, with the same quantum numbers except for the spin, which differs by $1/2$. These particles are called superpartners. Up to now, experiments of particle physics have not seen any evidence of the particles predicted by supersymmetry. The absence of the superpartners is believed to be explained by the fact that the mass of the superpartners is very large. Therefore supersymmetry must be a broken symmetry i.e. SM particles and their superpartners are not equal in mass. However as soon as the energy of the accelerator is large enough, the superpartners will be created. The analysis presented in this thesis provides a recipe how the creation of superpartners may be discovered. In the following subsection the particle spectrum of the MSSM is introduced.

2.3.1 Particle Spectrum

Supersymmetry associates known bosons with new fermions and known fermions with new bosons [36]. Table 2.2 shows the particle spectrum of the MSSM.

- The superpartners of the quarks and leptons are called squarks and sleptons, respectively. e.g. selectron, smuon, stau,... . Since the fermions have two spin states i.e. spin up and down, whereas their superpartners are scalars, there are actually two superpartners for each fermion, corresponding to the spin state. The left-handed leptons and the quarks build a multiplet with their corresponding superpartners, whereas the right-handed fermions are arranged in doublets with their superpartners.
- The gauge bosons and their superpartners form a multiplet. The superpartners of the gauge bosons are labeled with the ending 'ino' ($W \rightarrow$ Wino, $Z \rightarrow$ Zino,...).
- Since in the MSSM the charge conjugated Higgs fields are not suitable to generate the masses of the up-type quarks, an additional Higgs field is introduced. The superpartner of the Higgs boson is the higgsino.

2.3.2 Lagrangian of the MSSM

The Lagrangian of the MSSM is composed of two parts:

$$\mathcal{L} = \mathcal{L}_{\text{SUSY}} + \mathcal{L}_{\text{Breaking}} \quad . \quad (2.56)$$

The first term $\mathcal{L}_{\text{SUSY}}$ describes the supersymmetric generalization of the SM. Since the symmetry of SM particles and their superpartners is broken, the Lagrangian has to contain a term corresponding to the mechanism of symmetry breaking $\mathcal{L}_{\text{Breaking}}$.

The supersymmetric term $\mathcal{L}_{\text{SUSY}}$ includes the gauge invariant kinetic terms corresponding to the $SU(3)$, $SU(2)$, $U(1)$ gauge groups depending on 3 gauge couplings as in the Standard

Superfield	Bosons	Fermions	$SU(3)_C$	$SU(2)_L$	$U(1)_Y$
Gauge					
\mathbf{G}^a	g^a	\tilde{g}^a	8	0	0
\mathbf{V}^k	$W^k (W^\pm, Z_0)$	$\tilde{w}^k (\tilde{w}^\pm, \tilde{z}_0)$	1	3	0
\mathbf{V}'	B/γ	$\tilde{b} / \tilde{\gamma}$	1	1	0
Matter					
\mathbf{L}_i	Sleptons $\left\{ \begin{array}{l} \tilde{L}_i = (\tilde{\nu}, \tilde{e})_L \\ \tilde{E}_i = \tilde{e}_R \end{array} \right.$	Leptons $\left\{ \begin{array}{l} L_i = (\nu, e)_L \\ E_i = e_R \end{array} \right.$	1	2	-1
\mathbf{E}_i			1	1	2
\mathbf{Q}_i	Squarks $\left\{ \begin{array}{l} \tilde{Q}_i = (\tilde{u}, \tilde{d})_L \\ \tilde{U}_i = \tilde{u}_R \\ \tilde{D}_i = \tilde{d}_R \end{array} \right.$	Quarks $\left\{ \begin{array}{l} Q_i = (u, d)_L \\ U_i = u_R \\ D_i = d_R \end{array} \right.$	3	2	1/3
\mathbf{U}_i			3	1	-4/3
\mathbf{D}_i			3	1	2/3
Higgs					
\mathbf{H}_1	Higgs $\left\{ \begin{array}{l} H_1 \\ H_2 \end{array} \right.$	higgsino $\left\{ \begin{array}{l} \tilde{H}_1 \\ \tilde{H}_2 \end{array} \right.$	1	2	-1
\mathbf{H}_2			1	2	1

Table 2.2: Particle spectrum of the MSSM [37]. The particles and the superpartners are arranged in super-multiplets, where $a = 1 \dots 8$ is the index of $SU(3)_c$ and $k = 1 \dots 3$ is the index of $SU(2)_L$. The three generation are labeled with the index $i = 1 \dots 3$. The last three columns are denoted for the quantum number of internal symmetries, defining the behavior under transformation.

Model and a supersymmetric extension of the Yukawa term describing the interaction of the particles with each other:

$$\mathcal{L}_{\text{SUSY}} = \mathcal{L}_{\text{Gauge}} + \mathcal{L}_{\text{Yukawa}} \quad . \quad (2.57)$$

The superpotential W_R of the Yukawa term $\mathcal{L}_{\text{Yukawa}}$ reads as:

$$W_R = \varepsilon_{ij} (h_U^{ab} Q_a^j U_b^C H_2^i + h_D^{ab} Q_a^j D_b^C H_1^i + h_L^{ab} L_a^j E_b^C H_1^i + \mu H_1^i H_2^j) \quad , \quad (2.58)$$

with the $SU(2)$ indices $i, j = 1, 2$, the generation labels $a, b = 1, 2, 3$, the Yukawa couplings $h_{U,D,L}$ and the antisymmetric tensor ε_{ij} . Charge conjugated fields are denoted by the label C . This part of the Lagrangian is similar to that of the SM, but in comparison, the superpotential contains only superfields rather than the ordinary fields of the SM. Additional the last term describes the Higgs mixing, which is absent in the SM, since here only one Higgs field appears.

***R*-Parity**

In principle the superpotential can contain also terms which violate either the lepton or the baryon number conservation. Since neither lepton nor baryon number violation has been observed so far, those terms must be suppressed in the superpotential. The introduction of

a special symmetry called R -parity resolves the problem. The R -parity is an multiplicative quantum number defined as:

$$R = (-1)^{3(B-L)+2S} \quad , \quad (2.59)$$

where B is the baryon number, L is the lepton number and S is the spin of the particle [36]. Therefore R is $+1$ for all leptons and quarks. In contrast R is -1 for their superpartners, because of the factor $(-1)^{2S}$. The conservation of R -parity has the following consequences:

- The lightest supersymmetric particle is absolutely stable, since the decay to normal matter would change the R -parity. Therefore, if the LSP is uncharged, it is an attractive candidate for dark matter. Furthermore, regarding the production of supersymmetric particles at collider experiments, once a LSP is produced, it can not decay subsequently to known SM particles.
- The decay products of sparticles must contain an odd number of LSPs. This is a characteristic of the SUSY production at the LHC, which can be used to distinguish events with from events without SUSY particles.
- The superpartners of the SM particles are produced in pairs e.g. also in the proton-proton collision at the Large Hadron Collider SUSY particles can be only produced in pairs. Consequently there are always at least two LSPs produced.

Breaking Mechanism

Since modern experiments of particle physics have not seen an evidence of the superpartners, the mass of the superpartners is expected to be very large and supersymmetry must be a broken symmetry. The breaking of the symmetry can be introduced by additional breaking terms. Since the breaking terms do not introduce new quadratic divergences, they are called soft breaking terms:

$$\begin{aligned} L_{\text{Breaking}} = & m_{H_1}^2 H_1^\dagger H_1 + m_{H_2}^2 H_2^\dagger H_2 + B\mu (H_2^T i\tau_2 H_1 + h.c.) \\ & + \sum_i \left(\tilde{m}_{Q_i}^2 \tilde{Q}_i^\dagger \tilde{Q}_i + \tilde{m}_{L_i}^2 \tilde{L}_i^\dagger \tilde{L}_i + \tilde{m}_{U_i}^2 \tilde{U}_i^\dagger \tilde{U}_i + \tilde{m}_{D_i}^2 \tilde{D}_i^\dagger \tilde{D}_i + \tilde{m}_{E_i}^2 \tilde{E}_i^\dagger \tilde{E}_i + h.c. \right) \\ & + \sum_{i,j} \left(A_u^{ij} h_u^{ij} \tilde{U}_i H_2 \tilde{Q}_j + A_d^{ij} h_d^{ij} \tilde{D}_i H_1 \tilde{Q}_j + A_e^{ij} h_e^{ij} \tilde{L}_i H_1 \tilde{L}_j + h.c. \right) \\ & + \frac{1}{2} \sum_{l=1}^3 M_l \tilde{\lambda}_l \tilde{\lambda}_l + h.c. \quad . \end{aligned} \quad (2.60)$$

Here $H_{1,2}$ are the Higgsdoublets, μ is the mass parameter of the superpotential (Eq. 2.58), B is the bilinear coupling, $A_{u,d,e}^{ij}$ is the trilinear coupling of interactions of Higgs fields and sfermions, the indices $i, j = 1, 2, 3$ run over the three generations and $\tilde{\lambda}_l$ are the gauginos, the superpartner of the gauge boson.

Obviously a vast number of new parameters are introduced to generate the breaking of the symmetry. The number of free parameters can be reduced by assuming the universality or equality of various parameters at a high energy scale. For this purpose several approaches have been developed. In the presented analysis the mSUGRA model is used [38], here supersymmetry is broken by a coupling to a yet unknown supergravity theory, assuming the unification at M_{GUT} of:

$$M_1(M_{\text{GUT}}) = M_2(M_{\text{GUT}}) = M_3(M_{\text{GUT}}) \equiv m_{1/2} \quad (2.61)$$

$$\tilde{m}_{E,L,U^i,D^i,Q^i}(M_{\text{GUT}}) = m_{H_{1,2}}(M_{\text{GUT}}) \equiv m_0 \quad (2.62)$$

$$A_t(M_{\text{GUT}}) = A_b(M_{\text{GUT}}) = A_\tau(M_{\text{GUT}}) \equiv A_0 \quad , \quad (2.63)$$

where $m_{1/2}$ is the unified gaugino mass, m_0 is the unified scalar mass and A_0 the unified trilinear coupling. The trilinear couplings appear only as a product with the corresponding Yukawa coupling and the Yukawa couplings of the first two generations are comparable small to the third generation. Therefore it is sufficient to use the trilinear coupling of the third generation.

In the mSUGRA model the vast number of free parameters of the MSSM is reduced to five free parameters, namely:

- $m_{1/2}$, the unified gaugino mass $m_{1/2}$ at the GUT scale
- m_0 , the unified scalar mass m_0 at the GUT scale
- B , the bilinear coupling or equivalent $\tan\beta \equiv \frac{v_1}{v_2}$, the ratio of the vacuum expectation values of the two Higgs fields
- A_0 , the unified trilinear coupling A_0 at the GUT scale
- μ , the Higgs field mixing parameter.

2.3.3 SUSY Mass Spectrum

In the MSSM, the masses of the SUSY particles can be calculated via the renormalization group equations (RGE), which are derived from the Lagrangian. With a given initial condition at the GUT scale, the solution of the RGE link the values at the GUT scale with the electroweak scales and thus determine the mass matrices of gauginos, squarks and leptons.

Neutralinos and Charginos

Neutralinos and Charginos are the mass eigenstates of the neutral and charged fields, respectively. Their mass eigenstates are mixed states of gauginos and higgsinos:

$$\chi = \begin{pmatrix} \tilde{B} \\ \tilde{W}^3 \\ \tilde{H}_1^0 \\ \tilde{H}_2^0 \end{pmatrix} \quad , \quad \Psi = \begin{pmatrix} \tilde{W}^+ \\ \tilde{H}^+ \end{pmatrix} \quad , \quad (2.64)$$

where χ and Ψ are the Majorana neutralino and Dirac chargino fields, respectively.

The corresponding neutralino mass matrix reads as:

$$M^{(0)} = \begin{pmatrix} M_1 & 0 & -M_Z \cos \beta \sin \theta_W & M_Z \sin \beta \sin \theta_W \\ 0 & M_2 & M_Z \cos \beta \cos \theta_W & -M_Z \sin \beta \cos \theta_W \\ -M_Z \cos \beta \sin \theta_W & M_Z \cos \beta \cos \theta_W & 0 & -\mu \\ M_Z \sin \beta \sin \theta_W & -M_Z \sin \beta \cos \theta_W & -\mu & 0 \end{pmatrix} \quad (2.65)$$

with the gaugino masses M_1, M_2 , the weak mixing angle θ_W and $\tan \beta$, the ratio of two Higgs vacuum expectation values. The physical masses of the neutralinos are given by the eigenvalues of this matrix. The neutralino mass eigenstates are denoted as $\chi_1^0, \chi_2^0, \chi_3^0, \chi_4^0$ with $m_{\chi_1^0} \leq m_{\chi_2^0} \leq m_{\chi_3^0} \leq m_{\chi_4^0}$.

The mass matrix for the charginos given by:

$$M^{(c)} = \begin{pmatrix} M_2 & \sqrt{2}M_W \sin \beta \\ \sqrt{2}M_W \cos \beta & \mu \end{pmatrix} \quad (2.66)$$

leads to two chargino eigenstates $m_{\chi_{1,2}^\pm}$ with the mass eigenvalues

$$m_{\chi_{1,2}^\pm}^2 = \frac{1}{2}M_2^2 + \frac{1}{2}\mu^2 + M_W^2 \mp \frac{1}{2}\sqrt{(M_2^2 - \mu^2)^2 + 4M_W^4 \cos^2 2\beta + 4M_W^2(M_2^2 + \mu^2 + 2M_2\mu \sin 2\beta)} \quad (2.67)$$

The gluino is the only color octet fermion. Since the SU(3) is unbroken, the gluino does not mix with other MSSM particles. The mass of the physical particle is defined by the gaugino mass parameter $m_{\tilde{g}} \equiv M_3$.

Approximately, the gaugino mass parameters at the electroweak scale are:

$$M_3 \simeq 2.7m_{1/2} \quad (2.68)$$

$$M_2 \simeq 0.8m_{1/2} \quad (2.69)$$

$$M_1 \simeq 0.4m_{1/2} \quad (2.70)$$

The physical masses of the neutralinos are obtained by diagonalizing the mass matrix Eq. 2.65. In the mSUGRA model, the lightest neutralino is dominantly bino-like and the next-to-lightest neutralino is mostly wino-like, with masses close to M_1 and M_2 , respectively. The mass of the lightest chargino is approximately given by M_2 . Hence the masses of the next-to-lightest neutralino and the lightest chargino are similar, and approximately two times the mass of the lightest neutralino.

Sleptons and Squarks

The masses of left-handed and right-handed fermions are equal. But their superpartners are bosons and the masses of left-handed and right-handed sfermions can be different:

$$\tilde{m}_{e_L}^2 = \tilde{m}_{L_i}^2 + m_{E_i}^2 + M_Z^2 \cos(2\beta) \left(-\frac{1}{2} + \sin^2 \theta_W \right) \quad (2.71)$$

$$\tilde{m}_{\nu_L}^2 = \tilde{m}_{L_i}^2 + M_Z^2 \cos(2\beta) \left(\frac{1}{2} \right) \quad (2.72)$$

$$\tilde{m}_{e_R}^2 = \tilde{m}_{E_i}^2 + m_{E_i}^2 - M_Z^2 \cos(2\beta) (\sin^2 \theta_W) \quad (2.73)$$

$$\tilde{m}_{u_L}^2 = \tilde{m}_{Q_i}^2 + m_{U_i}^2 + M_Z^2 \cos(2\beta) \left(+\frac{1}{2} + \sin^2 \theta_W \right) \quad (2.74)$$

$$\tilde{m}_{d_L}^2 = \tilde{m}_{Q_i}^2 + m_{D_i}^2 + M_Z^2 \cos(2\beta) \left(-\frac{1}{2} + \frac{1}{3} \sin^2 \theta_W \right) \quad (2.75)$$

$$\tilde{m}_{u_R}^2 = \tilde{m}_{U_i}^2 + m_{U_i}^2 + M_Z^2 \cos(2\beta) \left(\frac{2}{3} \sin^2 \theta_W \right) \quad (2.76)$$

$$\tilde{m}_{d_R}^2 = \tilde{m}_{D_i}^2 + m_{D_i}^2 - M_Z^2 \cos(2\beta) \left(\frac{1}{3} \sin^2 \theta_W \right) \quad (2.77)$$

On the right side of the equations, the terms denoted as \tilde{m} are calculated with the RGE, the mass terms m are the fermion masses. The index i denotes the three generations.

Furthermore non-negligible Yukawa couplings lead to a mixing between the electroweak eigenstates and the mass eigenstates of the third generation sleptons and squarks. Due to small Yukawa couplings the mixing is negligible for the first and second generation. Therefore the mass eigenstates corresponds to the interaction eigenstates, which have been introduced above. The mass matrices for the third generation reads as:

$$\mathcal{M}^{\tilde{t}} = \begin{pmatrix} \tilde{m}_{t_L}^2 & m_t(A_t - \mu \cot \beta) \\ m_t(A_t - \mu \cot \beta) & \tilde{m}_{t_R}^2 \end{pmatrix} \quad (2.78)$$

$$\mathcal{M}^{\tilde{b}} = \begin{pmatrix} \tilde{m}_{b_L}^2 & m_b(A_b - \mu \tan \beta) \\ m_b(A_b - \mu \tan \beta) & \tilde{m}_{b_R}^2 \end{pmatrix} \quad (2.79)$$

$$\mathcal{M}^{\tilde{\tau}} = \begin{pmatrix} \tilde{m}_{\tau_L}^2 & m_\tau(A_\tau - \mu \tan \beta) \\ m_\tau(A_\tau - \mu \tan \beta) & \tilde{m}_{\tau_R}^2 \end{pmatrix} \quad (2.80)$$

The mass eigenstates of the third generation are:

$$m_{\tilde{t}_{1,2}}^2 = \frac{1}{2} (\tilde{m}_{t_L}^2 + \tilde{m}_{t_R}^2) \pm \sqrt{\frac{1}{4} (\tilde{m}_{t_L}^2 - \tilde{m}_{t_R}^2)^2 + m_t^2 (A_t - \mu \cot \beta)^2} \quad (2.81)$$

$$m_{\tilde{b}_{1,2}}^2 = \frac{1}{2} (\tilde{m}_{b_L}^2 + \tilde{m}_{b_R}^2) \pm \sqrt{\frac{1}{4} (\tilde{m}_{b_L}^2 - \tilde{m}_{b_R}^2)^2 + m_b^2 (A_b - \mu \tan \beta)^2} \quad (2.82)$$

$$m_{\tilde{\tau}_{1,2}}^2 = \frac{1}{2} (\tilde{m}_{\tau_L}^2 + \tilde{m}_{\tau_R}^2) \pm \sqrt{\frac{1}{4} (\tilde{m}_{\tau_L}^2 - \tilde{m}_{\tau_R}^2)^2 + m_\tau^2 (A_\tau - \mu \tan \beta)^2} \quad (2.83)$$

Higgs Bosons

In the MSSM, one needs at least two Higgs doublets to give mass to all matter particles. Considering the following Higgs doublets

$$H_1 = \begin{pmatrix} H_1^0 \\ H_1^- \end{pmatrix} = \begin{pmatrix} v_1 + \frac{1}{\sqrt{2}}(\phi_1 + i\phi_2) \\ H_1^- \end{pmatrix} \quad (2.84)$$

$$H_2 = \begin{pmatrix} H_2^+ \\ H_2^0 \end{pmatrix} = \begin{pmatrix} H_2^+ \\ v_2 + \frac{1}{\sqrt{2}}(\phi_3 + i\phi_4) \end{pmatrix} , \quad (2.85)$$

with the vacuum expectation value v_1, v_2 of the neutral components, the Higgs potential reads as:

$$\begin{aligned} V_{\text{Higgs}} &= m_1^2 |H_1|^2 + m_2^2 |H_2|^2 - m_3^2 (H_1 H_2 + h.c.) \\ &+ \frac{g^2 + g'^2}{8} (|H_1|^2 - |H_2|^2)^2 + \frac{g^2}{2} |H_1^* H_2|^2 . \end{aligned} \quad (2.86)$$

In the SM the non-trivial minimum of the Higgs potential is introduced ad-hoc by requiring the coefficient μ^2 in the potential Eq. 2.26. However in the MSSM the Higgspotential V_{Higgs} depends on the mass parameters

$$\begin{aligned} m_1^2 &= m_{H_1}^2 + \mu^2 \\ m_2^2 &= m_{H_2}^2 + \mu^2 \\ m_3^2 &= Bm_0\mu . \end{aligned} \quad (2.87)$$

In order to break the electroweak symmetry, the Higgs potential V_{Higgs} must have a non-trivial minimum. This requirement is only fulfilled if the mass parameters provide the conditions

$$m_1^2 m_2^2 < m_3^4 \quad (2.88)$$

$$m_1^2 + m_2^2 > 2m_3^2 . \quad (2.89)$$

At the GUT scale, the mass parameters are defined as $m_1^2 = m_2^2 = m_0^2 + \mu^2$. Hence, at the GUT scale the Higgs potential has no non-trivial minimum and thus the electroweak symmetry breaking does not take place. However, the energy dependency of the mass parameters described by the RGE result in values of m_1^2 and m_2^2 , which fulfil the requirements Eq. 2.88 and Eq. 2.89. Since radiative corrections to the mass parameters cause the energy dependency, this phenomenon is known as radiative spontaneous symmetry breaking. The hierarchy problem, i.e. the large difference of the GUT scale and the electroweak scale can be explained by this mechanism, since those radiative corrections depend logarithmic on the energy.

In contrast to the Standard Model, where only one physical Higgs boson is predicted, the requirement of two Higgs doublets lead to five physical Higgs bosons in the MSSM . Namely

the two scalar, neutral and CP-even Higgs bosons h and H , the A Higgs boson, which is pseudoscalar, neutral and CP-odd and two scalar, charged Higgs bosons H^\pm .

Their mass matrices read as:

$$M_A^2 = m_1^2 + m_2^2 \quad (2.90)$$

$$M_{H,h}^2 = \frac{1}{2} \left(M_A^2 + M_Z^2 \pm \sqrt{(M_A^2 + M_Z^2)^2 - 4M_A^2 M_Z^2 \cos^2 2\beta} \right) \quad (2.91)$$

$$M_{H^\pm}^2 = M_A^2 + M_W^2 \quad . \quad (2.92)$$

By convention the h Higgs boson is always the lightest Higgs boson $m_h < m_H$. The masses of the lightest Higgs can be derived at tree level as:

$$m_h^2 \leq M_Z |\cos 2\beta| \leq M_Z^2 \quad . \quad (2.93)$$

This region is already excluded by the experimental limit on the Higgs bosons mass at 95% confidence level:

$$m_h > 114 \text{ GeV} \quad [3]. \quad (2.94)$$

However after including radiative corrections, the mass of the lightest Higgs boson is shifted upwards by a substantial amount.

2.3.4 Experimental Constraints

Since the time SUSY was proposed, many experiments have already been searching for signs of supersymmetric particles. Provided that supersymmetry is realized in nature, the consequences should be seen in various different fields. Obviously the SUSY particles should have been directly produced in modern collider experiments at the LEP and at the Tevatron. Furthermore, their presence should result in indirect effects of radiative corrections or gravitational force. Additional constraints come from the motivation of the theory itself.

- **Coupling unification:** One of the main motivation for supersymmetry is the unification of the coupling constants at the GUT scale. The coupling constants unify only if the scale of SUSY breaking and hence the mass of the SUSY particles is in the order of 1 TeV [36].
- **Anomalous magnetic moment of the muon:** The indirect effects of SUSY particles are checked in the measurements of the anomalous magnetic moment of the muon. The anomalous magnetic moment of the muon is sensitive to radiative corrections both from SM and SUSY particles and has been measured very precisely at the Brookhaven National Laboratory as:

$$\alpha_\mu^{\text{exp}} = 116592080(63) \cdot 10^{-3} \quad [39]. \quad (2.95)$$

The deviation from the SM predictions is in the order of 3.2σ :

$$\Delta\alpha_\mu = \alpha_\mu^{\text{exp}} - \alpha_\mu^{\text{theo}} = (29 \pm 9) \cdot 10^{-10} \quad [33], \quad (2.96)$$

which is still consistent with SUSY contributions, if μ has a positive sign $\mu > 0$ [3].

- **B physics:** Another indirect measurement sensible to the influence of SUSY particles are the rates of rare decays of B mesons into a strange meson and a photon $B_s \rightarrow s\gamma$ and of the B meson to an opposite sign muon pair $B_s \rightarrow \mu\mu$.

The inclusive decays rate of $b \rightarrow s\gamma$ is measured with a very high precision at the BaBar [40], CLEO [41] and BELLE [42] experiments, resulting in the present world average of:

$$\text{BR}^{\text{exp}}(b \rightarrow s\gamma) = (3.52 \pm 0.32) \cdot 10^{-4} \quad [3]. \quad (2.97)$$

The SM prediction of the inclusive decay rate is only slightly lower:

$$\text{BR}^{\text{theo}}(b \rightarrow s\gamma) = (3.29 \pm 0.33) \cdot 10^{-4} \quad [3]. \quad (2.98)$$

This result imposes severe constraints on the parameter space, especially for the case of large $\tan\beta$. However, there remains still a window for SUSY. [43]

Also the decays $B_s \rightarrow \mu\mu$ can have large contributions from SUSY particles. The Tevatron experiments CDF and D0 have both measured this decay rate, resulting in the limit

$$\text{BR}^{\text{exp}}(B_s^0 \rightarrow \mu^+\mu^-) \leq 5.8 \cdot 10^{-8} \quad [3], \quad (2.99)$$

where the B_s^0 decay rate is just one order of magnitude above theoretical predictions:

$$\text{BR}^{\text{theo}}(B_s^0 \rightarrow \mu^+\mu^-) \leq 3.42 \cdot 10^{-9} \quad [3]. \quad (2.100)$$

So B meson physics is a productive field in particle physics, probing the SM with a very high precision.

- **Cosmology:** R -parity conserving SUSY models with neutralino-LSP provide a suitable candidate for the explanation of cold dark matter (CDM), since in this models the LSP is stable and only weak and gravitationally interacting. The expected LSP relic density can be calculated SUSY model depended and compared with the precisely measured value of the dark matter density. Hence, the measurement of the CDM relic density can be reinterpreted as measurements constraining the SUSY model.

Recent measurements of the WMAP experiment have determined the amount of the dark matter in the universe as 23% [5]. From this result it can be concluded that the contribution of each relict particle χ has to obey the constraint $\Omega_\chi h_0^2 \approx 0.12$, where the Hubble constant h_0 is assumed to be $h_0 \approx 0.7$. This requirement leaves a narrow band in the SUSY parameter space, which is shown in Fig. 2.3 for $\tan\beta = 51$ [37].

Direct searches for dark matter are experiments dedicated to the observation of the energetic recoiling ions produced by the scattering of weakly interacting massive particles (WIMP) from our galactic halo on terrestrial targets. At present,

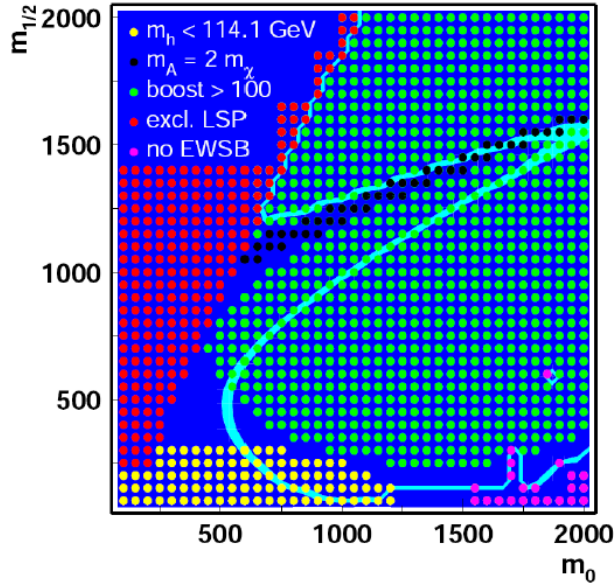


Figure 2.3: Allowed region of the SUSY parameter space from the WMAP high precision relict density measurements for $\tan\beta = 51$ is represented by the blue band [37]. The red points on the left upper corner show the region in the parameter space, where the stau is the lightest supersymmetric particle. Furthermore, the Higgs boson mass limit is marked with yellow points in the lower left region.

the CDMS [44] and XENON [45] experiments have achieved the best sensitivities. Present limits are just starting to probe the 10^{-8} pb range where an important class of supersymmetric models relevant for LHC are lying [46]. Current supersymmetric model predictions for the WIMP-nucleon cross-section are typically in the range from 10^{-8} to 10^{-10} pb [46]. Both collaborations are developing more ambitious projects aiming at a cross section in the range of 10^{-9} pb and eventually 10^{-10} pb [46]. The EDELWEISS experiment should reach a sensitivity of 5×10^{-8} pb by the end of 2009 [46].

- **Collider experiments:** The experiments at the Large Electron Positron Collider (LEP) and Tevatron Collider have been searching for direct production of SUSY particles in various different analyses. No evidence for these particles has been found so far.

The constraints obtained with the ALEPH [50], DELPHI [51], L3 [52] and OPAL [53] experiments at LEP are shown in Fig. 2.4. The final results are obtained by combining the searches in e^+e^- collisions at the center of mass energy $\sqrt{s} \leq 209$ GeV for pair production of various SUSY particles (e.g. $e^+e^- \rightarrow \tilde{\tau}\tilde{\tau}, \tilde{e}\tilde{e}, \chi_1^0\chi_1^0$) with searches for the lightest scalar neutral Higgs boson in the $e^+e^- \rightarrow hZ$ reaction as well as with the latest electroweak results [47].

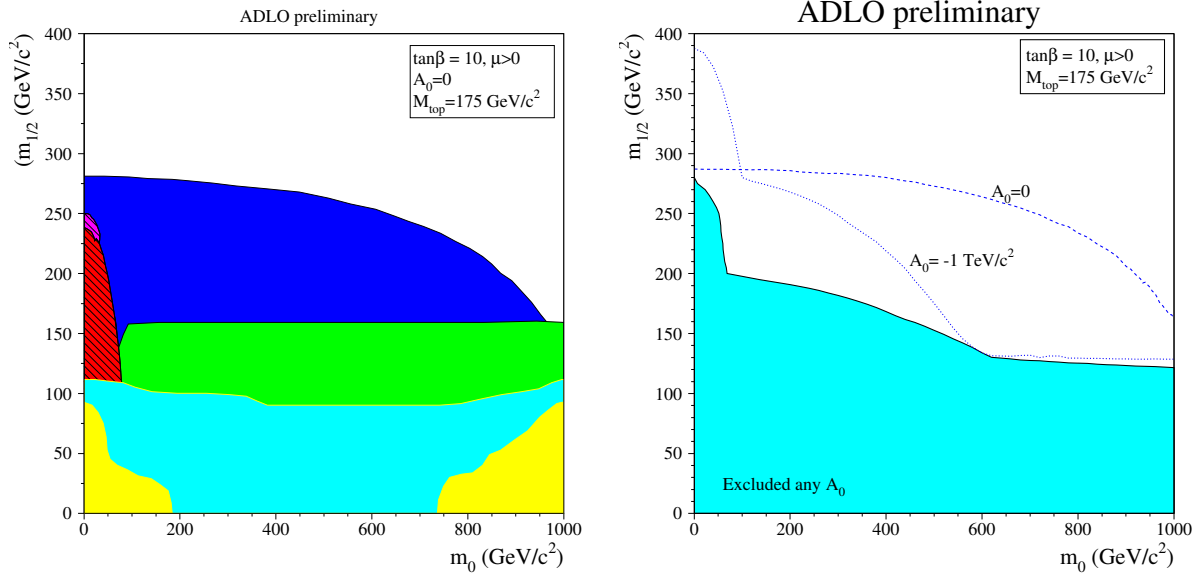


Figure 2.4: LEP SUSY constraints in the m_0 - $m_{1/2}$ plane for $\tan\beta = 10$, $\mu > 0$, (L) $A_0 = 0$ and (R) $A_0 = 0$, $A_0 < -1$ TeV and for any value of A_0 [47]. In the yellow region no electroweak symmetry breaking (EWSB) or tachyonic particles appears, the light blue represent regions inconsistent with the measurement of the electroweak parameters at LEP1, the green regions are excluded by the chargino searches, the red regions are excluded by the selectron or stau standard searches, the dark blue regions are excluded by the search for hZ , the brown regions are excluded by the neutralino stau cascade searches and magenta represents regions excluded by the search for heavy stable charged particles.

In proton-antiproton collisions at center of mass energies at $\sqrt{s} = 1.96$ TeV, the Tevatron experiments D0 [54] and CDF [55] have been searching for SUSY in squark and gluino and in direct gaugino production. Probing the gluino and squark particle masses $M \sim 400$ GeV, the searches in squark and gluino production with 2, 3, or 4 jets and missing transverse energy have extended the LEP limits [48, 49]. Fig. 2.5 shows the exclusion limits obtained by the D0 and CDF collaborations. The searches for trileptons from associated chargino-neutralino production resulted in the currently world most largest exclusion limit in the m_0 - $m_{1/2}$ plane [13, 14]. Fig. 2.6 presents the corresponding exclusion limits from the CDF and D0 experiments. The trilepton analyses at the Tevatron are discussed in Section 5.9.1.

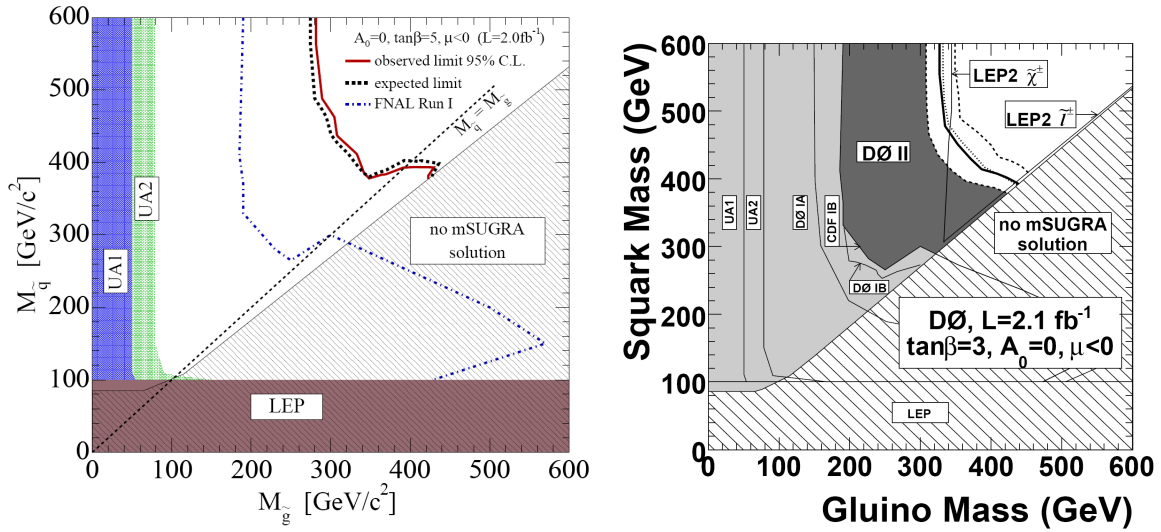


Figure 2.5: Exclusion limits from the squark-gluino searches at the Tevatron from CDF (L) and D0 (R) [48, 49]. The exclusion limit is shown as a function of squark and gluino masses in the mSUGRA scenario with $A_0 = 0, \mu < 0$ and $\tan\beta = 5$ (L) and $\tan\beta = 3$ (R). The limits are compared to previous results from SPS and LEP experiments at CERN.

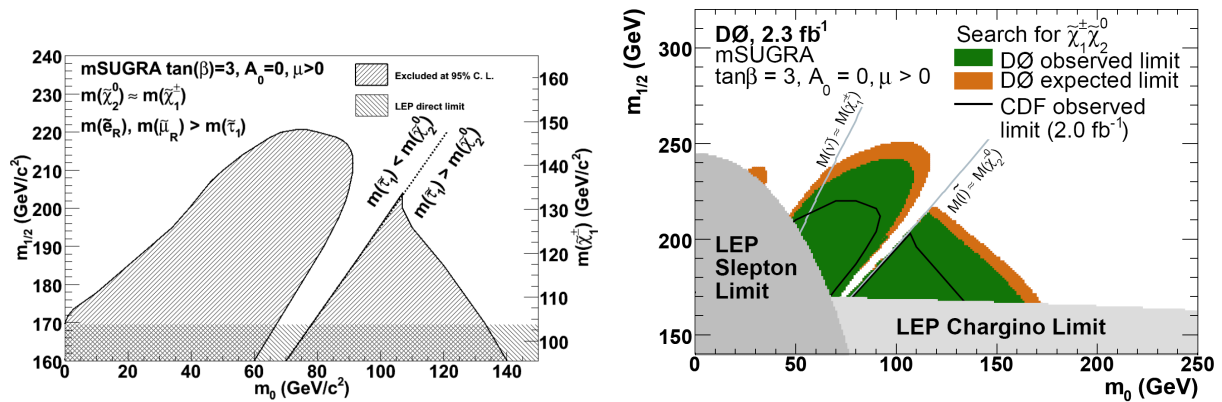


Figure 2.6: Exclusion limits from the trilepton searches at the Tevatron from CDF (L) and D0 (R) [13, 14]. The searches are discussed in detail in Section 5.9.1.

Chapter 3

LHC and the CMS-Experiment

3.1 Large Hadron Collider

At CERN, the European Organization of Nuclear Research in Geneva, the worlds' largest particle accelerator Large Hadron Collider (LHC) has been built in the 27 km long tunnel of the former Large Electron Positron (LEP) Collider at a depth about 100 m underground.

In contrast to LEP, which collided electrons and positrons, LHC accelerates and collides protons. The energy loss of accelerated charged particles due to synchrotron radiation limited the center of mass energy of LEP to $\sqrt{s} = 209$ GeV. Since the synchrotron radiation is antiproportional to the mass of the accelerated particle as $\propto Em^{-4}$ and the mass of the proton is 2000 times the mass of the electron, protons can be accelerated to much higher energies without suffering from synchrotron radiation.

At the LHC, two separate proton beams are collided at four interaction points. In contrast to the electron, the proton is a composite object of partons, the quarks and gluons. The variable x measures the fraction of the proton momentum which is carried by the parton. The structure functions of the partons decrease rapidly with increasing x . Since each parton carries only a fraction of the proton momentum, the beam energy at hadron colliders has to be foreseen to be well above the energy scale of the desired interactions. The LHC has been designed to reach proton collisions at a center of mass energy of $\sqrt{s} = 14$ TeV. This is seven times higher than the currently worlds' highest energy accelerator, the Tevatron Collider at the Fermi National Accelerator Laboratory (FermiLab) near Chicago, which accelerates protons and antiprotons at a center of mass energy of $\sqrt{s} = 1.96$ TeV.

Hence the LHC will be able to validate the Standard Model of particle physics and look for physics beyond the Standard Model at the highest ever reached energy level. Experiments at the LHC will search for the Higgs particle and for new physics phenomena at the TeV scale such as supersymmetry or extra dimensions. The rate of physics events produced in

the proton-proton collisions is

$$\mathcal{N} = \sigma \cdot \mathcal{L} \quad , \quad (3.1)$$

with the cross section of the considered physical process σ and the luminosity \mathcal{L} . Since the cross section of parton-parton scattering decreases antiproportional to the energy as $\sigma \propto E^{-2}$, the luminosity has to be increased by E^2 to compensate the decreasing cross section. The luminosity of the LHC is calculated assuming two bunches n_1 and n_2 of particles colliding with a frequency f as:

$$\mathcal{L} = f \frac{n_1 n_2}{4\pi \sigma_x \sigma_y} \quad , \quad (3.2)$$

where σ_x, σ_y denote the gaussian transverse profiles of the beam.

In order to reach the designed luminosity $\mathcal{L} = 10^{34} \text{ cm}^{-2}\text{s}^{-1}$ of the LHC, the bunch crossing frequency, the number of proton bunches as well as the number of protons per bunch have to be accordingly chosen. At the nominal intensity each beam will consist of around 2800 bunches with up to 1.15×10^{11} protons per bunch and the bunch spacing is 25 ns corresponding to bunch crossing frequency of 40 MHz. With the high number of protons per bunch, the average number of inelastic collisions between protons per bunch-crossing is large ($\sim 10 - 20$), which are called pile-up events. This complicates the search for rare interesting physic processes, since they will be contaminated by pile-up events. Overall the designed luminosity leads to around 1 billion proton-proton interactions per second.

The LHC will initially run at an energy of 3.5 TeV per beam after start up in November 2009 until a significant data sample has been collected. Thereafter the energy will be taken towards 5 TeV per beam. At the end of 2010, the LHC will be run with lead ions for the first time. Afterwards the LHC will shut down and work will begin on moving the machine towards 7 TeV per beam [56].

In order to reach the corresponding energy per beam, several LHC accelerator components successively increase the energy of the protons. First of all, the linear accelerator Linac2 generates protons with 50 MeV. Then the Proton Synchrotron Booster (PSB) and in turn the Proton Synchrotron (PS) accelerates the protons up to a total energy of 26 GeV. Afterwards the Super Proton Synchrotron (SPS) increases the energy to 450 GeV, before the protons are inserted into the main LHC ring, where the protons circulate inside the beam pipes, which are vacuum tubes in order to avoid collisions with normal matter. Here, eight Radio-Frequency (RF) cavities per beam providing strong electric fields accelerate the protons further. In total 1232 dipole and 392 quadrupole superconducting magnets keep the beam focussed around the circular path. The superconducting magnets are cooled with liquid helium at an operating temperature of $T = 1.9 \text{ K}$.

At the LHC, four particle detectors will measure the proton-proton collisions at the interaction points. The ATLAS [1] experiment and the Compact Muon Solenoid (CMS) are

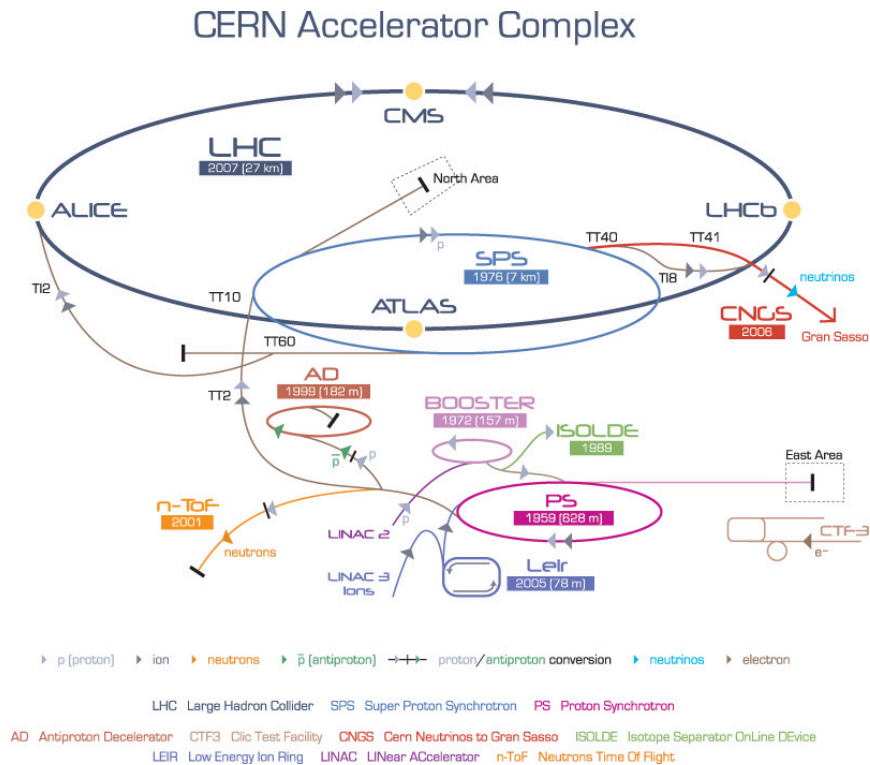


Figure 3.1: CERN accelerator complex [59].

multipurpose detectors, which are designed to cover the various possible range of physics processes, but mainly to discover the Higgs particle and to search for supersymmetry or other physics beyond the Standard Model. The LHCb [57] experiment is a special designed detector for b physics. Since the LHC will also collide lead (Pb) ions, the Large Ion Collider Experiment (ALICE) [58] is build to study the properties of the quark-gluon plasma in heavy ion collisions.

3.2 CMS Experiment

The CMS detector has a length of 24 m, a diameter of 14.6 m and a weight of about 14500 tons. As every modern detector in accelerator experiments, the detector of the Compact Muon Solenoid experiment is composed of several subsystems. Each of the sub-detectors provides different and complementary measurements. In order to achieve the largest possible coverage, the subdetectors are placed in concentric layers around the interaction point of the proton-proton collision. The main distinguishing features of CMS are a high-field solenoid, a full silicon-based inner tracking system and a fully active scintillating crystals-based electromagnetic calorimeter. Figure 3.2 shows the subsystems of the CMS detector.

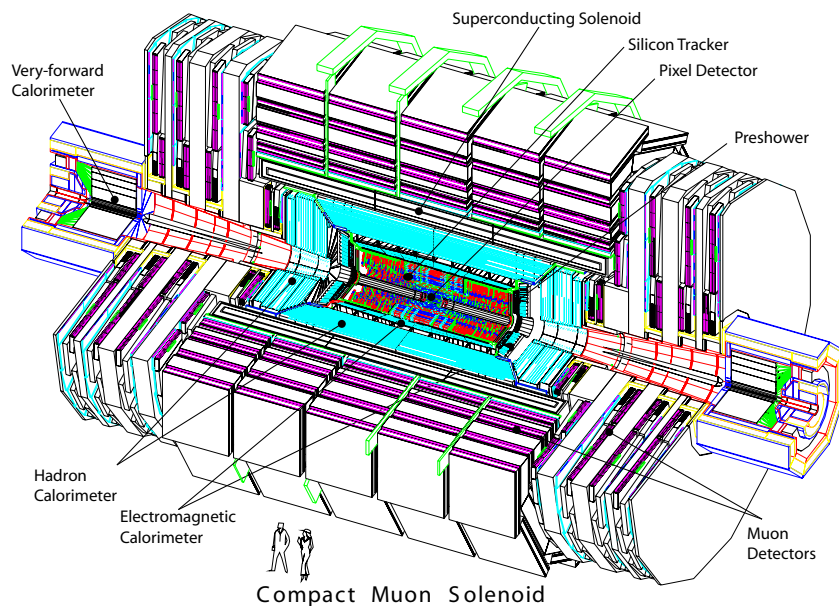


Figure 3.2: Compact Muon Solenoid experiment [60].

The CMS detector meets the requirements of the LHC physics program, namely [60]

- Good muon identification and momentum resolution over a wide range of momenta in the region $|\eta| < 2.5$, good dimuon mass resolution ($\sim 1\%$ at 100 GeV), and the ability to determine unambiguously the charge of muons with $PT < 1$ TeV.
- Good charged particle momentum resolution and reconstruction efficiency in the inner tracker. Efficient triggering and offline tagging of τ 's and b jets, requiring pixel detectors close to the interaction region.
- Good electromagnetic energy resolution, good diphoton and dielectron mass resolution ($\sim 1\%$ at 100 GeV), wide geometric coverage ($|\eta| < 2.5$), measurement of the direction of photons and/or correct localization of the primary interaction vertex, π^0 rejection and efficient photon and lepton isolation at high luminosities.
- Good MET and dijet mass resolution, requiring hadron calorimeters with a large hermetic geometric coverage ($|\eta| < 5$) and with fine lateral segmentation ($\Delta\eta \times \Delta\phi < 0.1 \times 0.1$).

As shown pictorially in Fig. 3.3 particles emerging from collisions first meet the tracking system, made entirely of silicon, that charts the position of the charged particles moving through the detector and allows to measure their momentum. Outside the tracking system are calorimeters that measure the energy of particles. The tracking system should interfere

with the particles as little as possible, whereas the calorimeters are designed to stop the particles in their tracks. The electromagnetic calorimeter (ECAL) measures the energy of photons and electrons whereas the hadron calorimeter (HCAL) is designed principally to detect any particle made up of quarks. The size of the magnet allows the tracker and calorimeters to be placed inside its coil, resulting in an overall compact detector. In the outer part of the detector, the iron magnet return yoke confines and guides the magnetic field. All particles, except muons and only weakly interacting particles, such as neutrinos, should be stopped within the calorimeters and the iron return yoke. Hence since only muons will be measured in the muon system, muons provide a very clean signature, whereas on the contrary electrons and photons measured in the ECAL require sophisticated techniques for discrimination and identification.

Since muon final states form a very clean signature for many of the interesting processes that will be searched for at LHC, the detection of muons is among the highest priorities for CMS. Concerning the measurement of the muon momentum the choice of the magnetic field configuration is an important issue. The CMS collaboration decided to use a solenoid magnet which produces a strong magnetic field along the beam axis bending the charged particles in the transverse plane. The muon momentum reconstruction depends on the strength of the magnetic field B and on its length L as:

$$\frac{\sigma_{PT}}{PT} = \frac{\sigma_s}{s} = \sigma_s \frac{8PT}{0.3BL^2} \quad , \quad (3.3)$$

with the transverse momentum of the particle PT and the sagitta s , or amount of bending, of the particle track inside the magnetic field. Hence the precision of the momentum measurement is proportional to $1/(BL^2)$. Whereas the ATLAS experiment uses a rather moderate magnetic field and a large detector, the CMS experiment uses a high field strength of 3.8 Tesla and a rather compact detector.

3.2.1 Coordinate System

Before going into details about the detector components, the chosen coordinate system adopted by CMS to describe the properties of reconstructed physics objects needs to be introduced.

- The coordinate system has the origin at the nominal collision point inside the CMS detector.
- The beam axis is the z -axis, the y -axis points vertically upwards and the x -axis of the coordinate system points radially inward towards the center of the LHC.
- The polar angle θ is measured from the z -axis and the azimuthal angle ϕ is defined as the angle from the x -axis in the x - y -plane.

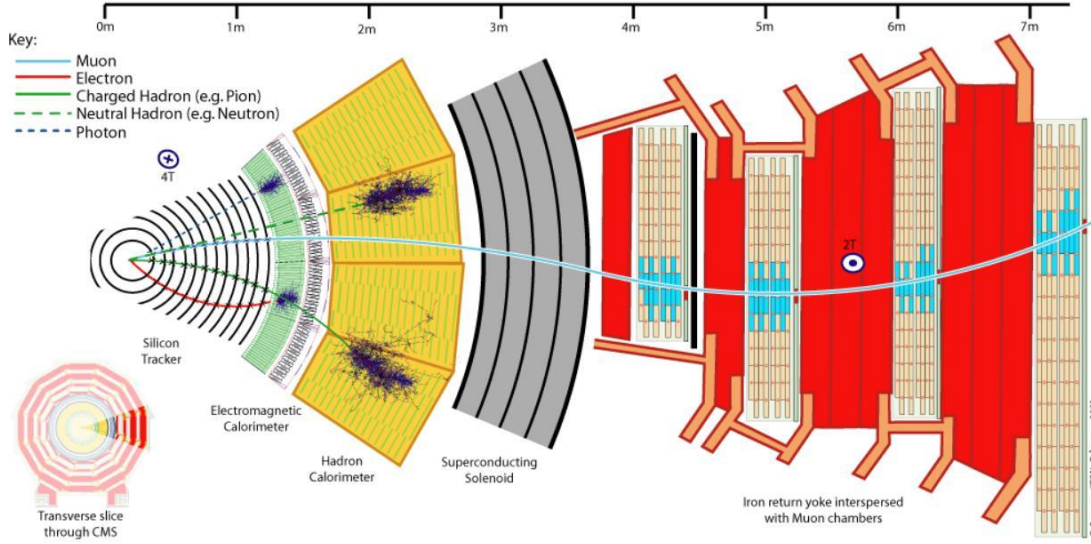


Figure 3.3: Slice of the CMS detector and pictorial presentation of the measurement of electrons, photons, hadrons (e.g. pions) and muons in the different subsystems [61]. Electrons and photons deposit their whole energy in the electromagnetic calorimeter, whereas hadrons are measured in the hadron calorimeter. All particles, except for muons and only weakly interacting particles will be stopped in the inner region of the detector. Muons pass the detector material including the superconducting solenoid and are detected in the muon system. Therefore muons provide a very clean signature. On the contrary electrons and photons have to be distinguished with sophisticated techniques.

- The pseudorapidity defined as:

$$\eta = -\ln \left[\tan \left(\frac{\theta}{2} \right) \right] \quad (3.4)$$

is preferably used at hadron-hadron instead of the polar angle, since it is invariant under the momentum along the beam axis. Consequently the particle production is nearly constant as a function of η .

- The transverse momentum PT and transverse energy ET are computed as:

$$PT = \sqrt{p_x^2 + p_y^2} \quad \text{and} \quad ET = \sqrt{E_x^2 + E_y^2} \quad . \quad (3.5)$$

- In a reconstructed event the imbalance of energy measured in the transverse plane called missing transverse energy is denoted by MET.

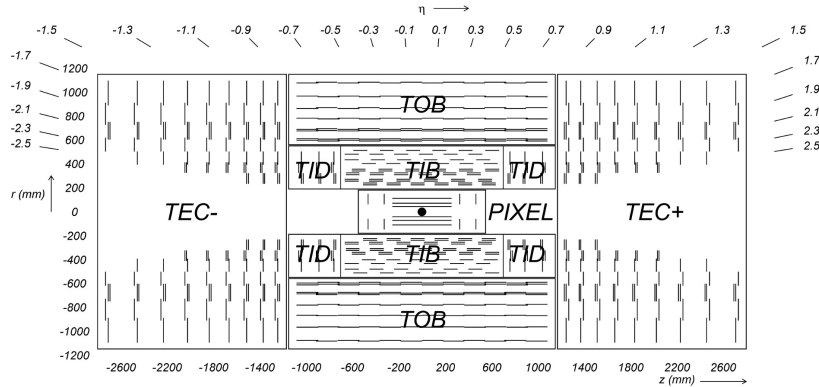


Figure 3.4: Layout of the CMS tracking system [2]. Each line represents a detector module, double lines indicate stereo modules.

3.2.2 Inner Tracking System

Starting from the beam pipe, the first detector component is the tracking system, which provides a precise and efficient measurement of the trajectories of charged particles with a high momentum resolution. The tracking system offers high efficiencies also for low momentum particles ($p = 1 - 5$ GeV) which is essential e.g. for studies with muon final states, since muons from SM bosons and their SUSY partners can be identified by the low particle activity around the muon track. Moreover it provides a precise reconstruction of their vertex position used to identify decays of heavy hadrons. The track reconstruction efficiency, PT resolution and vertex resolution is presented in the appendix in Fig. A.1 and Fig. A.2, respectively.

A layout of the CMS tracker is shown in Fig. 3.4. The outer radius of the CMS tracker extends up to nearly 110 cm, while its total length is approximately 540 cm. The pseudo-rapidity coverage corresponds to $|\eta| < 2.5$. The design of the tracking system is strongly related to the challenging experimental conditions at the LHC, where the large number of pile up events at the designed luminosity leads to a huge amount (~ 1000) of charged particles produced per bunch crossing. In order to identify the particle tracks and assign them to the corresponding bunch crossing, a high granularity and fast response is mandatory. Additionally the tracking system has to stay unharmed by the high radiation environment and the material budget has to be minimized in order to limit secondary phenomena like multiple scattering, bremsstrahlung, photon conversions and nuclear interactions.

To meet the mentioned requirements, the tracking system is composed of silicon pixel detectors placed in the inner regions up to $r < 10$ cm, where the occupancy is highest, followed by silicon microstrip detectors.

Pixel Detector

The silicon pixel detector is composed of a total of 66 million pixels with a size of $100\ \mu\text{m} \times 150\ \mu\text{m}$, which are arranged in the barrel in three concentric cylinders at mean radii of 4.4 cm, 7.3 cm and 10.2 cm around the beam axis and in the endcaps in two layers perpendicular to the beam axis in the z direction at ± 34.5 cm and ± 46.5 cm. Charged particles passing through the silicon pixel create electron-hole pairs affected both by the reverse bias which is applied to the pixels and the magnetic field of the CMS solenoid. Consequently the drifting electron-hole pairs experience a Lorentz force

$$\mathbf{F} = q(\mathbf{E} + \mathbf{v} \times \mathbf{B}) \quad , \quad (3.6)$$

with the charge of the electron q , the magnitude of the electric field E , the electron drift velocity v and the magnitude of the magnetic field B . Since in the barrel the magnetic field is perpendicular to the electric field, the charge carriers are deflected at an angle to the electric field lines known as the Lorentz angle, resulting in a better resolution than the width of each individual pixel because the charge is shared between several pixels. However, in order to benefit from the same effect in the endcaps, the pixels in the endcaps are not mounted perpendicular to the beam pipe in the disks, but rotated by 20° about their radial symmetry axis, known as the turbine-blade geometry. The position resolution is $\sim 10\ \mu\text{m}$ in the r - ϕ and $\sim 20\ \mu\text{m}$ in the z direction [62].

Strip Detector

The silicon strip detector contains a total of 9.6 million silicon strips. As shown in Figure 3.4, the silicon strip detector is subdivided in the inner barrel (TIB), the tracker outer barrel (TOB), the tracker inner disks (TID) and the tracker endcaps (TEC). The TIB consists of 4 layers of silicon sensors with a thickness of $320\ \mu\text{m}$ and a strip pitch varying from 80 to $120\ \mu\text{m}$. Since the strips are parallel to the beam axis, the z coordinate cannot be determined by a single strip detector. Therefore the first 2 layers are made with stereo modules i.e. two detectors are placed back to back with the strips at an angle of 0.1 rad to each other. In the TIB the resolution is between 23 and $34\ \mu\text{m}$ in the r - ϕ direction and $230\ \mu\text{m}$ in z . Due to smaller radiation levels in the outer region, the thickness of the silicon sensors is chosen as $500\ \mu\text{m}$ together with a wider strip pitch of 120 to $180\ \mu\text{m}$. Also in the TOB the first two layers are made with stereo modules. The resolution is between 35-52 μm in the r - ϕ direction and $530\ \mu\text{m}$ in z . Stereo modules are attached in the first two layers of the TID and in the first two as well as the fifth layer of the TOB. The strips in the TID and TEC are perpendicular to the beam axis with a thickness of $320\ \mu\text{m}$ in the TID and the first three layers of the TOB and $530\ \mu\text{m}$ for the rest of the TOB. [63]

3.2.3 Electromagnetic Calorimeter

The electromagnetic calorimeter (ECAL) is designed to measure electrons and photons with high accuracy and contributes to the jet energy measurement by determination of the

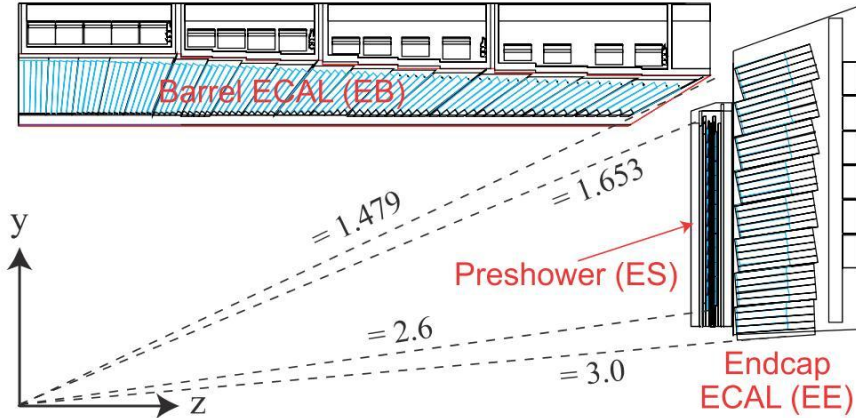


Figure 3.5: Layout of one quarter of the electromagnetic calorimeter (ECAL) [60].

electromagnetic component of jets. The ECAL consists of 75848 lead tungstate (PbWO_4) crystals, a material with a high density $\sim 8.3 \text{ g/cm}^3$, short radiation length $X_0 = 0.89 \text{ cm}$ and small Moliere radius 2.2 cm, giving the scale of the transverse dimension of the fully contained electromagnetic showers. Since a smaller Moliere radius means better shower position resolution and better shower separation due to a smaller degree of shower overlaps, the choice of lead tungstate enabled a compact design for the ECAL without suffering from a worse shower resolution. Furthermore, the material has a short scintillation light decay time, since in 25 ns $\sim 80\%$ of the light is collected.

Fig. 3.5 shows the electromagnetic calorimeter subdivided in the barrel part (EB) made of 61200 lead tungstate crystals and two endcaps (EE) each made of 7324 crystals. The EB with an inner radius 129 cm covers the region $|\eta| < 1.479$. The crystals in the EB have a front face cross-section of $22 \times 22 \text{ mm}^2$, each crystal covers a range of $\Delta\eta \times \Delta\phi = 0.00174 \times 0.00174$. The length of 230 mm corresponds to a radiation length of $\sim 26 X_0$. The electromagnetic calorimeter in the endcaps covers the pseudorapidity range of $1.479 < |\eta| < 3.0$ with crystals each having a front face cross-section of $28.6 \times 28.6 \text{ mm}^2$ and a length of 220 mm which corresponds to a radiation length of $\sim 24.7 X_0$. The preshower detector (ES) covers the range $1.653 < |\eta| < 2.6$ and is placed in front of the crystal calorimeter in order to identify neutral pions and to increase the position measurement of electrons and photons. The ES is a two layer sampling calorimeter, the first layer is composed of lead radiators followed by a second layer of silicon strip sensors.

The energy resolution of the ECAL can be parameterized as a function of energy:

$$\left(\frac{\sigma}{E}\right)^2 = \left(\frac{S}{\sqrt{E}}\right)^2 + \left(\frac{N}{E}\right)^2 + C^2, \quad (3.7)$$

where S is the stochastic term that includes the effects of the fluctuations in the photon statistics and the shower containment, N is the noise term that comes from electronics

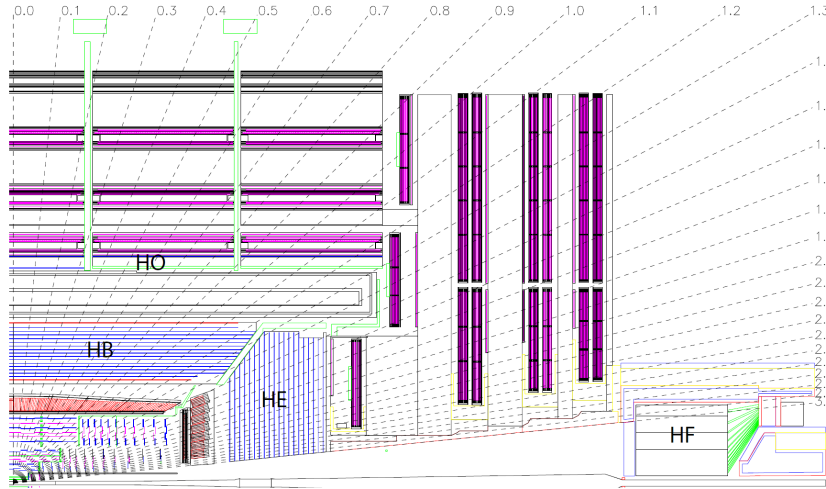


Figure 3.6: Layout of the hadron calorimeter (HCAL) [60].

and pile-up, and C is the constant term that arises due to calibration errors and various systematic errors. The constant term dominates the resolution at high energies, its target value is 0.5% for both the barrel and the endcaps. The energy resolution of the ECAL barrel super-modules was studied with test beam electrons with energies between 20 and 250 GeV. For electrons entering at the center of the studied 3×3 arrays of crystals the energy resolution has been determined as $S = 2.8\%$, $N = 41.5$ MeV and $C = 0.3\%$ [2,64,65].

3.2.4 Hadron Calorimeter

The hadron calorimeter (HCAL) is designed to measure the hadronic component of jets and the missing transverse energy of events together with the ECAL, which requires a good overall coverage. The HCAL is a sampling calorimeter consisting of scintillator tiles with interposed absorber plates made of steel and brass. The hadrons entering the calorimeter interact with the nuclei of the detector material, which creates a hadronic shower measured by the scintillators. The optical signal is detected with hybrid photo diodes (HPD) mounted at the ends of the barrel. Since most of the shower energy is stored in the absorber material, the energy resolution of the HCAL is worse compared to the ECAL resolution.

Fig. 3.6 shows the HCAL subdivided in several subsystems. The hadron barrel (HB) calorimeter covers a pseudorapidity range $|\eta| < 1.3$ and is placed between the EB and the solenoid magnet. The HB consists of two barrels of 18 identical brass alloy absorber plates with wavelength shifting fiber readout (WLS) arranged parallel to the beam axis. The hadron endcap (HE) calorimeter covers the range $1.305 < |\eta| < 3.0$ and consists also of brass and scintillator. In both parts of the calorimeter the segmentation is $\Delta\eta \times \Delta\phi = 0.087 \times 0.087$ except near $|\eta| \sim 3.0$, where the size of the segmentation is doubled. The hadron forward (HF) calorimeter with coverage $3.0 < |\eta| < 5.0$ consists of quartz fibers

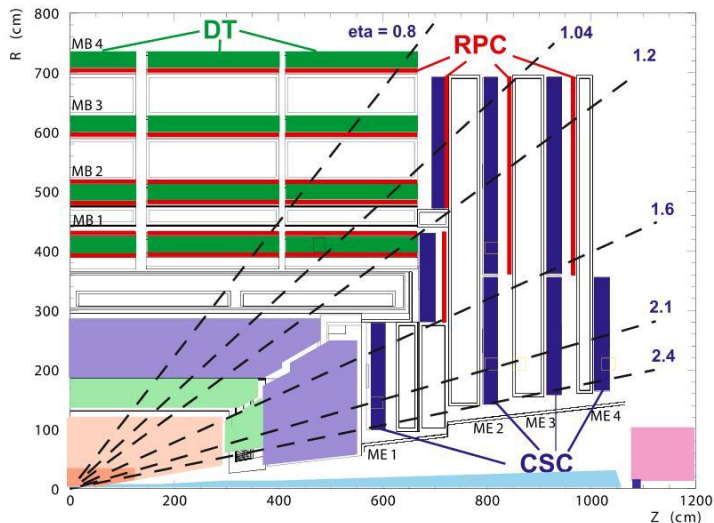


Figure 3.7: Longitudinal view of the CMS muon system [60].

embedded in iron, since in this regions the high rate of hadrons require the use of radiation hard material. Cerenkov light generated in the fibers is transmitted to the photo tubes (PMT). In the barrel region outside the magnet, the hadron outer (HO) calorimeter covers the pseudorapidity range $|\eta| < 1.26$ extending the total depth of the HB in interaction lengths to a minimum of $11 \lambda_I$ [66,67].

3.2.5 Magnet

The superconducting solenoid is 13 m long, has an inner diameter of 6 m and provides a strong magnetic field of 3.8 T. This high field is required demanding a momentum resolution of $\Delta p/p \sim 10\%$ for 1 TeV muons. The magnetic flux is returned by a 1.5 m thick saturated iron yoke, which weights about 10000 tons hosting several layers of muon detectors. At full current energy of ~ 2.6 GJ is stored in the magnet. The tracking system, the electromagnetic calorimeter and the hadronic calorimeter, except for the hadron outer calorimeter are situated inside the superconducting solenoid. [68]

3.2.6 Muon System

Since various interesting processes in physics beyond the Standard Model as well as electroweak, Higgs and B physics lead to muon final states, the muons are considered as a crucial tool for discovery and precision measurements. Hence the reconstruction, identification, correct charge assignment and precise measurement of the momentum of muons along with triggering of events using muons is of highest priority. Since muons are heavy ($m_\mu \sim 105.65$ MeV), they emit less bremsstrahlung radiation compared to electrons. Muons pass the calorimeter system depositing only little amount of ionizing energy, whereas

other particles like electrons, photons and hadrons will store their whole energy and will be stopped in the calorimeter. Only a small amount of hadrons pass the calorimeter (so called punch-through), which can be effectively identified by their energy loss and deflection.

Fig. 3.7 shows the muon system situated outside the magnetic coil as the outermost detector component of CMS. The central barrel part (MB) covering the pseudorapidity range $|\eta| < 1.2$ and the two endcaps (ME) covering the range $0.9 < |\eta| < 2.4$ form the entire muon system, which consists of three types of gaseous detectors. In the MB drift tube chambers are attached, motivated by the low neutron background, low muon rate and low magnetic field, whereas in the region at larger pseudorapidity in the endcaps cathode strip chambers are deployed, since the neutron background, muon rate and magnetic field is high. Additionally in both regions resistive plate chambers (RPC) are used, providing a fast response with good time resolution in order to identify the correct bunch crossing but with a coarser position resolution than DT and CSC.

In the barrel region in total 250 DT chambers organized in four layers are arranged parallel to the beam axis in cylinders interleaved with the iron return yoke. The barrel consists of 5 wheels, each of the 3 innermost stations consists of 12 chambers, with each covering a 30° azimuthal angle, whereas the outer section holds 14 chambers. Depending on the station, each chamber has 1 or 2 RPCs attached. DTs consist of 1.2 mm thick and 9.6 mm long aluminum cathodes with stainless steel anode wires at their center and the cells are filled with a gas mixture of Ar and CO_2 . The electrons generated in the DTs by charged particles move to the anode wire in the center and the high electric field close to the wire amplifies the signal. The track position is measured by the travelling time of the electron, where the maximum drift time is 400 ns and the time resolution is 5 ns. The single point resolution is $\sim 200 \mu\text{m}$. The precision of the measurement of the muon vector is $\sim 100 \mu\text{m}$ in ϕ position and $\sim 1 \text{ mrad}$ in direction for each station. In the central region high PT muons can be reconstructed from up to 44 produced points, when it passes 4 DT chambers. The endcaps hold 4 disks of CSCs and RPCs attached perpendicular to the beam axis consisting in total of 468 CSCs each measuring up to 6 space coordinates in r , ϕ and z . The spatial resolution is typically about $\sim 200 \mu\text{m}$ with an angular resolution in ϕ in the order of 10 mrad. The CSCs have a faster response and a finer segmentation than the DTs. The CSCs are $1 \times 2 \text{ m}^2$ trapezoidal chambers consisting of six gas gaps, all having a plane of radial cathode strips and a plane of gold-plated anode wires running almost perpendicular to the strips in the middle of the chamber. They are filled with a mixture of Ar- CO_2 - CF_4 gas. A charged particle entering the chamber ionizes the gas and develops an avalanche which then induces a charge on the anode wire and an image charge on a group of cathode strips. The signal on the wires is fast and is used for the Level-1 trigger [60, 69].

3.2.7 Trigger and Data Acquisition

The collision of proton bunches at the LHC with a frequency of 40 MHz creates an enormous amount of experimental data. Since the rate of collisions is too high to store each event on tape, the CMS trigger aims to select only interesting events and reduces the event rate to a manageable amount. The entire CMS trigger system consists of the Level-1 (L1) trigger

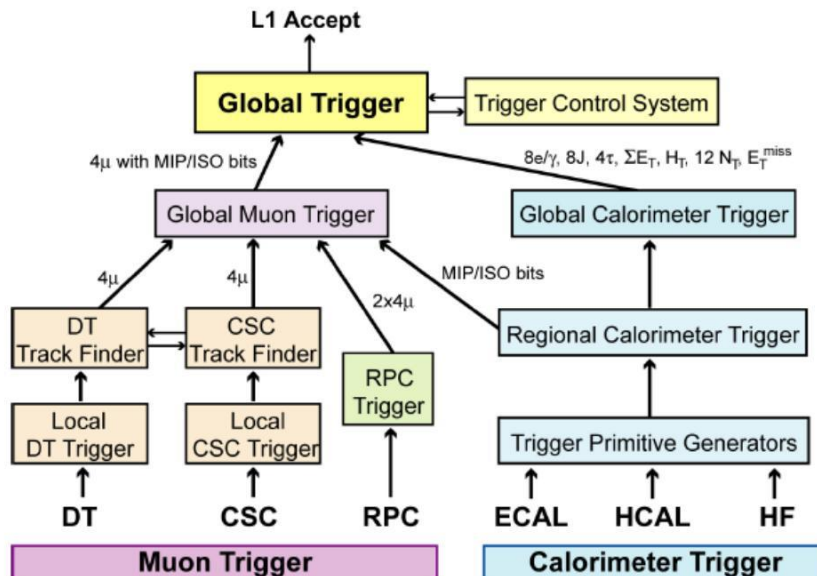


Figure 3.8: Design of the CMS L1-Trigger [2].

based on custom electronics and the High Level Trigger (HLT), a software trigger relying upon commercial processors.

For a trigger decision, the L1 trigger uses coarsely segmented data from calorimeter and muon detectors, while holding all the high-resolution data in pipeline memories in the front-end electronics. If an event is accepted by the L1 trigger decision, the high-resolution data is further analyzed by the HLT. Fig. 3.8 shows a sketch of the L1 trigger design. The global muon trigger combines and evaluates the information of the three muon systems components, where track segments identified by DTs and CSCs are used for a rough track reconstruction in the regional muon trigger, while in parallel tracks are reconstructed by using only information of RPCs. The global calorimeter trigger builds electron, photon, jets, sum of ET and MET candidates using the information of the regional calorimeter trigger. Finally the global trigger uses the information of both global muon and global calorimeter trigger to decide whether a event is dropped or accepted to be further processed by the HLT. The HLT software system processes the event on a filter farm, reducing the event rate further to 150 Hz at high luminosity running. Assuming an event size of 1.5 MB, a data stream of 225 MB/s has to be stored for latter processing. Since the HLT is a software based trigger, the algorithms used for HLT selection are flexible and adaptable [2, 70].

3.2.8 CMS Computing Model

In order to manage the enormous amount of data produced at the experiments, the LHC Computing Grid Project (LCG) has been developed, see e.g. [71, 72]. The CMS experiment

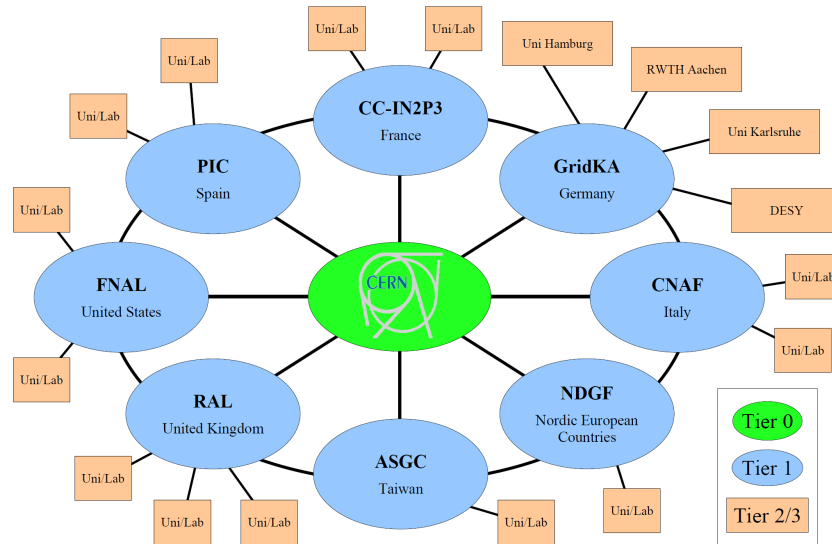


Figure 3.9: Illustration of the Tier structure of the LHC Computing Grid [71].

uses decentralized mass storage and computing resources. At the Tier 0 center at CERN the raw data passing the HLT trigger and emerging from the data acquisition system is accepted and a first reconstruction of the physics objects takes place. The raw and reconstructed data is stored in the mass storage system of the Tier 0 and copied to the associated Tier 1 centres for further processing, where the size of the data is compressed (AOD format) and dedicated filters are applied (skins). The skimmed datasets are copied to the Tier 2 centres, which offer capacity for analysis, calibration activities and Monte Carlo simulation. The last category, the Tier 3 centres are designed for interactive analysis of local groups. Fig. 3.9 illustrates the Tier structure schematically.

Chapter 4

Event Reconstruction and Software Tools

4.1 CMS Software Framework

The CMS software framework, denoted as CMSSW, has been designed to meet the requirements of a clear data model, modular testing procedures, tracking the provenance of data and a simple data structure. During processing the data is accessed only through the *Event*, a C++ object container for all raw and reconstructed data related to a particular collision. The objects in the *Event* can be stored in ROOT files, thus offering a simple structure of the data, which is directly browseable in ROOT [73]. The component structure of the framework allows the testing of individual modules in isolation. The provenance holds information about the configuration i.e. how the data has been produced.

The component architecture of the CMSSW framework uses five different types of dynamically loadable processing components

- *Source* provides the *Event* to be processed
- *Producer* add new data to the *Event*
- *Filter* decides if an *Event* is further produced
- *Analyzer* studies the properties of an *Event* without adding new data
- *OutputModule* stores the data from the *Event*

The processing model is illustrated in Fig. 4.1. First the *Source* creates the *Event*, then the different modules (*Producers*, *Filters*, *Analyzers*) process the *Event* and finally the *Event* is stored by the *OutputModule*.

The configuration is done via the configuration files. The several modules are configured using the *ParameterSet*, which holds the configuration information of the components. The values are retrieved using a string key and are passed to the modules during construction.

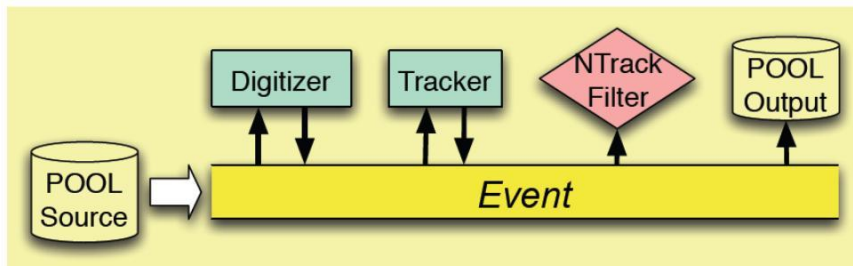


Figure 4.1: The CMS software *Event* model [74]. First a source creates the *Event*, which is passed to execution paths. The *Producers* add data to the *Event* and once all paths have been executed, the *OutputModule* stores the output to external media.

After the configuration is complete, all components will have been loaded into the application [72, 74].

In the following, the different steps from Monte Carlo event generators to reconstructed, useable physics objects are presented. First, the MC event generator calculates the proton-proton collisions, resulting in a list of particles produced in the collision. In the CMS software framework, the MC generator acts as a *Source* of the *Event*. The *Event* is further passed to the full detector simulation (FullSim), which simulates the interaction of generated particles with the detector materials, the response of the detector and the output signal of the various detector components based on GEANT [75]. The simulation step can be also performed by fast simulation (FastSim) of the detector, using only a parametrization of the detector response. Fast simulation, validated against the full simulation, is applied when only a limited computing power is available. Thereafter the reconstruction of physics objects attempts to reconstruct the initial particles from output signals of the detector components. Within the presented analysis only simulated data has been used, due to the absence of real collision data. The simulated data has been analyzed using a private *Analyzer*, which has been implemented in CMSSW. During operation of the LHC and the CMS experiment, the reconstruction of physics objects will be applied to the detector output of real collision data, thus the generation and simulation step will be omitted.

4.2 Event Generation

The complexity of Monte Carlo (MC) modeling of physics processes in proton-proton collision is shown pictorially in Fig. 4.2, including effects of QCD radiation in the initial and final state, secondary interactions, hadronisation of partons, decay of hadrons and QED final state radiation. Modern event generators typically factorize the entire process in steps according to the different kinematic regimes. The central part of the simulation of an event, namely the calculation of the hard process, shown as the dark red blob in Fig. 4.2, is provided by matrix element generators. The QCD evolution of the generated colored final

state partons is described by parton shower calculations, transforming the QCD partons with different available hadronisation models to colorless hadrons. Finally, the hadrons are decayed into particles that can be observed in the detector. The interactions of the remnants of the incoming hadrons denoted as the underlying event is beyond QCD factorization theorems and cannot be derived from first-principles theory.

Matrix element calculations and parton showers evaluation are complementary approaches and both are necessary for high precision studies of multi-jet processes, but the combination of the two approaches can result in double counting. Therefore the matching of jets from matrix element calculation with jets from parton shower evolution is mandatory. Basically the matrix element description is used for well separated jets and the parton showers for collinear jets. Two major matching schemes are currently used, the MLM [76] and the CKKM [77] method.

The study presented in this thesis uses the following MC event generator tools:

- PYTHIA [78] is a highly successful, well established standalone generator, offering leading order (LO) $2 \rightarrow 2$ matrix-element calculations and a parton shower evolution. Radiative effects and higher order corrections are described by the parton shower. The hadronisation of the generated parton final state is calculated using the Lund string fragmentation model.
- MadEvent [79] is a multi-purpose, tree-level event generator powered by the matrix element generator MadGraph, which handles leading order processes. In order to perform the parton shower, MadGraph is interfaced to PYTHIA within the CMSSW framework using the MLM matching scheme.
- ALPGEN [76] is a matrix-element generator, which is interfaced to PYTHIA within the CMSSW framework for parton shower evolution of the generated parton final states. Double counting with parton shower emissions is avoided by using the MLM matching scheme.
- SHERPA [80] is an independent multi-purpose event generation framework, based on the leading order matrix element generator AMEGIC [81]. APACIC [82] contains classes for the simulation of both the initial and the final state parton shower, which is similar to the PYTHIA approach. All features for a consistent merging with matrix elements are included, using the CKKM matching approach. The SherpaInterface [83] has been developed in order to implement the SHERPA event generator in the CMSSW framework.
- SOFTSUSY [84] is a program which accurately calculates the spectrum of super-particles in the MSSM, with a full flavor mixing structure. The program solves the renormalisation group equations with theoretical constraints on soft supersymmetry breaking terms provided by the user.
- SUSYHIT [85] is a program package for the computation of supersymmetric particle decays within the framework of the MSSM. The code is based on two existing

programs HDECAY and SDECAY for the calculation of the decay widths and branching ratios of the MSSM Higgs bosons and the SUSY particles, respectively. In the presented analysis, the SUSY particle spectrum is calculated with SOFTSUSY and passed to SUSYHIT .

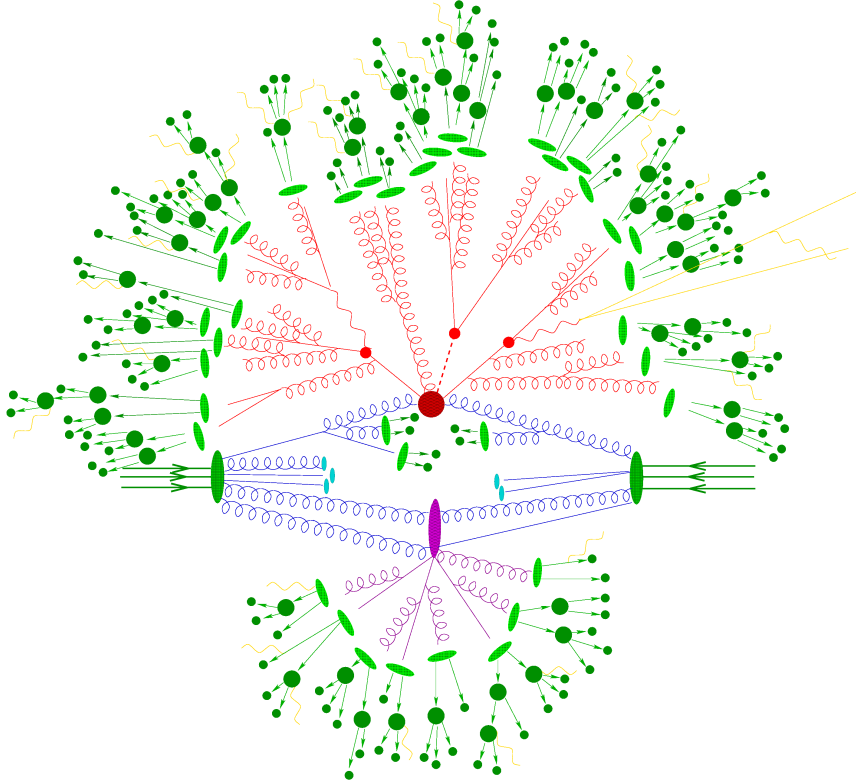


Figure 4.2: Sketch of an $t\bar{t}h$ event subdivided in several parts as seen from the perspective of typical MC event generators [86]. The top quark pair and the Higgs boson (small red blobs) are generated by gluon fusion (blue curly lines) in the hard interaction (big red blob) of a proton proton collision. The purple blob denotes secondary interactions of the partons which are not participating in the hard interaction. The top quark pairs emit hard QCD radiation (red curly lines) before the final state partons hadronize (light green blob) and hadron decay (dark green blobs). The QED radiation is shown in yellow.

4.3 Reconstruction of Physics Objects

4.3.1 Muons

The reconstruction of muons is performed in three sequent steps, namely local (muon chamber), standalone (muon system) and global (inner tracking and muon system) reconstruction.

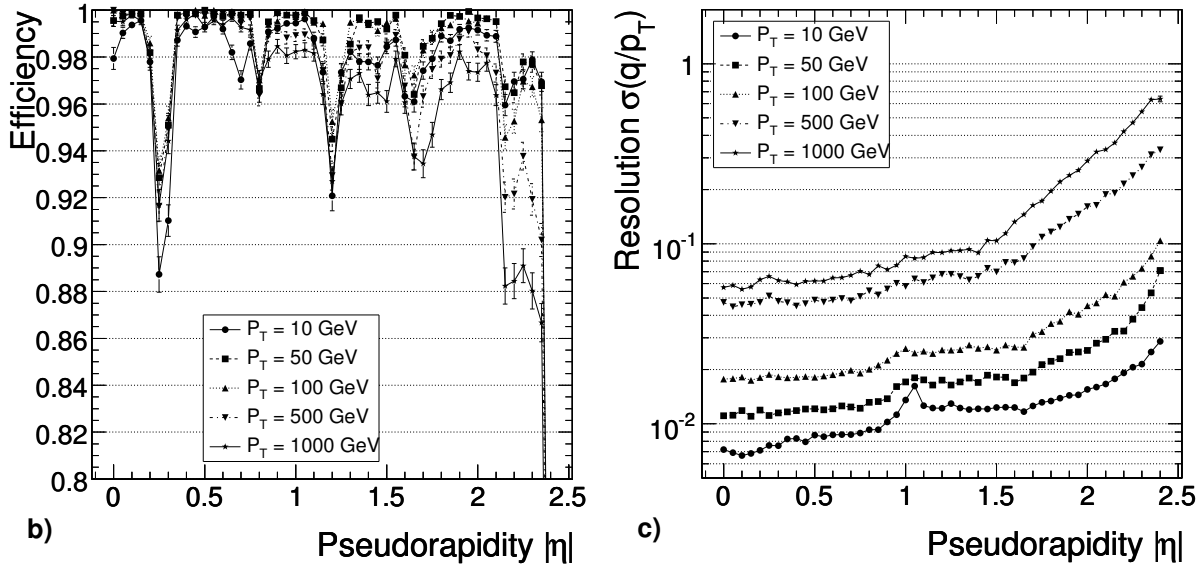


Figure 4.3: Global muon reconstruction efficiency (L) and resolution (R) as a function of the pseudorapidity [60].

The local reconstruction uses the position of hits in the muon chambers and forms segments in each chamber which are further used to generate state vectors (track segments), consisting of position, direction and an rough estimate of the muon transverse momentum. Both tracking detectors (DT and CSC) and RPCs are used, where the RPCs have a worse spatial resolution, but complement the DTs and CSCs especially in the regions with problematic geometrical coverage, mostly in the barrel-endcap overlap region.

The state vectors obtained with the local reconstruction are used as the input for the standalone reconstruction. The muon trajectories are build starting from the innermost chambers, subsequently including to the outer chambers, using the Kalman filter technique [87]. In order to reject bad hits, mostly from showering, delta rays and pair production, a suitable χ^2 cut is applied. The search for suitable hits is continued to the next station, if no matching segments are found in order to prevent detector inefficiencies, geometrical cracks or hard showering. Once the outermost chambers are reached, a backward Kalman filter is applied, working from outside in, and the track parameters are defined at the innermost muon station. Finally, the track is extrapolated to the nominal interaction point, which is defined by the beam-spot size ($\sigma_{xy} = 15 \mu\text{m}$, $\sigma_z = 5.3 \mu\text{m}$) and a vertex constrained fit to the track parameters is performed.

The global muon reconstruction extends the muon trajectories including the information of the inner tracking system. Using the standalone reconstructed muon as input, the muon trajectory is extrapolated from the innermost muon station to the outermost region of the inner tracking system. The region of interest in the tracker are determined by the extrapolation of the muon track taking into account muon energy loss in the material, multiple

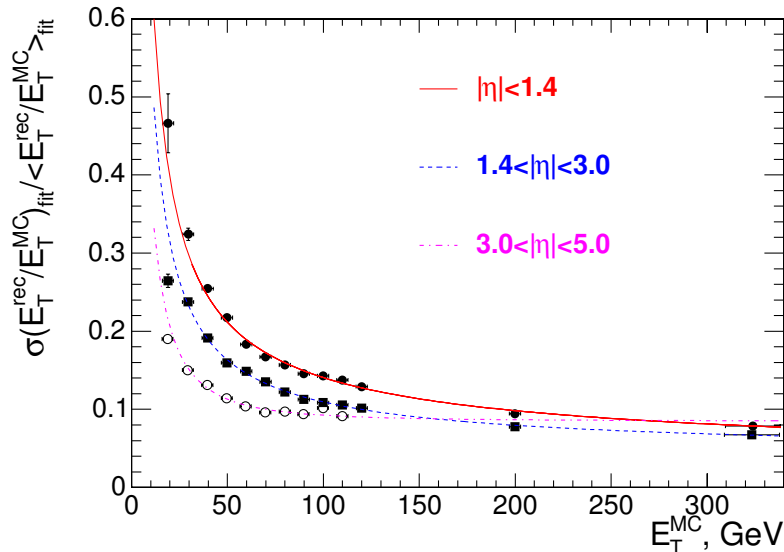


Figure 4.4: Jet transverse energy resolution as a function of the generated jet transverse energy for barrel jets ($|\eta| < 1.4$), endcap jets ($1.4 < |\eta| < 3.0$) and very forward jets ($3.0 < |\eta| < 5.0$), reconstructed with the iterative cone algorithm ($R = 0.5$) [60].

scattering effects and the uncertainties of the extrapolation. Inside the regions of interest in the inner tracking system, regional seeds are build using two hits from different layers. Then the track reconstruction algorithm runs, transforming each seed into a set of trajectories working from inside-out. Based on the hit multiplicity and χ^2 tests, the trajectory cleaner resolves ambiguities between multiple trajectories arising from the same seed. In the last step, the reconstructed tracks are fitted using the hits in the muon chambers from the original standalone reconstruction together. The final muon candidates are selected on the basis on a χ^2 cut.

The muon reconstruction efficiency and the momentum resolution for the global reconstructed muons is shown in Fig. 4.3. The reconstruction efficiency is typically 95-99%, except for pseudorapidity regions between 2 DT wheels ($|\eta| = 0.25$ and $|\eta| = 0.8$) and in the transition region between the DT and CSC systems ($|\eta| = 1.2$). For low-momentum muons, the muon resolution around $\sim 2\%$ is dominantly obtained by the resolution in the silicon tracker [60].

4.3.2 Jets

The jet reconstruction attempts to identify and to measure the properties of initial colored partons generated in the hard interaction. Since the colored partons hadronize and produce a bunch of color-neutral hadrons, which can further decay, the jet clustering algorithms attempt to group all particles originating from the initial parton in a single object, the jet.

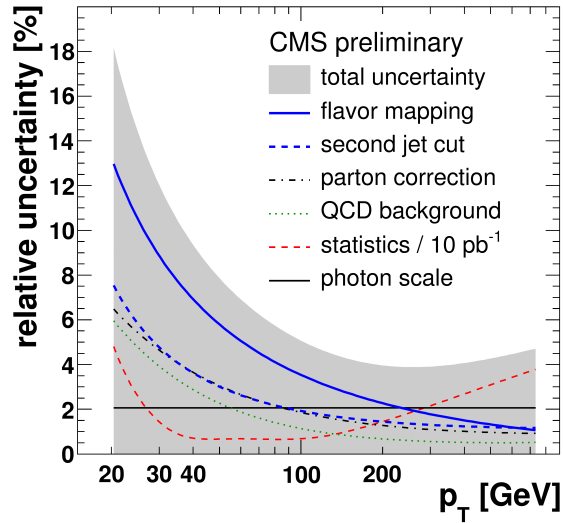


Figure 4.5: Relative jet energy scale uncertainty obtained with the γ +jet calibration for $\mathcal{L}_{acc} = 10 \text{ pb}^{-1}$ of accumulated data [88].

This is done by their energy deposition in the electromagnetic and hadronic calorimeter. Since the ECAL granularity is much finer than HCAL, calorimeter towers are formed by addition of signals in bins corresponding to individual HCAL cells. After considering energy thresholds for noise suppression, the energy deposits in the towers are used as input to several jet clustering algorithms.

Among several available jet algorithm within the CMSSW framework, the presented analysis has used the iterative cone jet algorithm. The cone size and the seed threshold are parameters of the algorithm. The iterative cone algorithm uses input objects ordered by ET above a specified seed threshold. The direction and energy of the so-called proto-jet is derived by considering all towers in a cone of size R . Then the direction is used as a seed for calculating the next proto-jet. This procedure continues until a defined criteria, then all input objects are removed from the input list and the procedure starts again until all input objects above the seed threshold are removed from the input list.

Since the energy of reconstructed jets differs from the energy of the initial partons due to detector and reconstruction effects, the jets are corrected according to a multi-step procedure [89]. The expected jet energy resolution determined with a sample of simulated QCD dijet events is shown in Fig. 4.4, where the transverse energy of the reconstructed jet was compared with the corresponding particle jet on generator level. The resolution for jets in the pseudorapidity range $|\eta| < 1.4$ is parameterized as:

$$\sigma\left(\frac{ET_{rec}/ET_{MC}}{\langle ET_{rec}/ET_{MC} \rangle}\right) = \frac{5.6}{ET_{MC}} \oplus \frac{1.25}{\sqrt{ET_{MC}}} \oplus 0.033 \quad , \quad (4.1)$$

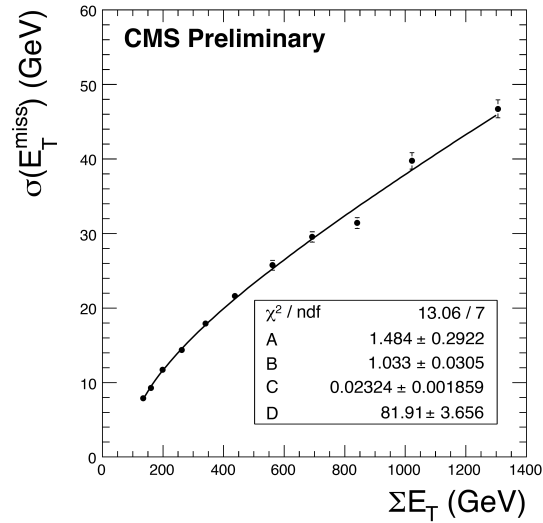


Figure 4.6: Resolution of the missing transverse energy for simulated QCD dijet samples without pile-up, the black line represents the fit of the resolution, parameterized according to Eq. 4.3 [91].

where the first term represents fixed energy fluctuations in the cone from electronics noise, pile-up and underlying event energy, the second term represents the stochastic response of the calorimeter measurement and the last term comes from residual non-linearities in the detector response [60].

The absolute jet energy scale can be calibrated with collision data using balanced γ +jet [88] and Z +jet [90] events. In the γ +jet study, the jet calibration is obtained from the extraction of the response in photon+jet events, which is defined as the ratio of the PT of the jet and the PT of the recoiling photon measured in the electromagnetic calorimeter. Figure 4.5 shows the relative jet energy scale uncertainty obtained with this approach for $\mathcal{L}_{acc} = 10 \text{ pb}^{-1}$ of accumulated data. The jet energy scale uncertainty is $\sim 10\%$ for low PT jets and is reduced for jets with higher transverse momentum. For larger accumulated luminosity $\mathcal{L}_{acc} \sim 1 \text{ fb}^{-1}$, the uncertainty is expected to be further reduced.

Due to the large systematic uncertainties of the jet energy scale in the first year of LHC running, the study presented in this thesis attempts to search for SUSY without using jets for event selection.

4.3.3 Missing Transverse Energy

The CMS detector has nearly 4π -solid angle coverage, but is not completely hermetic, since openings for the proton beams are mandatory. The calorimeter system covers ranges

$|\eta| < 5$. Therefore the total energy balance of an event cannot be used, since low PT particles moving in very forward direction escape detection. However since those particles carry only small transverse momentum, the detector allows for rather precise tests of the 2D-momentum conservation in the plane perpendicular to the direction of the beams.

As a result, any significant imbalance in transverse momentum measured in the calorimeter is indicative of a production of a weakly interacting particle in the collision, which by itself indicates a process of interest. Among the standard model particles, such an imbalance would indicate the presence of either a muon or a neutrino. The momentum of the muon can be precisely measured combining the central tracker and the muon system, and the calorimeter-based missing transverse momentum is corrected for its presence. The only SM particle that would truly escape the detection is the neutrino. In SUSY R parity conserving models the lightest supersymmetric particle is stable, massive, only weakly interacting and is always produced in cascade decays of heavier SUSY particles. The presence of LSPs in SUSY events contributes to the transverse missing energy, which is accordingly an important observable of SUSY events.

The missing transverse energy is determined from the transverse vector sum over energy deposits in projective calorimeter towers:

$$\mathbf{MET} = - \sum_n (E_n \sin \theta_n \cos \phi_n \cdot \hat{i} + E_n \sin \theta_n \sin \phi_n \cdot \hat{j}) = MET_x \hat{i} + MET_y \hat{j} \quad , \quad (4.2)$$

where the index n denotes all calorimeter input objects and \hat{i}, \hat{j} are the unit vectors in the direction of the x and y axis.

The global nature of MET also means that disentangling and understanding the different factors affecting the performance can be very challenging. Figure 4.6 illustrates the resolution of MET vs. the scalar sum of ET measured in the calorimeter (sumET) for QCD dijet sample. The resolution of MET can be parameterized as:

$$\sigma(\text{MET}) = A \oplus B \cdot \sqrt{\sum ET - D} \oplus C \cdot (\sum ET - D) \quad , \quad (4.3)$$

where the noise term A represents effects due to electronic noise, pile-up and underlying event, the stochastic term B represents the statistical sampling nature of the energy deposits in individual calorimeter towers, the constant term C represents residual systematic effects due to non-linearities, cracks, and dead material and the offset term D represents the effects of noise and pile-up.

The missing transverse energy is extremely sensitive to various detector malfunctions and particles hitting poorly instrumented regions of the detector. Any dead or malfunctioning element in the detector may result in an artificial imbalance, thus mimicking the signal for SUSY events. Consequently, great care is required to understand the distribution in missing transverse momentum as measured by the detector and to ensure that it is a trustworthy variable for searches. Hence, the MET variable is not an easy object to understand, so a long and dedicated study will be necessary to turn it into a useful physics analysis variable [60, 91].

The search for SUSY presented in this thesis has been designed avoiding the use of missing

transverse energy for rejection of the Standard Model background, in order to prevent the impact of the huge systematic uncertainties, which are associated with this variable.

4.4 Software Tools

- ROOT [73] is an object-oriented framework designed for the challenges of data analysis in high-energy physics. Among other various features, it provides facilities for visualization physics results.
- GARCON [92] automatically performs rectangular cuts optimization, evaluation of the most discriminating parameters and verification for stability in a multi-dimensional cuts phase space. The program has been successfully used by a number of different analyses presented in the CMS collaboration e.g. [15, 93]. The optimization of selection cuts for high energy physics analysis would require a scan over multi-dimensional selection cut space demanding an enormous amount of CPU time. The GARCON package provides access to Genetic Algorithm (GA) (see e.g. [94, 95]) solving the optimization with a comparable little amount of CPU time effectively trying $\sim 10^{50}$ selection cut parameters permutations for millions of input events.
- RooStatsCMS [96] software framework was developed at the University of Karlsruhe and allows to combine different analyses in order to increase the statistical significance. It takes care of correlations between these analyses and allows various treatment of systematic uncertainties.

For the analysis presented in this thesis the profile likelihood method has been used to calculate the significance of a signal observation. Within the RooStatsCMS framework a profile likelihood scan is performed: For each value of signal s , the likelihood $L(s, b, \sigma)$ is maximized with respect to the nuisance parameters (b, σ) , where b is the background expectation and σ denotes the systematic uncertainty, which is assumed as Gaussian distributed. For the hypothesis-test the likelihood-ratio

$$Q = \frac{L(s = 0, \hat{b}, \hat{\sigma})}{L(\hat{s}, \hat{b}, \hat{\sigma})} \quad , \quad (4.4)$$

where \hat{x} indicates that the parameter x has been estimated to maximize the likelihood, is used as a test statistics to distinguish between the null-hypothesis ($s = 0$) and the best alternative ($s = \hat{s}$). The significance is calculated as $\sqrt{-2\ln Q}$ (for details see [97]).

Chapter 5

Trimuon SUSY Search

The challenge of searching for SUSY is to distinguish the rare events with SUSY particles from the huge amount of events with only SM particles produced. As discussed in the review of searches for direct production of SUSY particles at the collider experiments LEP and Tevatron (Section 2.3.4), there are always several searches in different production channels. Each of these approaches has its benefits, and its downsides.

As mentioned in the introduction of this thesis the presented analysis has been designed for the first year of LHC running with 5 TeV per beam starting in 2010. At the LHC, the largest SUSY cross section is expected in pure hadronic final states with a large jet multiplicity accompanied by a large missing transverse energy caused by the lightest SUSY particles, which are stable and only weakly interacting. For this reason, the suppression of SM backgrounds in SUSY searches usually requires selection on missing transverse energy and jets. However, these variables are prone to large theoretical and instrumental uncertainties, especially at the beginning of LHC operation. The presented analysis has been developed driven by the idea of searching for supersymmetry without suffering from the impact of the large systematic uncertainties associated with hadronic observables. The most suitable candidate being subject to these conditions is the clean SUSY trimuon signature, even though it carries only a small fraction of the SUSY cross section.

5.1 Trimuon SUSY Signal

In this section the production and properties of the trimuon signature at the LHC is presented. The trimuon SUSY search uses prompt isolated muons, which are mainly produced in decays of next-to-lightest neutralinos (χ_2^0) and lightest charginos (χ_1^\pm). The gauginos can be produced either directly or in decays of squarks (\tilde{q}) and gluinos (\tilde{g}). Trimuon final states originates from SUSY events populated with pairs of a neutralino χ_2^0 and a chargino χ_1^\pm subsequently decaying to muons.

5.1.1 SUSY Particle Production

In proton-proton collisions at the LHC, SUSY particles are produced in various different processes. In this analysis the R parity conserving mSUGRA model is considered, accordingly SUSY particles are produced in pairs. In the following the production of gluinos and squarks and the direct production of gauginos at the LHC is reviewed.

Gluinos and Squarks

Squarks and gluinos are mainly produced in strong interactions of quarks and gluons. The production of squark-antisquark final states requires quark-antiquark or gluon-gluon initial states, whereas squark-pairs can be only produced from quark pair reactions. Gluino pairs are produced from quark-antiquark and gluon-gluon initial states. Squark-gluino final states can only be produced in quark-gluon collisions [98]. Fig. 5.1 shows typical leading order processes.

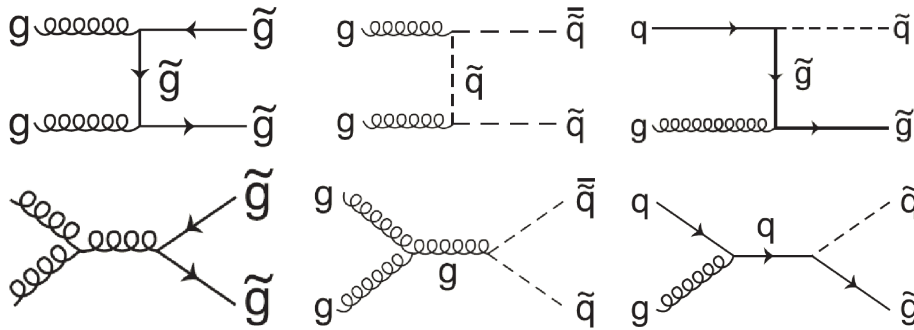


Figure 5.1: Typical diagrams for (L) gluino pair, (M) squark pair, (R) gluino-squark production [4].

Neutralinos and Charginos

The direct production of neutralinos and charginos is an electroweak process. Direct neutralino-chargino pairs are produced in s -channel and t -channel reactions of quarks and antiquarks. The vector boson in the s -channel couples to the gaugino and higgsino components of the charginos and neutralinos, whereas the squarks in the t -channel exchange, which are partners of the light quarks, couple mainly to the gaugino components. The relative contribution of s -channel and t -channel amplitudes depends on squark masses and the chargino and neutralino field content e.g. the t -channel diagram is suppressed for large squark masses [99]. Typical diagrams for the direct pair production of neutralinos and charginos are presented in Fig. 5.2.

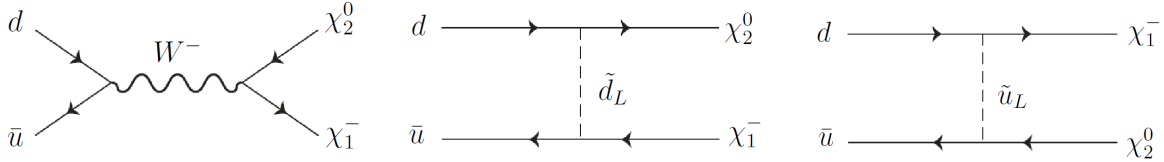


Figure 5.2: Typical diagrams for the direct neutralino-chargino pair production [4].

Cross section

Fig. 5.3(a) shows the total SUSY cross section in the m_0 - $m_{1/2}$ plane for $\tan\beta = 10$, $A_0 = 0$, $\mu > 0$ and $\sqrt{s} = 10$ TeV collision energy. The cross section decreases with increasing mass of SUSY particles, thus depending strongly on the value of $m_{1/2}$. The largest cross section at $m_0, m_{1/2} < 200$ GeV corresponding to low mass SUSY offers the opportunity to inspect this region of parameter space during the first year of LHC running at $\sqrt{s} = 10$ TeV.

If squarks and gluinos are kinematically accessible, the largest SUSY cross section is obtained for gluino and squarks production (Fig. 5.3(b)), followed by the electroweak production of neutralinos and charginos. Here, the direct production of the next-to-lightest neutralino and the lightest chargino (Fig. 5.3(c)) and the pair production of the lightest charginos are the dominant processes. The squarks and gluinos are typically heavier than the uncolored SUSY particles. The cross section of the direct neutralino-chargino production is comparably small in a wide region of the mSUGRA plane and becomes significant only at larger values of m_0 , when squarks become too heavy. The contribution of direct pair production of heavier neutralino-chargino pairs (Fig. 5.3(d)) increases for larger values of m_0 , since here the masses of heavier and lighter gauginos are of the same order. The direct slepton pair production carries a small fraction only at low m_0 , when the slepton mass is comparably small and is negligible in a wide region of the mSUGRA plane.

5.1.2 Prompt Muons in SUSY Particle Decays

The presented analysis attempts to identify SUSY using prompt isolated muons, which originate mainly from decays of neutralinos (χ_2^0) and charginos (χ_1^\pm). Below the production of gauginos in squark and gluino cascade decays and the properties of the gaugino decay to muons is reviewed.

Gauginos from Gluino and Squark Decays

The gluino and squark decay modes depend strongly on the SUSY mass spectrum. If squarks are lighter than gluinos $m_{\tilde{q}} < m_{\tilde{g}}$, gluinos tend to decay in two-body decay to

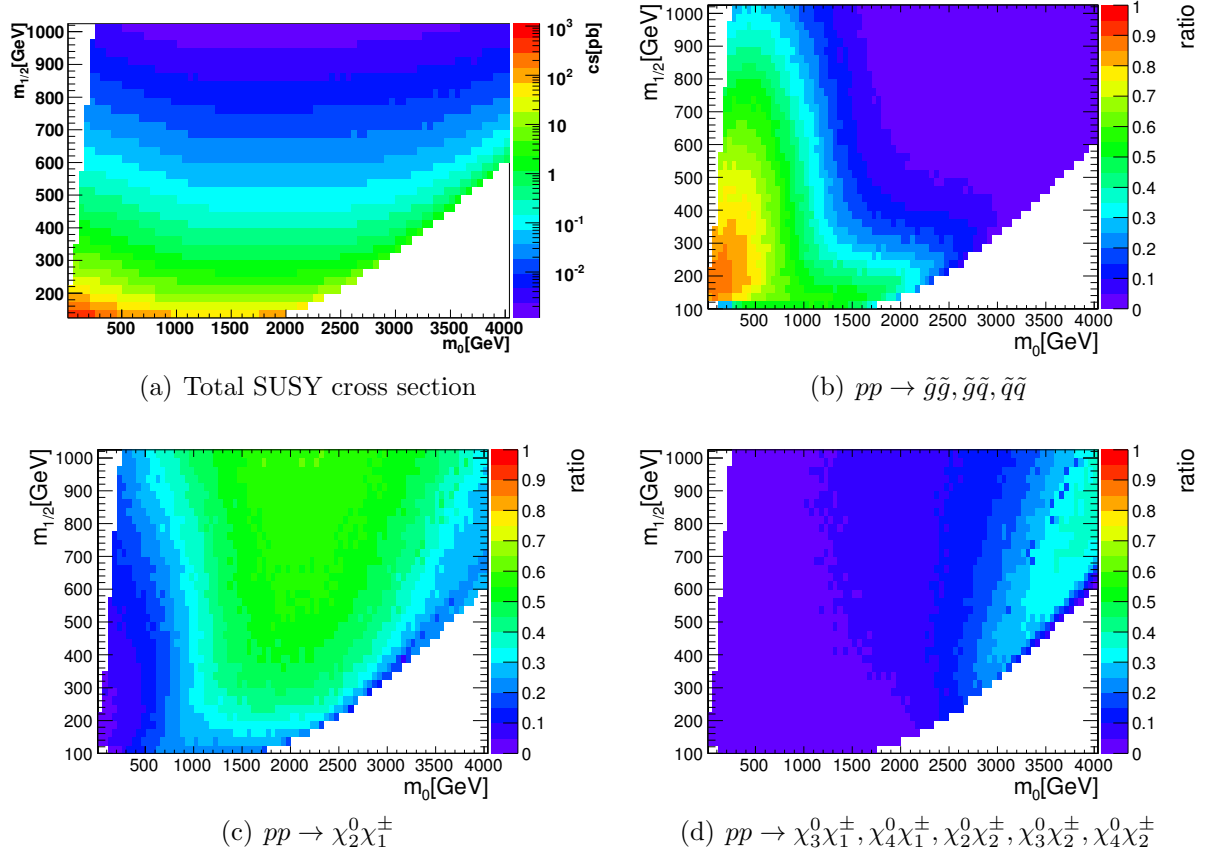


Figure 5.3: Total SUSY cross section (a) at the LHC ($\sqrt{s} = 10$ TeV) for $\tan\beta = 10$, $A_0 = 0$, $\mu > 0$ and the corresponding cross section fraction of gluino and squark production (b), direct production of the lightest chargino and next-to-lightest neutralino (c) and heavier neutralino-chargino pairs (d).

quark-squark pairs:

$$\tilde{g} \rightarrow \tilde{q}\tilde{q}, \tilde{q}\tilde{q}^* \quad , \quad (5.1)$$

and squarks decay dominantly into quarks and gauginos:

$$\tilde{q}_{(L,R)} \rightarrow \chi_i^0 q \quad (5.2)$$

$$\tilde{q}_{i(L)} \rightarrow \chi_i^\pm q_j \quad . \quad (5.3)$$

For left-handed squarks, the decay to the lightest chargino and next-to-lightest neutralino dominates at small squark masses. At larger squark masses, the branching fraction to heavier gauginos increases. For right-handed squarks, the decay to the lightest neutralino dominates. At larger squark masses, the branching fraction to the next-to-lightest neutralino increases [100]. The branching fractions of left-handed and right-handed squarks

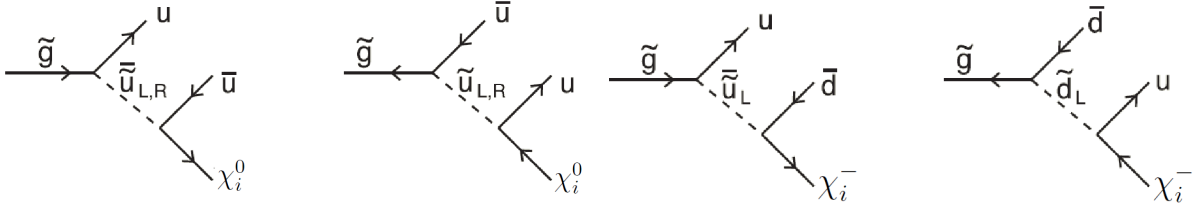


Figure 5.4: Typical three-body decays of gluinos to neutralinos and charginos [4].

are shown as a function of the squark mass in the appendix in Fig. B.1 and Fig. B.2, respectively.

If gluinos are lighter than squarks $m_{\tilde{q}} > m_{\tilde{g}}$, squarks decay dominantly into quarks and gluinos:

$$\tilde{q} \rightarrow q\tilde{g} \quad , \quad (5.4)$$

and gluinos decay mainly into quark-antiquark pairs and additional gauginos:

$$\tilde{g} \rightarrow q\bar{q}\chi_i^0 \quad (5.5)$$

$$\tilde{g} \rightarrow q_i\bar{q}_j\chi_i^\pm \quad . \quad (5.6)$$

The decay to the lightest chargino is dominant, followed by the decay to the next-to-lightest neutralino. For larger gluino masses the contribution of decays into heavy gauginos increases (see Figure B.3 in the appendix) [100]. Typical three-body diagrams are shown in Fig. 5.4.

Muons from Decays of Gauginos

The decay modes of the neutralino χ_2^0 and the chargino χ_1^\pm depend strongly on the considered mSUGRA parameter region. Two-body decays to a lepton-slepton pair dominate if kinematically allowed:

$$\chi_2^0 \rightarrow \mu\tilde{\mu} \quad , \quad (5.7)$$

where the superpartner of the muon decays preferably to the lightest neutralino and a muon ($\tilde{\mu} \rightarrow \mu\chi_1^0$). If this decay is kinematically forbidden and the mass difference of the neutralinos is larger than the mass of the Higgs boson h^0 i.e. $\Delta m(\chi_2^0, \chi_1^0) > m(h^0)$, the decay to the Higgs boson dominates. Once both previously mentioned decays are kinematically not allowed, the neutralino decays via an on-shell Z boson:

$$\chi_2^0 \rightarrow h^0\chi_1^0, Z\chi_1^0 \quad . \quad (5.8)$$

Once all previously listed decays are kinematically forbidden, direct three-body decays mediated dominantly by an off-shell Z boson or a slepton take place:

$$\chi_2^0 \rightarrow \mu^+\mu^-\chi_1^0 \quad . \quad (5.9)$$

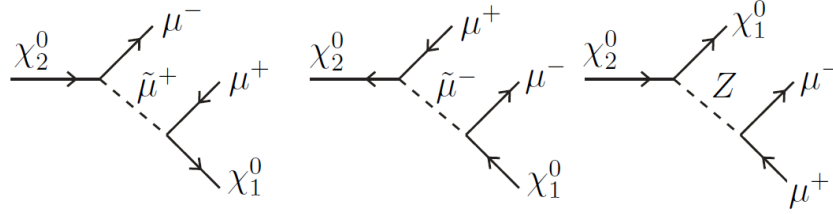


Figure 5.5: Typical three-body decays of neutralinos to muon final states [4].

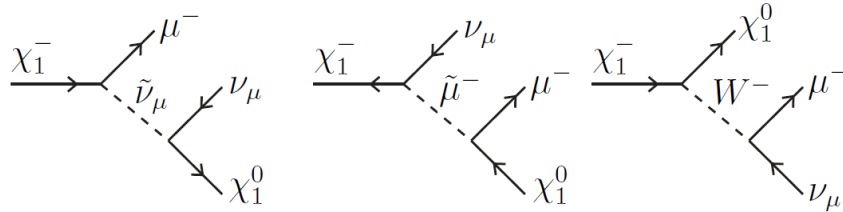


Figure 5.6: Typical three-body decays of charginos to muon final states [4].

Typical diagrams for three-body decays of neutralinos to muon final states are shown in Fig. 5.5.

The decays of charginos behave similar to neutralino decays. If all other decay modes are energetically forbidden, chargino decays are mediated dominantly by an off-shell W boson or a slepton in three-body decays

$$\chi_1^\pm \rightarrow \nu\mu\chi_1^0 \quad . \quad (5.10)$$

Fig. 5.6 shows typical diagrams for three-body decays of charginos to muon final states. If allowed by the mass difference of the chargino χ_1^\pm and the neutralino χ_1^0 , two-body decays into the lightest neutralinos and the W boson are dominant:

$$\chi_1^\pm \rightarrow W^\pm\chi_1^0 \quad , \quad (5.11)$$

where in case of decays $W \rightarrow \mu\nu$ the final state consists of a muon, a neutrino and the lightest neutralino. Similar to neutralinos two-body decays to slepton-lepton pairs are preferred, if kinematically allowed:

$$\chi_1^\pm \rightarrow \nu\tilde{\mu} \quad . \quad (5.12)$$

Fig. 5.7 shows the corresponding regions of the various neutralino and chargino decay modes in the $m_0 - m_{1/2}$ plane for $\tan\beta = 10$, $A_0 = 0$ and $\mu > 0$. The exact boundaries of the regions depend also on the values of $\tan\beta$ and A_0 . Decays to sleptons dominate at small values of m_0 and large values of $m_{1/2}$. In the major part of the mSUGRA parameter space

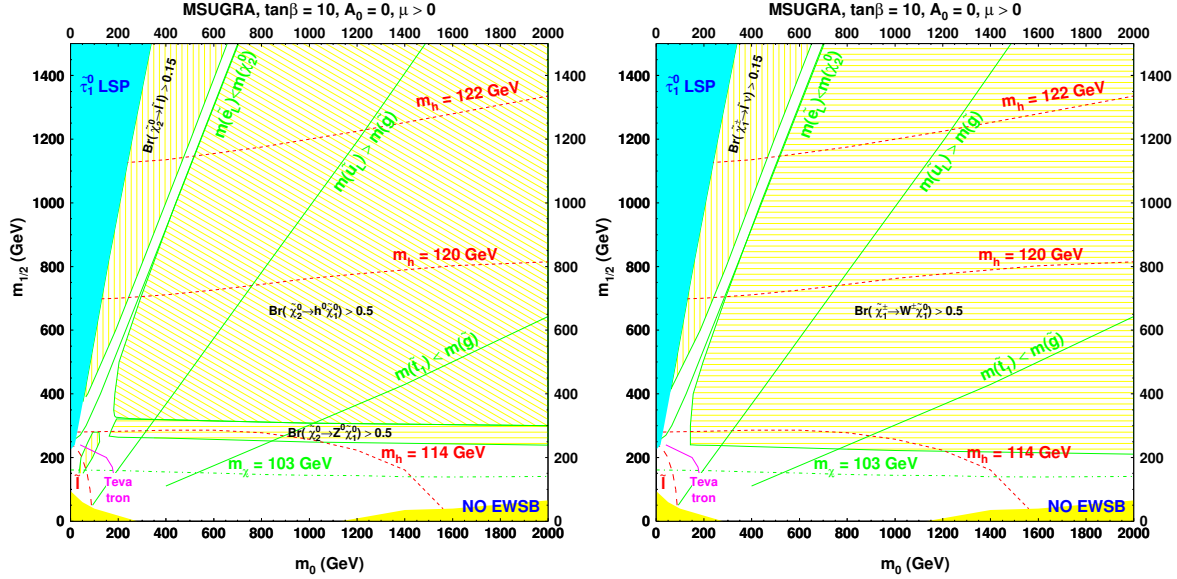


Figure 5.7: Regions corresponding to the main neutralino χ_2^0 (L) and chargino χ_1^\pm (R) decay modes to lepton final states in the m_0 - $m_{1/2}$ plane for $\tan\beta = 10$, $A_0 = 0$ and $\mu > 0$ [101].

the neutralino χ_2^0 and the chargino χ_1^\pm tend to decay into a lightest Higgs boson and a W boson, respectively. In a very narrow region at smaller values of $m_{1/2} \sim 300$ GeV, where the mass difference of the neutralino χ_2^0 and the chargino χ_1^0 is smaller than the lightest Higgs boson mass, decays of the neutralino χ_2^0 to an on-shell Z boson are preferred. Due to the small mass difference $\Delta m(\chi_2^0, \chi_1^0)$ and $\Delta m(\chi_1^\pm, \chi_1^0)$, three-body decays dominate at small values of $m_{1/2}$. Only at the very left lower corner at small values of m_0 and $m_{1/2}$, the neutralino starts to decay in two-body modes to slepton-lepton pairs again. Since this transition area happens to be in the range of the presented search, the special kinematics of muons from neutralino decays in the corresponding region of the parameter space is further discussed.

Kinematics of Muons from Neutralino Decays

In the region of the mSUGRA parameter plane with low m_0 and $m_{1/2}$, the neutralino decays in two-body modes to muons ($\chi_2^0 \rightarrow \mu \tilde{\mu}$). Since the mass of sleptons increases with m_0 , the mass difference of the neutralino χ_2^0 and the slepton decreases with increasing m_0 . Once $m_{\tilde{\mu}}$ becomes larger than $m_{\chi_2^0}$, the neutralino starts to decay in three-body modes $\chi_2^0 \rightarrow \mu \mu \chi_1^0$. But close to this transition region two-body decays still take place. Fig. 5.8 shows the PT distribution of the muon from two-body decays $\chi_2^0 \rightarrow \mu \tilde{\mu}$ for three scenarios $m_0 = 80, 90, 100$ GeV and $m_{1/2} = 200$ GeV, $\tan\beta = 10$, $A_0 = 0$, $\mu > 0$. For the latter the mass difference $\Delta m = m_{\chi_2^0} - m_{\tilde{\mu}}$ is ~ 1.9 GeV. Since the phase space for the muon produced in the neutralino χ_2^0 decay is small, the muon obtains only little momentum. Consequently the reconstruction and selection efficiency of the muon decreases.

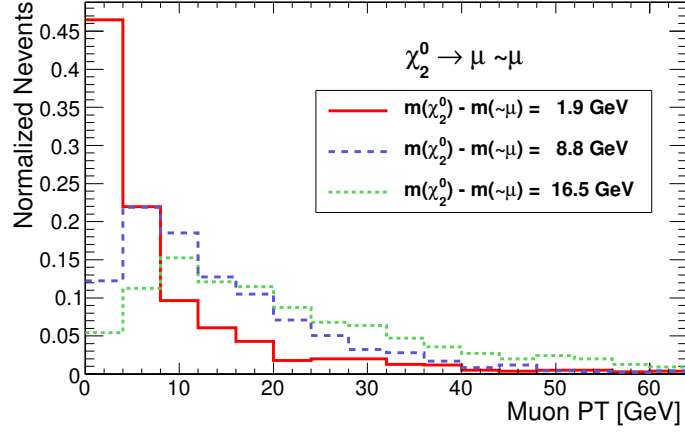


Figure 5.8: Transverse momentum distribution of muons from neutralino decays $\chi_2^0 \rightarrow \mu \tilde{\mu}$ for different scenarios with small mass difference $m_{\chi_2^0} - m_{\tilde{\mu}}$ for $m_0 = 80, 90, 100$ GeV and $m_{1/2} = 200$ GeV, $\tan\beta = 10$, $A_0 = 0$ and $\mu > 0$. The larger the value of m_0 , the smaller the mass difference and the softer the muons.

Dimuon Invariant Mass

The invariant mass distribution of opposite sign (OS) muon pairs produced by neutralino χ_2^0 decays exhibits a particular shape for two-body decays to slepton-lepton and three-body decays. This specific shape is not realized in any SM particle decay to dimuon pairs and represents a peculiarity of SUSY events. The kinematic end point depends on the event topology and is given for two-body decays by

$$M_{ll}^{max} = \sqrt{(m_{\chi_2^0}^2 - m_{\tilde{l}}^2)(m_{\tilde{l}}^2 - m_{\chi_1^0}^2)}/m_{\tilde{l}}^2 \quad (5.13)$$

and for three-body decays via off-shell Z or slepton by

$$M_{ll}^{max} = m_{\chi_2^0} - m_{\chi_1^0} \quad . \quad (5.14)$$

The peculiarity of the dimuon invariant mass distribution disappears at larger values of $m_{1/2}$, where the neutralino decays to a Higgs boson or an on-shell Z boson. Fig. 5.9 shows the dimuon invariant mass distribution for different scenarios. Since the presented analysis has used $M_{ll} < M_Z$ to select SUSY and reject SM events, it is not sensitive to regions where the neutralino decays to on-shell Z boson.

5.1.3 Trimuon Signature

Below the cross section of the SUSY trimuon signature is discussed. Fig. 5.10 shows the contribution of different muon multiplicity final states to the total SUSY cross section. The

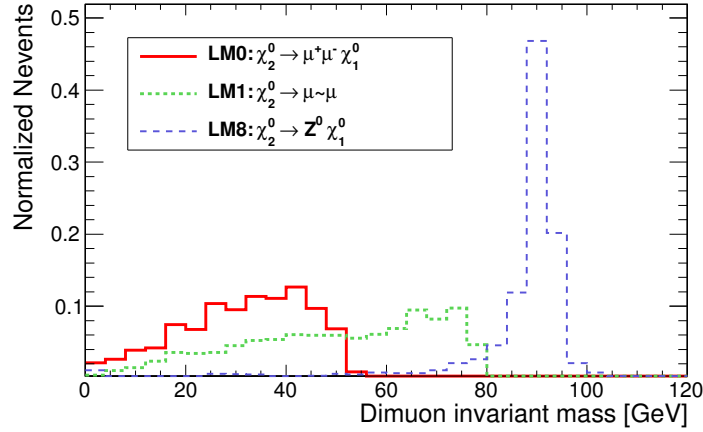


Figure 5.9: Dimuon invariant mass distribution of opposite sign muon pairs produced by χ_2^0 in three-body decays, two-body decay to sleptons and two-body decays to on-shell Z boson. The mSUGRA parameters of the corresponding LM benchmark points are shown in Tab. 5.1.

larger the number of muons in the final state, the smaller the cross section fraction. The variation in the mSUGRA parameter plane originates from the corresponding SUSY production mechanisms as well as from the decay topologies of SUSY particles. The increase of the leptonic fraction at small m_0 and large $m_{1/2}$ originates from the leptonic branching ratio of neutralinos and charginos, which increases, since here sleptons are lighter than gauginos and two-body decays via sleptons take place. In the region at $m_0 \sim 1000$ GeV and $m_{1/2} \sim 500$ GeV, the rise of the leptonic fraction corresponds mainly to the contribution of right-handed squarks decaying to gluinos, whereas at lower m_0 , squarks are lighter than gluinos and decay almost exclusively to the lightest neutralino and a quark. However in regions with larger m_0 , the squarks become too heavy and the contribution to the total SUSY cross section becomes negligible. The increase of the leptonic branching ratio at larger m_0 originates from the contribution of heavier neutralino and chargino pairs to the total SUSY cross section, since in this region the masses of lighter and heavier gauginos are similar and squarks and gluino are comparatively heavy.

The trimuon signature carries only a small part of the total SUSY cross section. Fig. 5.11 presents the contribution of different production mechanisms to the total SUSY trimuon cross section. In the region at low m_0 and $m_{1/2}$, the bulk of trimuon events originates from gluino and squark production. Here the contribution of direct neutralino-chargino pair production is small, but becomes significant at larger m_0 and small $m_{1/2}$, as well as at small m_0 and large $m_{1/2}$. In regions with large m_0 and large $m_{1/2}$, the contribution of direct pair production of heavier gaugino pairs becomes dominant.

The direct neutralino-chargino pair production corresponds to the trimuon signature with-

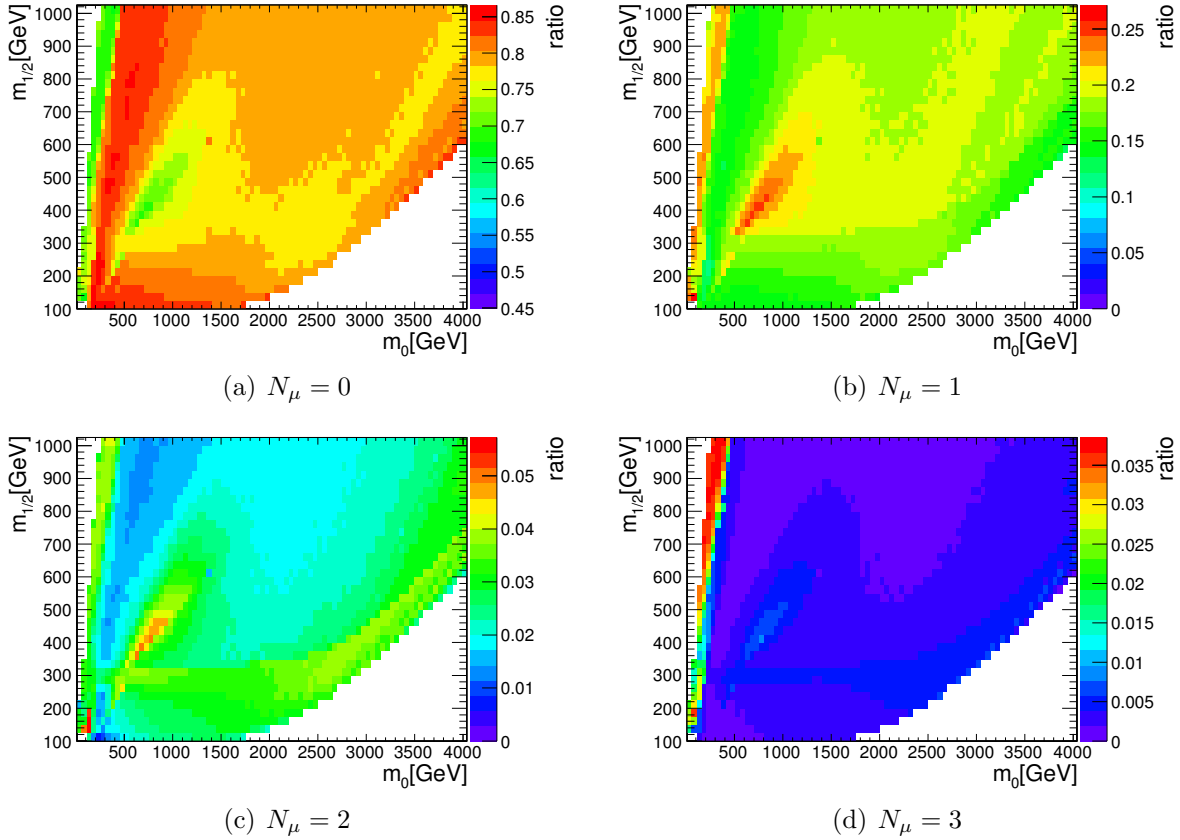


Figure 5.10: Cross section fraction for final states with different muon multiplicities with respect to the total SUSY cross section shown in Fig. 5.3(a). The larger the number of muon in the final state, the smaller the cross section fraction. The variation in different regions of parameter space originates from the SUSY production mechanisms as well as from the decay modes of SUSY particles.

out hard jets and with some missing transverse energy from the escaping lightest SUSY particles and neutrinos. Since squarks and gluinos decay to gauginos plus additional quarks, trimuon events originating from squark and gluino production are accompanied by a large number of jets, as well as by some missing energy from the lightest neutralinos and neutrinos. Fig. 5.13 shows typical diagrams of the SUSY trimuon signature produced in direct neutralino-chargino pair production and gluino-gluino production. The jet multiplicity for both trimuon signatures is presented in Fig. 5.12 for the benchmark point LM9 ($m_0 = 1450$ GeV, $m_{1/2} = 175$ GeV, $\tan\beta = 50$, $A_0 = 0$, $\mu > 0$), where the contribution of direct production is significant. The presented analysis is sensible to both production mechanisms, since no selection on the jet multiplicity has been applied.

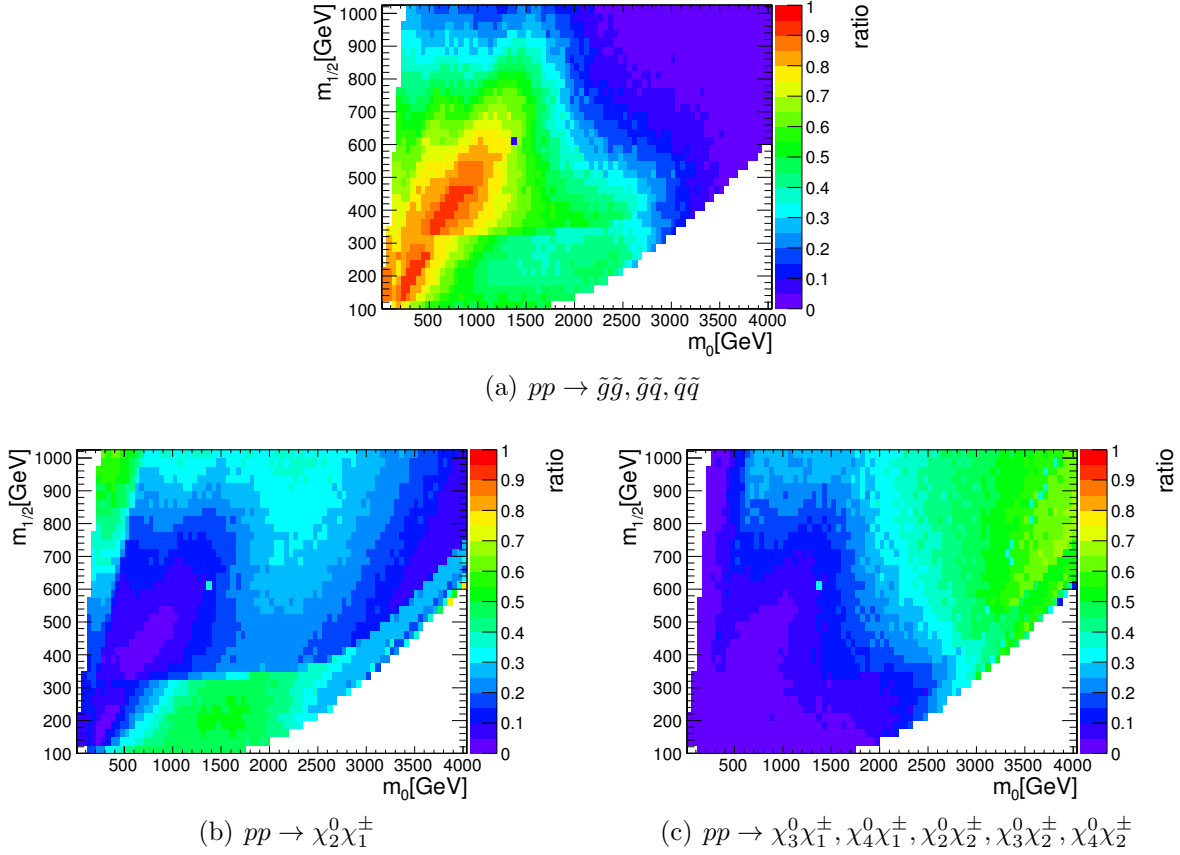


Figure 5.11: Contribution of the (a) squarks and gluino, (b) direct neutralino-chargino and (c) heavier gaugino pair production to the total trimuon SUSY cross section shown in Fig. 5.10(d).

Reference point

In CMS the mSUGRA parameter space corresponding to the reach of the first few years of LHC running at $\sqrt{s} = 14$ TeV is characterized by a set of low mass (LM) benchmark points presented in Tab. 5.1. The region close to the Tevatron exclusion limit is represented by LM0, which is defined by the mSUGRA parameters

$$m_0 = 200 \text{ GeV}, \quad m_{1/2} = 160 \text{ GeV}, \quad \tan\beta = 10, \quad A_0 = -400, \quad \mu > 0 \quad . \quad (5.15)$$

This benchmark point has been defined in common by the collaborations of the CMS and ATLAS experiments. The large cross section ($\sigma_{SUSY} = 110$ pb) offers the possibility to inspect this region of parameter space during the first year of LHC running at $\sqrt{s} = 10$ TeV. Therefore LM0 has been chosen as reference point of this analysis. At LM0 squarks and gluino are relatively light and in the same mass range:

$$m_{\tilde{g}} \sim m_{\tilde{q}} \sim 400 \text{ GeV} \quad , \quad (5.16)$$

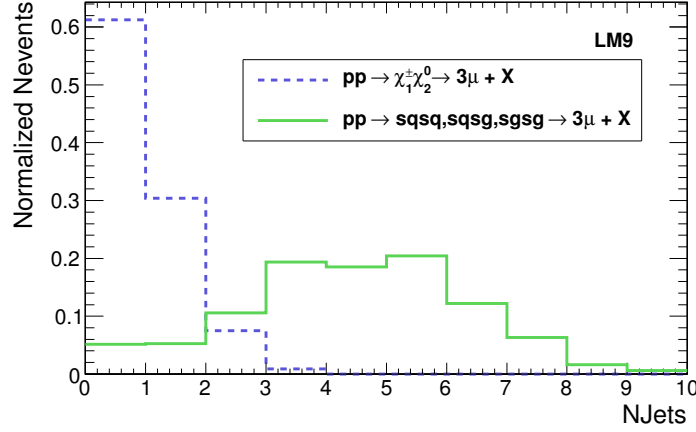


Figure 5.12: Jet multiplicity ($ET > 30$ GeV, $|\eta| < 3$, IC05) of SUSY trimuon events from direct neutralino-chargino production and gluino and squark cascade decays at the benchmark point LM9 ($m_0 = 1450$ GeV, $m_{1/2} = 175$ GeV, $\tan\beta = 50$, $A_0 = 0$, $\mu > 0$).

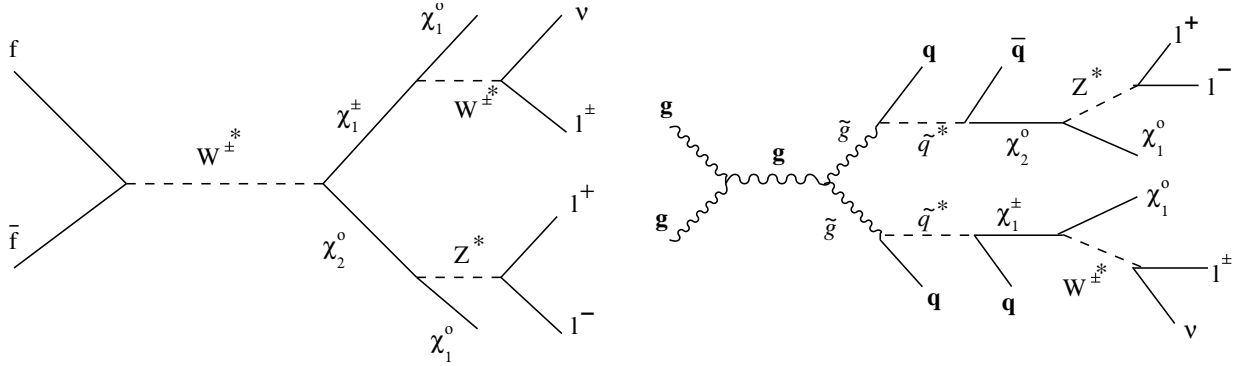


Figure 5.13: Typical diagrams for the trimuon production in SUSY from gaugino (L) and gluino (R) pair production at LM0.

and the lighter gauginos are lighter than sleptons:

$$m_{\chi_1^0} \sim 60 \text{ GeV}, \quad m_{\chi_2^0} \sim m_{\chi_1^\pm} \sim 113 \text{ GeV} < m_{\tilde{l}} \sim 200 \text{ GeV} \quad . \quad (5.17)$$

Therefore the squark and gluino production carries most part of the SUSY cross section and is the main source of trimuon final states, whereas the direct neutralino-chargino pair production contributes only $\sim 4\%$. Due to heavy sleptons and small mass difference $\Delta m(\chi_2^0, \chi_1^0)$, the neutralino χ_2^0 decays in three-body decays to muons with a typical branching ratio

$$\text{BR}(\chi_2^0 \rightarrow \mu^+ \mu^- \chi_1^0) \sim 3\% \quad , \quad (5.18)$$

thus SUSY events with muonic neutralino χ_2^0 decays can be identified with $M_{\mu\mu} < M_Z$. Also the chargino χ_1^\pm decays to muons in three-body decays with the branching ratio

$$\text{BR}(\chi_1^\pm \rightarrow \mu\nu_\mu\chi_1^0) \sim 11\% \quad . \quad (5.19)$$

Fig. 5.14 presents the transverse momentum of muons and the jet energy distribution for SUSY signal and SM backgrounds discussed in the following section. The samples have been preselected with three muons ($PT > 3$ GeV, $|\eta| < 2.1$) and the standard CMS track quality requirement (see Section 5.4.1). The SUSY sample has been selected requiring three prompt muons from gaugino decays, for the SM background samples also muons from jets (i.e. fake muons) have been taken into account. Fig. 5.15 presents the jet multiplicity and scalar sum of jet ET (HT). The jets are reconstructed using the iterative cone algorithm with a cone size $\Delta R < 0.5$ (IC05). Additionally, Fig. 5.15 shows the calorimeter missing transverse energy as well as the dimuon invariant mass of all OS muon pairs. In the low mass SUSY region, where the mass difference of gauginos is small, the production of the lightest neutralino in the decay of gauginos leads to softer muons compared to muons from W and Z boson decays. The jet energy and jet multiplicity is rather large, because SUSY trimuon events at LM0 are dominantly produced in gluino and squark cascade decays. The large missing transverse energy arises from neutrinos and the lightest neutralinos.

5.2 Standard Model Background

Any reaction which can produce the trimuon signature in the final state can be a potential background for the trimuon SUSY search. Among the diboson production ($pp \rightarrow ZZ, ZW$), there are other channels mimicking the trimuon signature with additional fake muons from jets. The SM background processes can be split in groups according to their prompt and fake muon multiplicity. The corresponding distributions of muons, jets and MET are presented in Fig. 5.14 and Fig. 5.15. Table 5.1 summarizes the considered SM background channels and their cross section.

SM Background with three Prompt Muons

Among the diboson (VV +jets) production, the Z/γ^*W production, the SM partner process of the direct $\chi_2^0\chi_1^\pm$ pair production, gives exactly 3 prompt isolated muons in the final state and forms the major irreducible background of the trimuon search. The branching ratio of Z and W boson decays to muons is $\sim 3\%$ and $\sim 11\%$, respectively. The ZZ production with the subsequent decay of Z bosons to muons gives 4 prompt muons in the final state and appears as a trimuon final state if one of the muons is produced outside of the detector acceptance or is rejected by the muon selection. Most of these events can be suppressed by a veto on the Z boson invariant mass in the $M_{\mu\mu}$ distribution, but the γ^* contribution and also wrong combinations of muons contribute to the signal region at $M_{\mu\mu} < M_Z$. The transverse momentum of all muons in SM diboson trimuon events is rather large, since the muons origin from Z and/or W boson decays. Fig. 5.16 shows typical diagrams for the

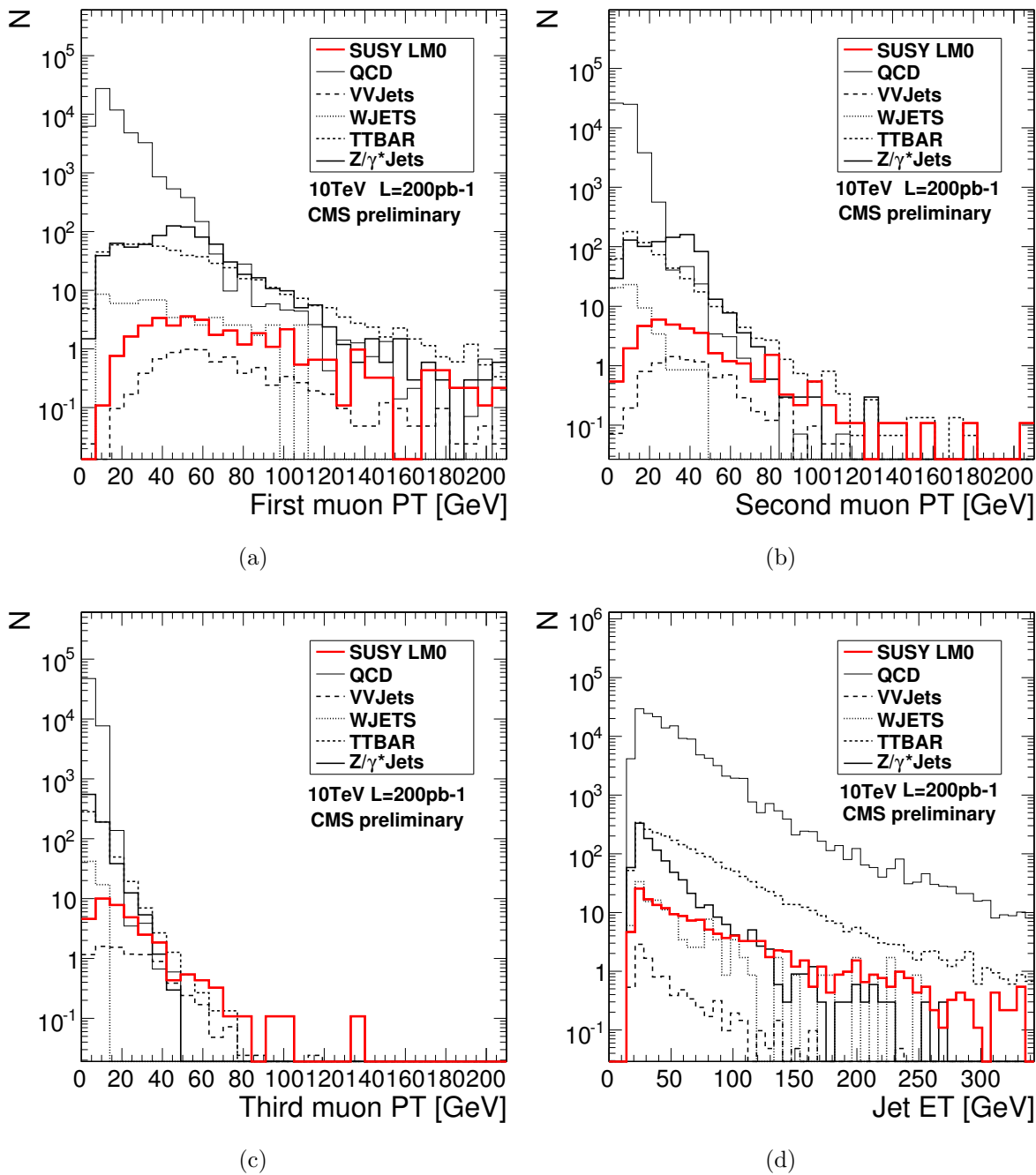


Figure 5.14: PT distribution of the first (a), second (b) and third (c) muon ordered by PT , as well as the transverse energy of jets ($|\eta| < 3$, IC05) (d) for SUSY LM0 and SM backgrounds after requiring at least three reconstructed muons with $PT > 3$ GeV, $|\eta| < 2.1$ and acceptable track quality.

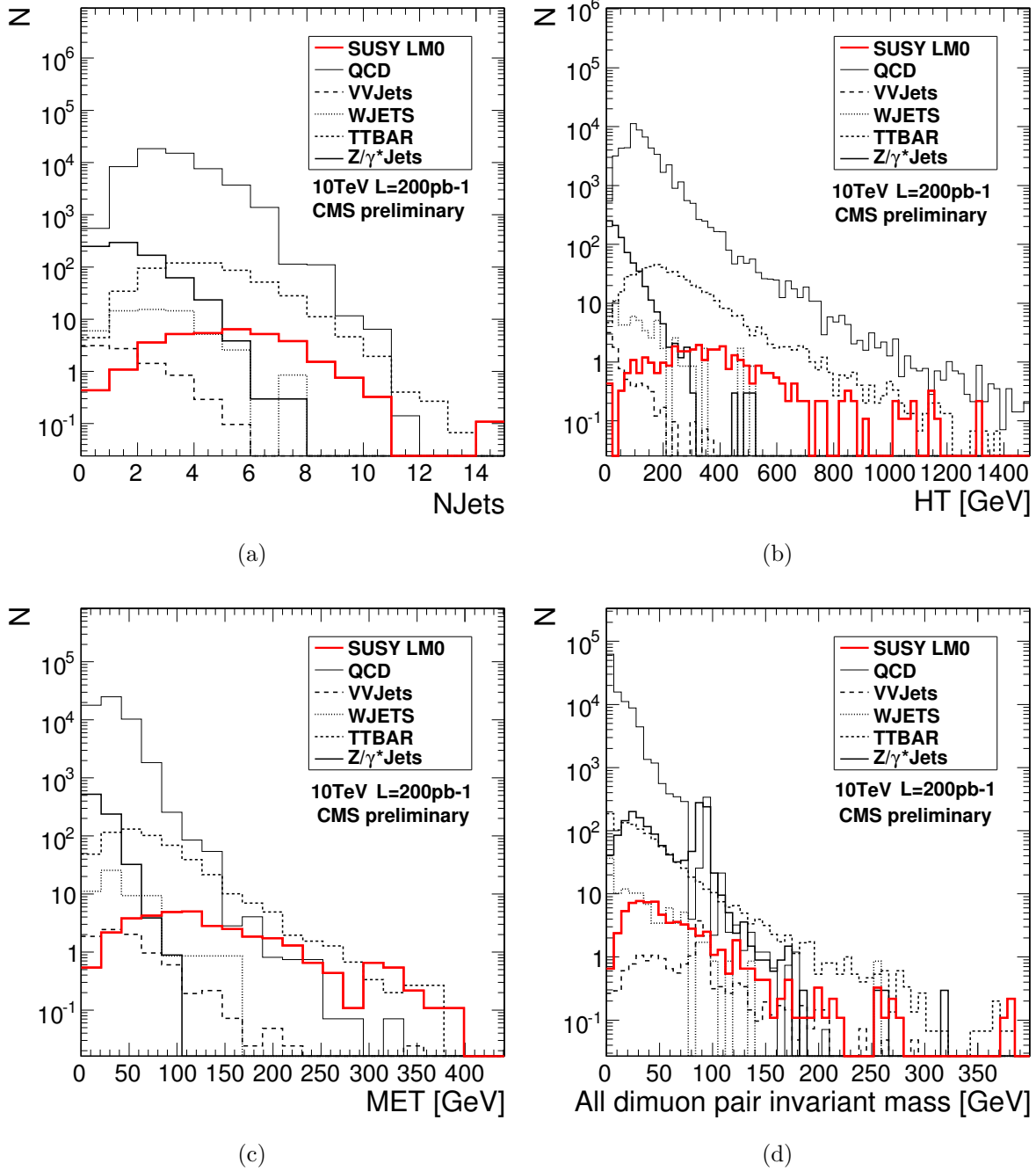


Figure 5.15: Multiplicity (a) and sum of ET (HT) (b) of jets ($ET > 30$, $|\eta| < 3$, IC05) as well as the calorimeter missing transverse energy (c) and the dimuon invariant mass distribution of all OS muon pairs (d), for SUSY LM0 and SM backgrounds after requiring at least three reconstructed muons with $PT > 3$, $|\eta| < 2.1$ and acceptable track quality.

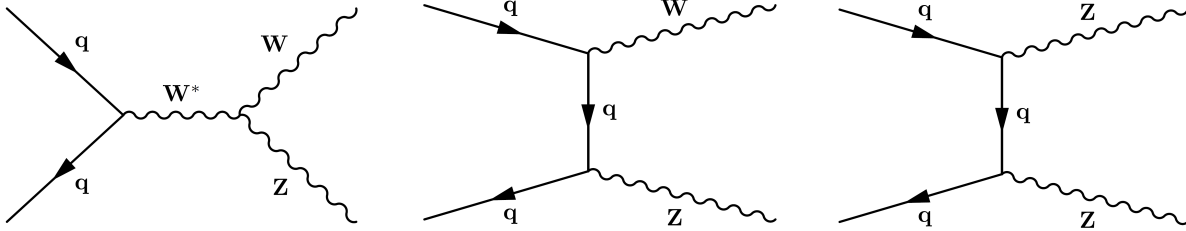


Figure 5.16: Typical diagrams for the ZW and ZZ diboson production [102].

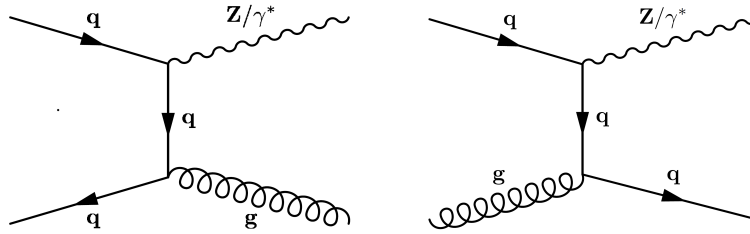


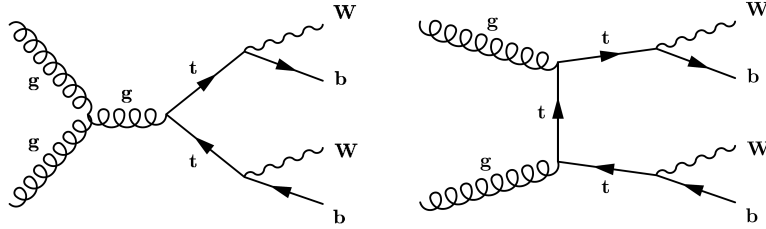
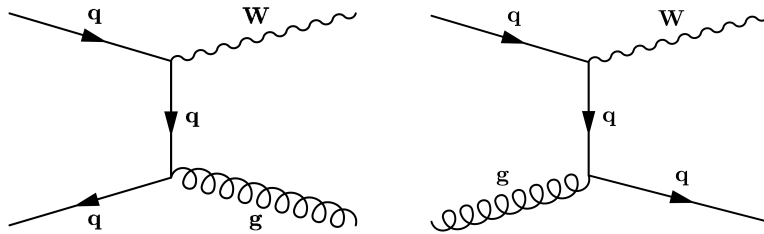
Figure 5.17: Typical diagrams for the Z +jets production [102].

ZW and ZZ diboson production at LHC. Other channels with 3 muons from bosons in the final state, like the WWW and $t\bar{t}W$ production, have a negligible cross section ($< 0.5fb$) at LHC energies [103].

SM Background with two Prompt Muons

In addition to the SM channels with three muons originating from boson decays, the processes with two muons from bosons and one additional muon produced in jets form a dangerous background for the trimuon search. Due to the large cross section, the most important processes of this kind are the Z/γ^* +jets and $t\bar{t}$ +jets production. The WW +jets diboson production has a smaller cross section and is less important. The Z/γ^* +jets channel (Fig. 5.17) includes the DY processes and the associated production of a Z boson with light (u, c, s) and heavy quarks (c, b). The dimuon final state in $t\bar{t}$ events (Fig. 5.18) is produced with heavy quarks, since the t -quark decays almost exclusively to a W boson and a b -quark, and escaping energy from the neutrinos produced in leptonic decays of the W boson. The first and second muon are hard, since they origin from W and Z boson decay, whereas the third muon is rather soft, since it is produced in jets. Due to the production of heavy quarks and the escaping energy from neutrinos, the jet and MET distribution for $t\bar{t}$ events is comparable to the SUSY production, thus forming the major background for the most SUSY searches.

In the trimuon search an optimized muon selection is the key to reject both Z/γ^* +jets and $t\bar{t}$ events. The gauge boson production can be relatively well simulated at LHC energies,

Figure 5.18: Typical diagrams for the $t\bar{t}$ production [102].Figure 5.19: Typical diagrams for the W +jets production [102].

but the rate of fake muons from jets depends on numerous factors including uncertainties in soft gluon radiation and gluon splitting, jets fragmentation and reconstruction and muon isolation efficiency. These factors introduce large systematic uncertainties in the estimation of these SM backgrounds. Therefore data-driven methods to control the contribution of events with fake muons have been developed.

SM Background with less than two Prompt Muons

Since the W +jets production has only one prompt muon in the final state, two additional fake muons from jets are required to mimic the trimuon signature. In spite of the large cross section, this channel can be effectively suppressed by an optimized muon selection. By definition the QCD processes have no prompt muon in the final state and therefore mimic the trimuon signature with 3 fake muons from jets. Hence, the second and third muon from the W +jets production and all muons from the QCD channels are soft. Since the large cross section prevents the detailed analysis of the QCD channels, also an muon enriched QCD data sample has been used to verify the QCD suppression.

5.3 Monte Carlo Datasets

The signal and the SM background channels have been studied with official CMS data samples available in the CMS database. The samples have been simulated with the software release CMSSW2.1_X and CMSSW2.2_X in the *summer08* and *fall08* CMS production

MC sample	Generator	cs[μb] LO	NEvents
SUSY ($m_0, m_{1/2}, \tan\beta, A_0, \text{sgn}\mu$)			
LM0 (200,160,10,-400,1)	SoftSusy+SusyHit+PYTHIA	110	200k
LM1 (60,250,15,0,1)	SoftSusy+SusyHit+PYTHIA	16.06	240k
LM2 (185,350,35,0,1)	SoftSusy+SusyHit+PYTHIA	2.42	240k
LM3 (330,240,20,0,1)	SoftSusy+SusyHit+PYTHIA	11.79	240k
LM4 (210,285,10,0,1)	SoftSusy+SusyHit+PYTHIA	6.7	200k
LM5 (230,360,10,0,1)	SoftSusy+SusyHit+PYTHIA	1.94	230k
LM6 (85,400,10,0,1)	SoftSusy+SusyHit+PYTHIA	1.28	220k
LM7(3000,230,10,0,1)	SoftSusy+SusyHit+PYTHIA	2.9	240k
LM8 (500,300,10,-300,1)	SoftSusy+SusyHit+PYTHIA	2.86	200k
LM9(1450,175,50,0,1)	SoftSusy+SusyHit+PYTHIA	11.58	200k
LM10(3000,500,10,0,1)	SoftSusy+SusyHit+PYTHIA	6.55	200k
LM11(250,325,35,0,1)	SoftSusy+SusyHit+PYTHIA	3.24	210k
Standard Model			
$VV+\text{jets}(V=Z,W \rightarrow e,\mu,\tau)$	MadGraph+PYTHIA	11.8	200k
$Z/\gamma^*+\text{jets}(Z \rightarrow \mu)$	PYTHIA	1944	1.3M
$Z/\gamma^*+\text{jets}(Z \rightarrow \tau)$	PYTHIA	1944	1.1M
$t\bar{t}$	MadGraph+PYTHIA	317	1M
$W+\text{jets}(W \rightarrow e,\mu,\tau)$	MadGraph+PYTHIA	40000	10M
QCD100to250 ($HT=100-250\text{GeV}$)	MadGraph+PYTHIA	$1.5 \cdot 10^7$	15M
QCD250to500	MadGraph+PYTHIA	$4 \cdot 10^6$	5M
QCD500to1000	MadGraph+PYTHIA	14000	5M
QCD1000toInf	MadGraph+PYTHIA	370	1M

Table 5.1: Signal and SM background data samples and cross sections used in this analysis.

for physics at $\sqrt{s} = 10$ TeV. The summary of the signal and SM background channels is presented in Table 5.1.

The number of expected events for signal and backgrounds have been calculated with leading-order cross sections. All mSUGRA benchmark points and SM background processes have been simulated with the full detector simulation. The initial and final state radiation has been calculated in PYTHIA for all produced samples. Pile-up effects can be considered negligible at $\sqrt{s} = 10$ TeV and $\mathcal{L} \sim 10^{30} \text{ cm}^{-2}\text{s}^{-1}$ and have not been simulated. The full simulation has used the complete CMS detector in the ideal configuration, the uncertainties from miscalibration and misalignment have been taken into account by a smearing of the muon isolation and vertex resolution.

The SUSY signal was calculated in a few steps. With the given mSUGRA parameters ($m_0, m_{1/2}, \tan\beta, A_0, \mu > 0$) the sparticle mass spectrum has been calculated at the electroweak scale using the renormalisation group equations implemented in the SOFTSUSY (v. 2.18) package. The radiative corrections to decays of sparticles have been calculated with the SUSYHIT (v1.3) code. The Monte Carlo events have been simulated with PYTHIA (v. 6.25) using CTEQ6l PDF.

All SM backgrounds have been simulated with the MadGraph package interfaced to PYTHIA except for the Z/γ^* +jets data samples which have been simulated with PYTHIA itself. In order to reduce the size, the diboson VV +jets and the W +jets data samples have been simulated with leptonic decays of the W and Z bosons. The Z/γ^* +jets data samples have been simulated with a lower limit on the invariant mass $M_{l+l-} \geq 20$ GeV. The QCD data sample has been simulated in different bins according to HT , the sum of transverse energy of the partons produced in the hard interaction.

The QCD channel has been additionally studied with a bb +jets data sample simulated with MadGraph and a muon enriched QCD sample simulated with PYTHIA. The bb +jet production has been considered already in the QCD sample. Therefore the bb +jets sample has been used to cross check the results with larger MC statistics. The muon enriched QCD sample has been produced with a lower limit on the transverse momentum of the outgoing partons $PT > 20$ GeV by filtering events with a least one muon ($PT \geq 15$ GeV). Long lived mesons (π^\pm, K^\pm) have been decayed on generator level.

Private data samples have been generated with the fast simulation of the CMS detector, which has been validated to agree with the full simulation of the CMS detector, for evaluation of the discovery reach in the mSUGRA mass plane for $\tan\beta = 3, A_0 = 0$ and $\mu > 0$ and for the comparison of MC generators SHERPA and ALPGEN.

5.4 Muon Selection

This study has attempted to search for SUSY using only muons for selection, since muons are considered to be the most robust physics objects in CMS. All other variables, including jets and missing transverse energy have been avoided in order to reduce the systematic uncertainties and the model dependence of the selection. Therefore the selection of muons is the key of the trimuon search and has to provide a large selection efficiency for prompt muons, a high rejection of fake muons from jets and a small sensitivity to systematic uncertainties.

5.4.1 Muon Identification

The parameters used for the muon identification are motivated by the differences of prompt muons (Section 5.4.2) and fake muons (Section 5.4.3). The muon identification, which has been used for the trimuon search, is based on three pillars:

- a global muon consisting of a reconstructed track in both, the silicon tracker and the muon system, with good muon track quality. The track quality has been determined by the normalized- χ^2 (χ^2/dof) of the global track and the number of valid hits N_{Hits} in the silicon tracker. The muon identification was thoroughly studied at CMS and the *GlobalMuonPromptTight* selection with $\chi^2/dof \leq 10$ was recommended with an additional requirement on the silicon track $N_{Hits} \geq 11$. This selection has also been used for muon identification in the presented analysis. Fig. 5.20 presents the corresponding muon selection efficiency.
- the relative isolation of the muon. The isolation has been determined in a cone around the muon track defined by $0.01 < \Delta R = \sqrt{\Delta\eta^2 + \Delta\phi^2} < 0.3$ and was calculated in the tracker (*isoTr*) by the sum of transverse momentum of all tracks and in the calorimeter (*isoCal*) by summing up the energy deposition in the ECAL and HCAL. The relative tracker isolation $isoTr/PT$ and the relative calorimeter isolation $isoCal/PT$ weights the isolation with the transverse momentum of the muon i.e. low *PT* muons were required to be better isolated than high *PT* muons. The requirement of isolated muons (i.e. small values of $isoTr/PT$ and $isoCal/PT$) is a powerful discriminant to reject all kind of fake muons, since all fake muons are produced in jets.
- the impact parameter significance S_{dxy} calculated as the impact parameter d_{xy} divided by its uncertainty σ_{dxy} . The impact parameter has been determined as the distance in the x - y -plane of the muon track and the primary vertex of the event. Instead of the impact parameter the significance has been considered, since a selection on the significance automatically scales with the vertex resolution, so when at the beginning the vertex resolution is worse, the selection will be looser.

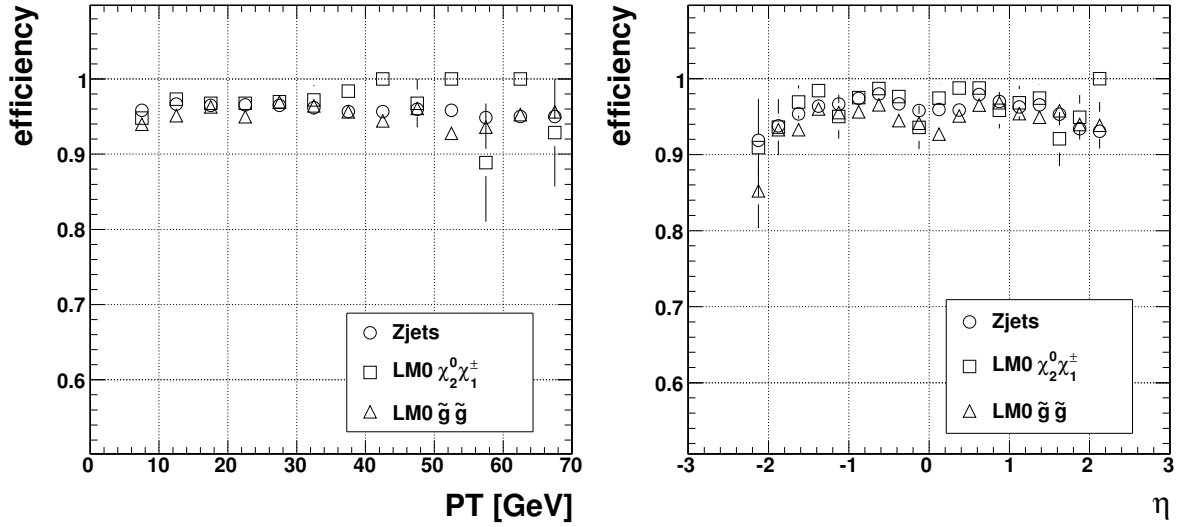


Figure 5.20: PT and η ($PT > 5$ GeV) dependence of the muon selection efficiency using the track quality criteria $N_{Hits} \geq 11$ and $\chi^2/dof \leq 10$ for muons from $Z/\gamma^* + \text{jets}$, direct neutralino-chargino and gluino production.

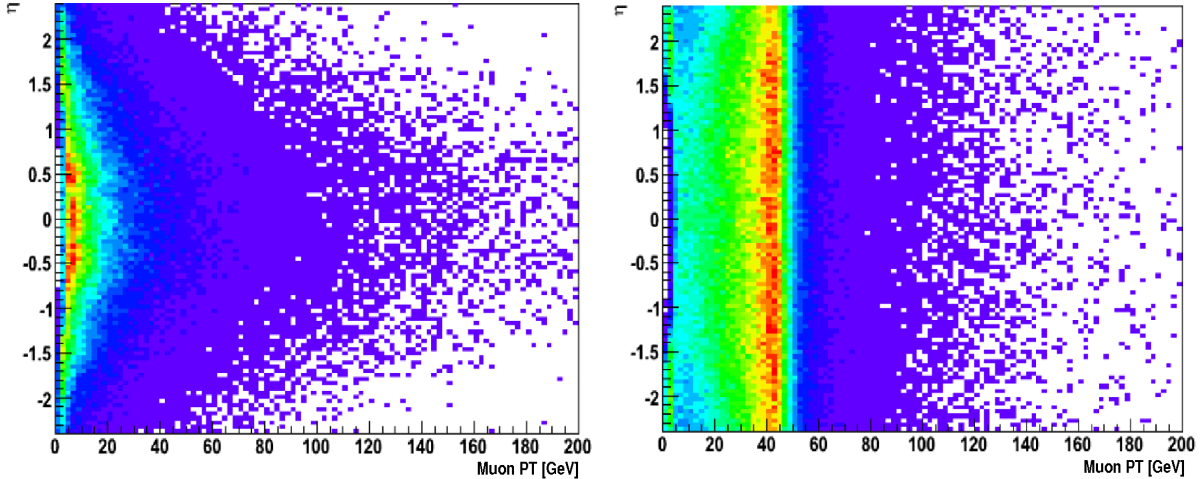


Figure 5.21: PT - η distribution of prompt muons from LM0 (left) and $Z + \text{jets}$ (right). Clearly, the muons from SUSY are considerably softer and more central.

5.4.2 Prompt Muons

In the trimuon SUSY search prompt muons have been defined as muons coming from the decay of SM bosons and gauginos. The characteristic properties of prompt muons correspond to the production mechanism. Prompt muons appear isolated in the detector, since

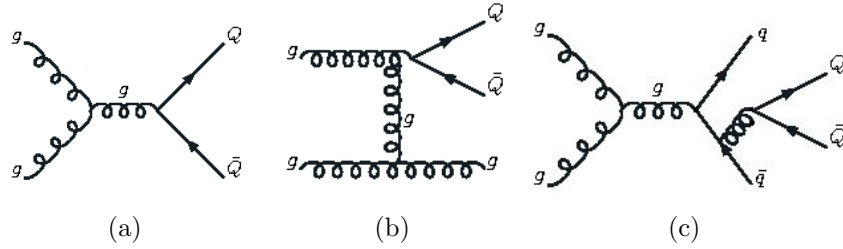


Figure 5.22: Typical heavy flavor production.

they are produced in a clean decay without additional particles producing tracks in the tracker and energy deposit in the calorimeter around the muon track. The mother particle has a short lifetime and decays immediately after production. Therefore the track of the muon should be close to the primary vertex of the event and the fit of global track is expected to have a good quality.

There is a difference between SUSY muons and muons from SM boson decays. In the low mass SUSY region where the mass difference of gauginos is small, the production of the lightest neutralino χ_1^0 from decay of the gaugino results in a softer muon PT distribution. The more heavy the initially produced particles are, the more central in the detector the muons are. Therefore muons produced in SUSY processes are more central than in SM processes. Fig. 5.21 shows the PT vs. η distribution of prompt muons from SUSY LM0 and Z +jets events.

SUSY trimuon events from cascade decays of gluino and squarks are produced with a large number of central jets. The high jet multiplicity environment results in larger activity in the calorimeter and tracker around the muon track, which affects the selection efficiency, because the isolation criteria is harder to fulfill. The tracker and calorimeter isolation distributions of prompt muons from SUSY and Z +jets are shown in Figure 5.26.

5.4.3 Fake Muons

Fake muons have been defined as all muons, which are not coming from SM bosons and gauginos and can be categorized as follows.

- Muons from decays of heavy flavor hadrons consisting of b , c quarks produced in the hard process and in gluon splitting (Fig. 5.22). Heavy flavor hadrons have a non-zero lifetime ($c\tau \sim 0.1-0.5$ mm) [3] and can travel through the tracker before decaying. Consequently those muons can have a displaced vertex and can be identified by the impact parameter significance. Mostly, muons from heavy flavor decays can be distinguished from prompt muons by the muon isolation criteria, since they are produced in jets. However those muons are the main source of fake muons after the isolation criteria is applied. The remnants of the heavy flavor decays can be outside

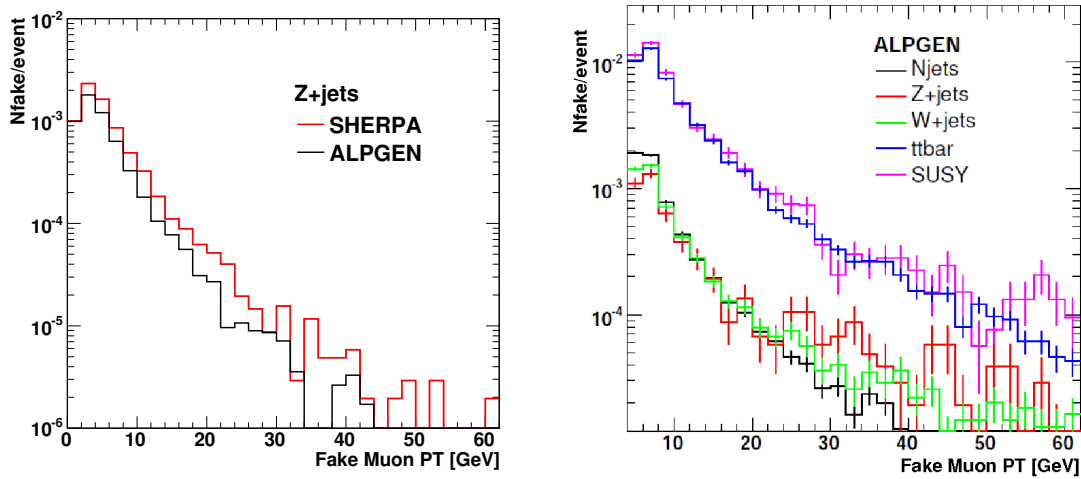


Figure 5.23: PT distribution of fake muons after loose isolation cut $isoPT < 5$ GeV in the Z +jets production simulated with MC event generators SHERPA and ALPGEN (L) and in different production channels simulated with ALPGEN (R). The distributions are normalized to the number of events. The fake muon production is prone to large theoretical uncertainties (L), the PT distribution for fakes in different channels is rather similar and the fake rate in the different channels depend on the heavy flavor content of the event (R).

the isolation cone or the muon hold the major part of the energy and the remnants are too soft to contribute significantly to the momentum/energy deposit in the isolation cone.

- Muons from decays of long living mesons (K^\pm , π^\pm). The large mean lifetimes of long living mesons $c\tau(K^\pm) \sim 3.7$ m and $c\tau(\pi^\pm) \sim 7.8$ m [3] result in in-flight decays in the detector, which affects the quality of the muon track. The normalized- χ^2 of the global track is a powerful tool to reject such muons, as well as the isolation requirement.
- Escaping charged particles from the calorimeter can produce some tracks in the muon system and can be misidentified as muons, the so called punch-through muons. These kind of fake muons can be effectively rejected by the track quality and isolation requirements and yield a negligible contribution with the muon selection used in this analysis.

The production rate of fake muons is prone to large systematic uncertainties. The contribution of fake muons from heavy flavor decays has large uncertainties from quarks produced in initial and final state radiation in the parton shower evolution, since it is sensitive to the gluon parton distribution function and the splitting probability into heavy quarks. The process of gluon splitting into a heavy-quark pair is one of the elementary processes in QCD but is poorly known, both theoretically (e.g. [104]) and experimentally (e.g. [105]).

The gluon splitting rate is sensitive to α_s and m_Q , which results in theoretical uncertainties [106].

The sensitivity to MC details was checked with Z +jets samples simulated with different MC generators. As already mentioned, the most dangerous SUSY trimuon background processes mimic the trimuon signature with fake muons and their contribution after the final selection depends on the number of fakes passing the muon selection. Fig. 5.23 shows the PT distribution of fake muons normalized to the number of events after a loose isolation requirement ($isoPT < 5$ GeV) for ALPGEN and SHERPA. The difference of the fake muon contribution in different generators demonstrates the importance of a good understanding of the fake muon contribution. The fake muon production has been also checked for different channels using the same generator. Fig. 5.23 shows the PT distribution of fake muons after a loose isolation requirement ($isoPT < 5$ GeV) for the QCD, Z +jets, W +jets, $t\bar{t}$ and SUSY production simulated with ALPGEN. It can be concluded that fake muons produced in different channels with the same generator are rather similar and the fake rate mostly depends on the heavy flavor content of the event, since SUSY and $t\bar{t}$ have practically the same fake rate, while the fake rate for QCD and electroweak boson production is an order of magnitude lower.

In addition to the theoretical uncertainties of the fake muon production, the distributions of relative isolation and impact parameter significance are also related to the detector performance. The basic idea of the muon selection in the trimuon search is to measure these quantities from the data to reduce the newly introduced uncertainties e.g. selecting a prompt reference sample with a high purity of prompt muons and a fake reference sample with high purity of fake muons. The selection of such reference samples will be discussed in detail in the next section.

5.4.4 Fake and Prompt Reference Samples

The selection of a fake and a prompt reference sample provides the opportunity to control and study the parameters used for muon identification with data. In order to minimize the bias, the samples have been selected without using parameters of the muon itself. The only requirement has been the presence of a reconstructed global muon in the event. Furthermore, the cross section had to be large enough to provide a sufficient number of fake and prompt muons. Another requirement was the purity of the reference samples i.e. the background processes had to be strongly rejected (processes with fake muons for the prompt reference sample and processes with prompt muons for the fake reference sample). Therefore the chosen signal processes had to provide characteristic properties in order to be easily discriminated from the background.

The selection of reference samples has been done in the following steps. First the data samples were preselected with a suitable HLT stream. Then an exhaustive list of observables were considered to minimize the fake rate by comparing these samples. This was done with

a Genetic Algorithm (GA) provided by the GARCON package selecting the most sensitive parameters from the following list: MET, sum of ET , jets, muon kinematics, angular relations, invariant mass of dijets and dimuons, jet balance parameters, etc. After ranking of all input variables by the GA, the most sensitive parameters were selected. The following parameters have been used for the final selection of the prompt and fake reference samples:

- N_μ , the number of reconstructed global muons with $PT_\mu > 5$ GeV and $|\eta| < 2.1$
- N_{jet} , the number of jets with $ET > 30$ GeV and $|\eta| < 2.4$
- $M_{\mu\mu}$, the invariant mass of a opposite sign muon pair
- MET_{rec} , the missing energy calculated as a recoil of all selected jets and muons
- $ET_{eff} = \Sigma ET_j + \Sigma PT_\mu$, the transverse energy of all selected jets and muons
- $\phi(j_1j_2)$, the azimuthal angles between leading jets
- $\alpha_2 = ET_{j_2}/M_{j_1j_2}$, the balance parameter of jets
- $M_{MET,\mu}$, the transverse invariant mass of MET_{rec} and the leading muon.

Prompt Reference Sample

The prompt reference sample has been selected from the Z +jets production. Among all SM processes with prompt muon final states, the Z +jets production with leptonic decays of the Z boson provides the most suitable properties. Basically, the Z +jets sample can be selected by a pair of muons with an invariant mass compatible with the Z boson mass. The considered background processes are the QCD, W +jets and $t\bar{t}$ channels. Due to the presence of two prompt muons in leptonic decays of the Z boson, the most suitable HLT stream for preselection is the DoubleMu3 stream, where two muons with $PT_\mu > 3$ GeV are required. As shown in Table 5.2, already the requirement of two reconstructed muons rejects a large part of the QCD and W +jets background processes. The final selection cuts optimized with the GA as well as the number of prompt muons after the final selection for an integrated luminosity of $\mathcal{L}_{acc} = 100 \text{ pb}^{-1}$ are presented in Table 5.2. Fig. 5.24 shows the distributions of observables used for the final selection for Z +jets, VV +jets and all background processes after the HLT preselection. The prompt reference sample can be selected with $\sim 10^5$ prompt muons and a small contamination of fake muons $\sim 10^{-4}$ coming from the W +jets production. The robustness of the selection has been checked by changing the jet energy by $\pm 10\%$. The number of fake muons changes by $\sim 40\%$, which is acceptable given the small contamination.

Observables	Selection	Sample	HLT[%]	Nev 100 pb ⁻¹
HLT Trigger	DoubleMu3	Z+jets	35	42560
N_μ	=2	VV+jets	52	140
$M_{\mu\mu}$	70-180 GeV	QCD100to250	5	0
N_{jet}	<2	QCD250to500	10	0
MET_{rec}	<100 GeV	QCD500to1000	17	0
ET_{eff}	<120 GeV	QCD1000toInf	29	0
		$t\bar{t}$	48	1
		W+jets	26	2.7

Table 5.2: Selection criteria of the prompt reference sample and expected statistics of prompt muons ($\times 2$) from the Z +jets and VV +jets production for an integrated luminosity of $\mathcal{L}_{acc} = 100 \text{ pb}^{-1}$.

Fake Reference Sample

The fake reference sample has been selected from QCD events. The large cross section of the QCD processes compared to the boson production provides an excellent opportunity for selecting a high purity fake muon sample. Basically, the sample can be selected by requiring two hard jets balanced in PT . The considered backgrounds are all processes with bosons i.e. the W +jets, Z +jets and VV +jets production. The most suitable HLT stream for preselection is the DiJet70, where two jets with $ET_{jet} > 70 \text{ GeV}$ are required. Again, the final selection has been optimized with the GA. The final selection as well as the number of muons in the selected fake sample for an integrated luminosity of $\mathcal{L}_{acc} = 100 \text{ pb}^{-1}$ are shown in Table 5.3. The distributions of parameters used for the final selection are shown in Fig. 5.25 for the QCD signal and the boson background production after HLT preselection. It has been demonstrated, that $\sim 10^7$ fake muons can be selected with a small contamination of prompt muons $\sim 10^{-4}$ coming from the W +jets production. The jet energy scale has been varied by $\pm 10\%$ to check the robustness of the selection. The impact of the jet energy scale uncertainties on the number of selected prompt muons is in an acceptable range of $\sim 20\%$.

5.4.5 Optimization of the Selection

The selection of prompt muons and the rejection of fake muons is based on three major parameters: the relative muon isolation in the tracker $isoTr/PT$ and calorimeter $isoCal/PT$ as well as the impact parameter significance $S_{dxy} = dxy/\sigma$. As already mentioned, the fake muon production is prone to large theoretical uncertainties and the distributions need to be compared with MC expectations. Also the detector performance affects the distributions, i.e. the resolution in impact parameter is expected to be of the order of $10 \mu\text{m}$ for a perfectly aligned detector [107] (see Fig. A.2), but the alignment position error is expected to become negligible only after $\mathcal{L}_{acc} = 100 \text{ pb}^{-1}$ [108], so the impact parameter resolution will vary as function of accumulated luminosity. Therefore the MC predictions

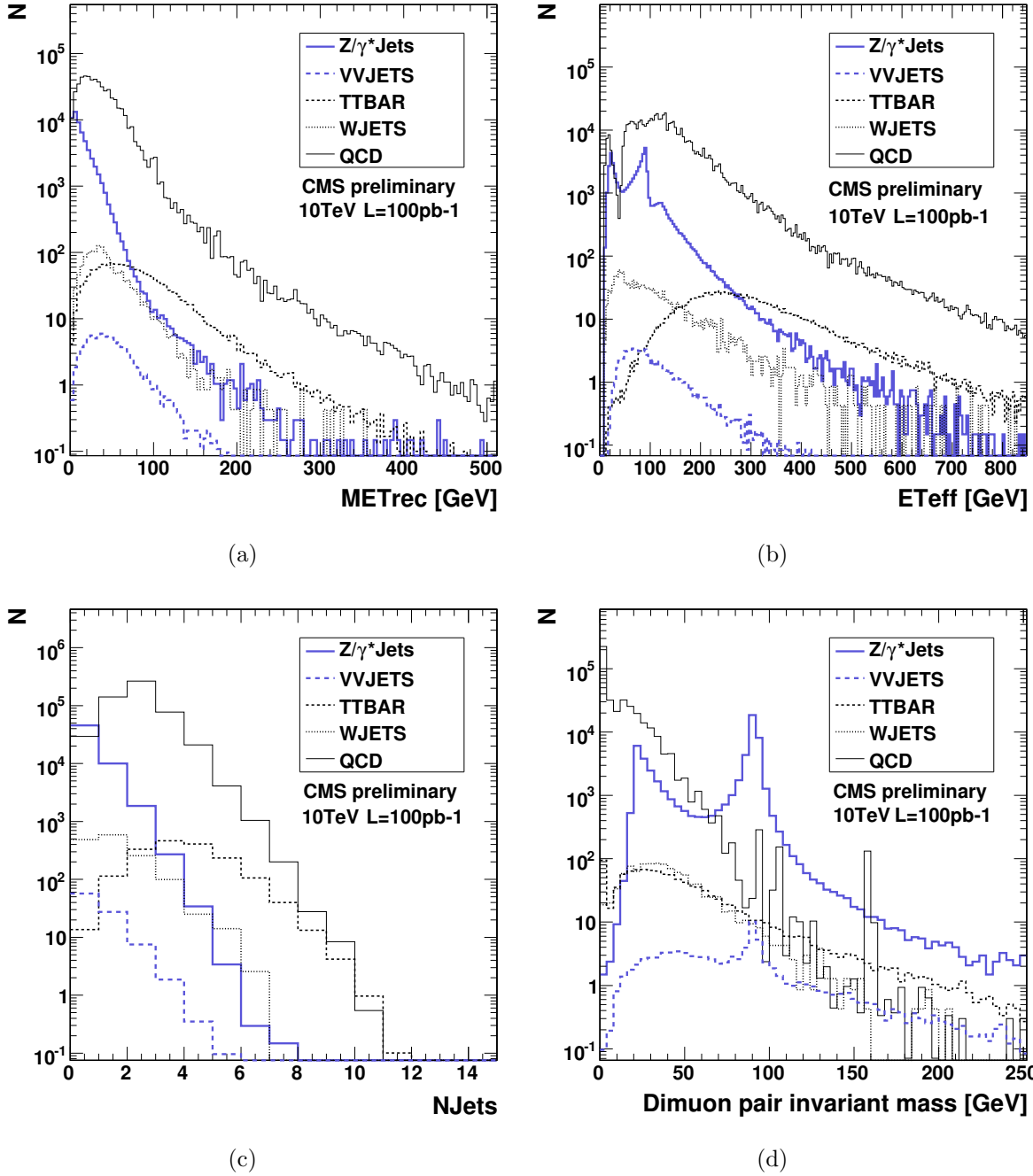


Figure 5.24: Distributions of parameters used for selection of the prompt reference sample from the Z +jets production after requiring two reconstructed muons with $PT > 5$ GeV, $|\eta| < 2.1$ in the HLT DoubleMu3 trigger stream ($PT > 3$ GeV). The main selection cut is the invariant mass requirement $70 \text{ GeV} < M_{\mu\mu} < 180 \text{ GeV}$.

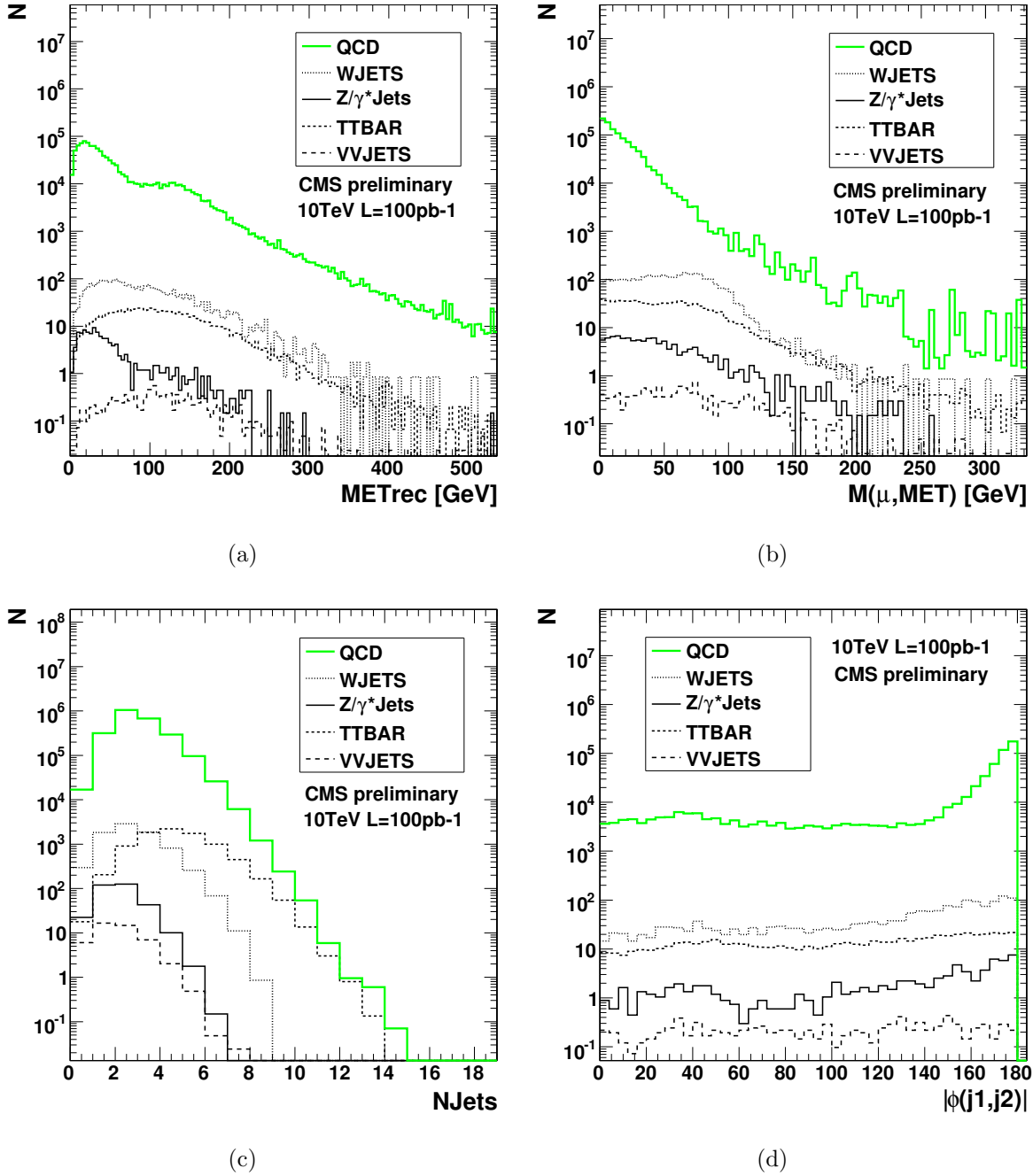


Figure 5.25: Distributions of parameters used for the fake sample selection from the QCD channels after requiring $N_\mu \geq 1$ with $PT_\mu > 5$ GeV, $|\eta_\mu| < 2.1$ in the HLT Dijet trigger stream ($PT > 70$ GeV). Except for the jet multiplicity, the samples have been selected with $N_{jet} = 2$. The main selection cuts are $N_{jet} = 2$ and $160^\circ < |\phi(j1, j2)| < 180^\circ$.

Observables	Selection	Sample	HLT[%]	Nev 100 pb ⁻¹
HLT Trigger	DiJet70	QCD100to250	78	9430000
N_{jet}	=2	QCD250to500	100	362000
$\phi(j1, j2)$	160°-180°	QCD500to1000	100	15900
$\alpha2$	<0.42	QCD1000toInf	100	386
N_μ	>0	$t\bar{t}$	99	112
$M(MET, \mu)$	<40 GeV	W+jets	25	905
MET_{rec}	<100 GeV	Z+jets	38	338
		VV+jets	60	1.4

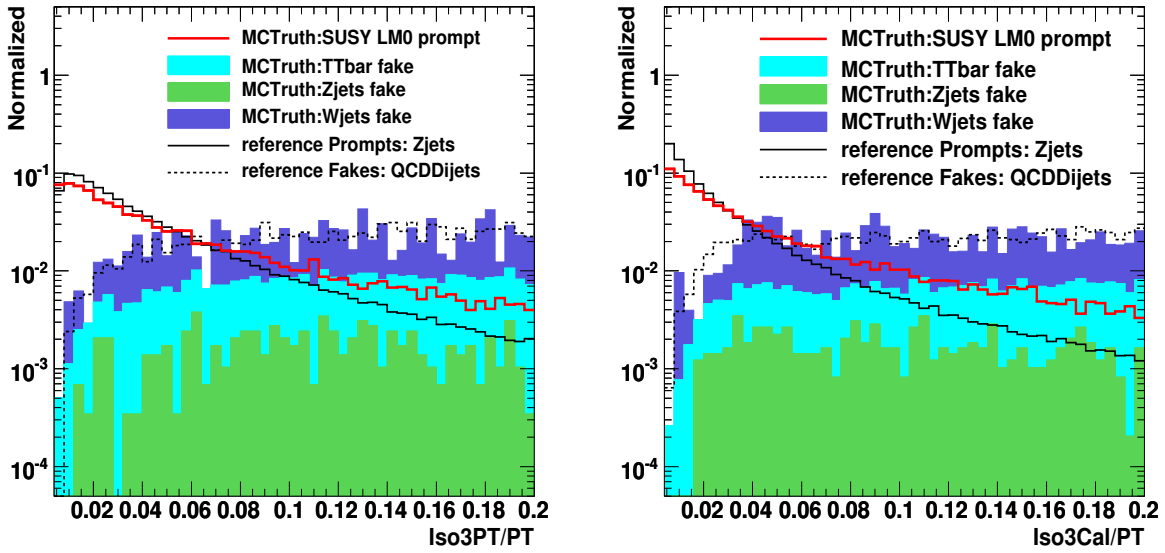
Table 5.3: Selection criteria of the fake reference sample and expected statistics of fake muons from the QCD channels at $\mathcal{L}_{acc} = 100 \text{ pb}^{-1}$.

of parameters used for the selection of fake and prompt muons needs to be verified with data. The distributions of parameters can be directly obtained from the reference samples and compared with the MC predictions.

Fig. 5.26 shows the distributions of relative isolation and impact parameter significance of muons from the fake and prompt reference samples, prompt muons from SUSY LM0 sample and fake muons from the SM background processes. A few observations are noteworthy:

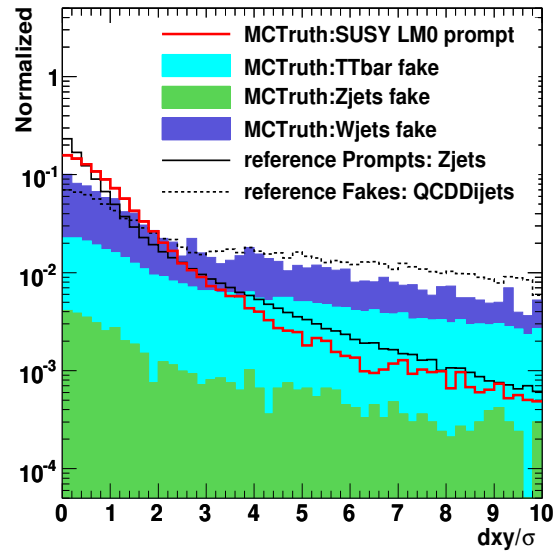
- Fake muons from the trimuon SM backgrounds Z/γ^* +jets, W +jets, and $t\bar{t}$ all have similar impact parameter $Sdxy$ and isolation distributions. This is not surprising, given that they all originate from similar sources.
- Prompt muons from the Z +jets reference sample have distributions reasonably close to the prompt muons expected for SUSY. The differences in isolation result from the different event topologies.
- Fake muons from the QCD reference sample have distributions reasonably close to the fake muons expected for the main SUSY backgrounds (Z/γ^* +jets, $t\bar{t}$).
- One observes that for larger values of relative isolations in tracker and calorimeter the main contribution from fake muons (Z/γ^* +jet, $t\bar{t}$) starts to dominate over the rate of prompt muons, both for the SUSY and reference samples.
- The same is true for larger impact parameter values. Therefore, by a simultaneous cut in impact parameter, isolation in calorimeter and isolation in tracker one can reduce the contribution from fake muons in the signal.

The sensitivity of the prompt and fake muon selection to the used parameters is shown in Fig. 5.27 and has been evaluated in the following way. For each selection cut value plotted on the x -axis the number of accepted prompt and fake muons has been counted. Then the object selection efficiency of prompt and fake muons has been calculated using these numbers, as well as the 'signal-over-noise' ratio, defined as $N_{prompt}/\sqrt{N_{fake} + \sigma_{sys}^2}$. The



(a) Relative tracker isolation

(b) Relative calorimeter isolation



(c) Impact parameter significance

Figure 5.26: Normalized relative isolations iso_{PT}/PT_μ , iso_{Cal}/PT_μ and impact parameter significance S_{dxy} in MC-truth samples of SUSY (LM0) and SM backgrounds as well as for the reference samples.

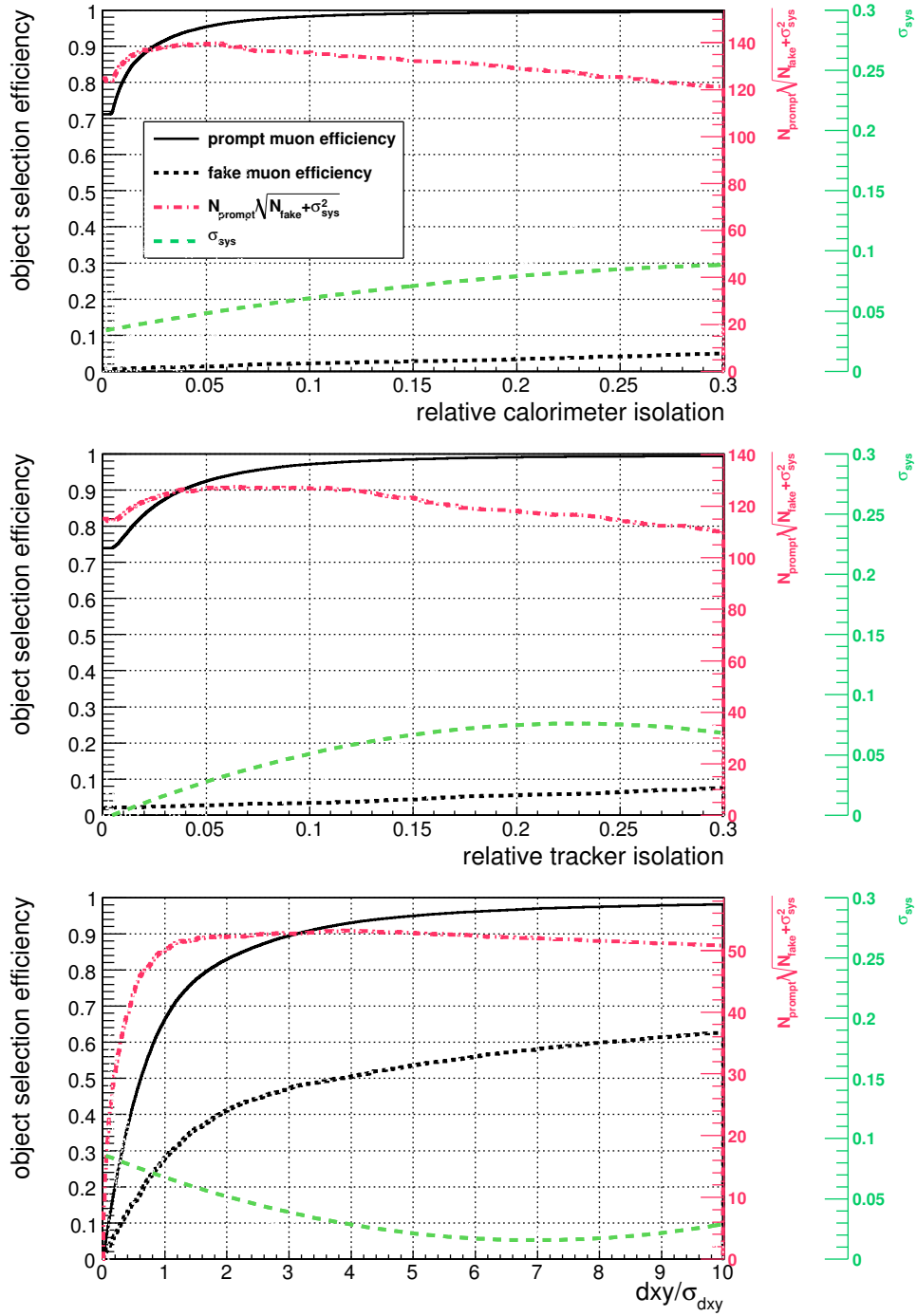


Figure 5.27: The efficiency of the prompt and fake muon selection together with the signal significance and sensitivity as a function of the three muon selection variables (from top to bottom). Here the prompt and fake muons are obtained from the reference samples.

systematic uncertainty σ_{sys} has been calculated for each selection cut by varying the value of the cut by $\pm 5\%$ and counting the variations in the number of selected objects $\Delta N/N$. The distributions of parameters used to separate prompt and fake muons are rather slowly varying. Thus, the precise selection cuts are not important. Also the sensitivity to the impact parameter resolution is not large, since a worse impact parameter resolution will smear both the signal and the background, so one can still well separate between tracks with small impact and large impact parameter. This will be discussed quantitatively in the section on systematic errors.

The muon selection has been optimized using prompt muons from the SUSY sample and fake muons from the SM backgrounds. The optimum selection evaluated by optimizing the signal over noise ratio $N_{prompt}/\sqrt{N_{fake}}$ with the GA has been obtained as

$$isoCal/PT < 0.08 \quad (5.20)$$

$$isoPT/PT < 0.08 \quad (5.21)$$

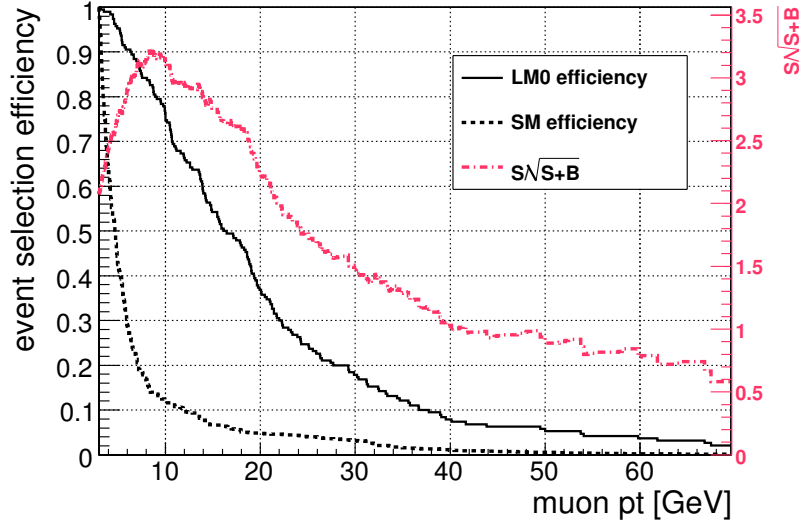
$$Sdxy < 4 \quad (5.22)$$

plus the standard CMS track quality requirements.

The cut on the muon transverse momenta is another sensitive measure to reduce the background processes. Since the SUSY muons are all soft for the parameter range of low SUSY masses considered in this analysis, also the minimum PT cut was selected to be the same for all three muons. The cut has been evaluated by scanning the significance $N_S/\sqrt{N_S + N_B}$ of prompt muons from the SUSY signal and fake muons from the SM background events as a function of the minimal PT cut after the requirement of exactly three selected muons in the event. The signal significance and the event selection efficiency for SUSY LM0 and SM backgrounds are shown in Fig. 5.28. The optimum minimum PT selection cut of $PT > 8$ GeV corresponds to the onset of the contribution from fake muons, which rises fast at low PT .

However, the presented analysis has attempted to estimate the SM background in a data-driven way using the sidebands of the relative isolation and the impact parameter significance. This data-driven background estimation would require larger statistics in the control regions, especially the statistics for large impact parameter $Sdxy$ and low isolation value is low. Therefore cuts have been relaxed somewhat without much changes in the signal significance. The final muon selection is shown in Table 5.4. The pseudorapidity selection corresponds to the trigger acceptance of muons.

The muons accepted by the final muon selection (kinetic and quality requirements) will be called 'tight' ('loose') muons. Note that *small* values of the isolation parameters imply little energy in the cone around the track, so they correspond to *good* isolation. The same selection was applied to all three muons, but the *relative* isolation, i.e. the isolation weighted with $1/PT$, will automatically increase the efficiency for the hardest muons in the event by reducing the energy requirements in the cone, while fake muons, which are soft,

Figure 5.28: Optimization of PT selection of SUSY muons.

kinetic requirements	$PT > 8\text{GeV}, \eta < 2.1$
track quality cuts	$\chi^2/dof < 10, N_{hits} \geq 11$
isolation criteria	$isoCal/PT < 0.15, isoPT/PT < 0.15$
impact parameter significance	$Sdxy < 4$

Table 5.4: Final muon selection used in the trimuon analysis.

are efficiently suppressed. Fig. 5.29 shows the selection efficiency for prompt muons from SUSY and $Z/\gamma^* + \text{jets}$ production. Due to the different event topologies, the average muon selection efficiency drops from $\sim 80\%$ for the direct neutralino-chargino pair production to $\sim 60\%$ for gluino and squarks cascade decays. Therefore the trimuon event selection efficiency for the gluino and squarks production is a factor ~ 2 worse than for the direct neutralino-chargino production.

5.5 Trimuon Event Selection

After optimization of the muon identification the event selection is simple in the trimuon analysis: exactly three selected muons with one pair having an opposite charge sign. The statistics for the signal and all SM background processes at different steps of selection is presented in Table 5.5 for an accumulated luminosity of $\mathcal{L}_{acc} = 200 \text{ pb}^{-1}$. From the fourth column on, the events have been required to be selected by the DoubleMu3 trigger stream. The trigger selection will be discussed in detail in Section 5.6.

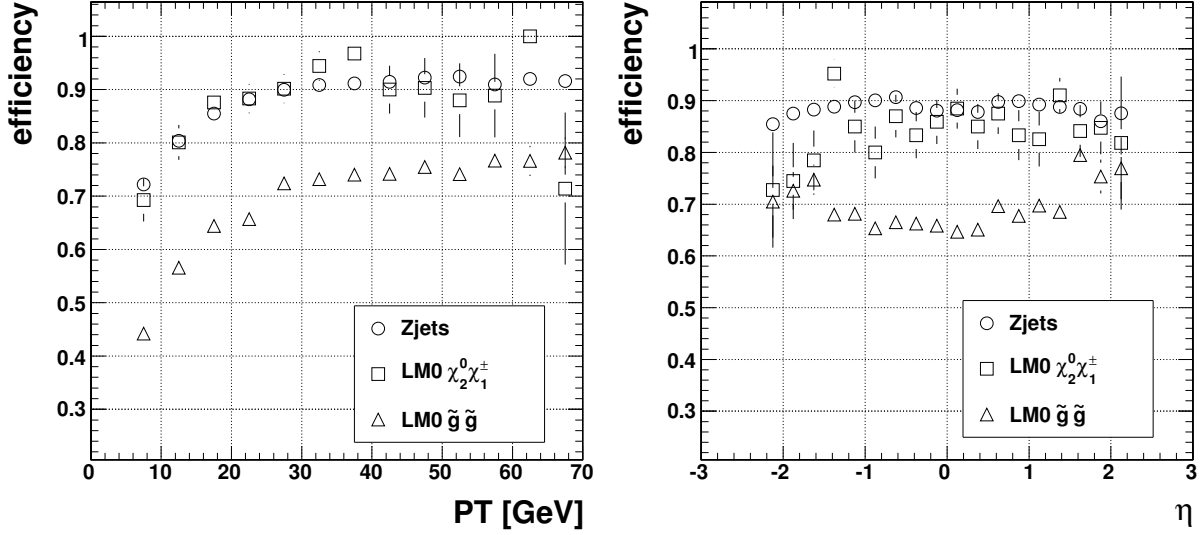


Figure 5.29: PT and η dependence of the selection efficiency using the final muon selection (Table 5.4) for muons from Z/γ^* +jets, direct neutralino-chargino and gluino production.

	cs[pb]	$N_{\mu}^{MC}=3$	$N_{\mu} \geq 3$ 'loose'	$N_{\mu}=2$ 'tight' + ≥ 1 'loose'	$N_{\mu}=3$ 'tight'	low OS pairs M[20,86]GeV
SUSY: LM0	110	50.5	187.4 ± 4.5	75.0 ± 2.9	17.8 ± 1.4	15.3 ± 1.3
SM:						
VV +jets	11.8	18.1	7.2 ± 0.4	6.5 ± 0.4	4.7 ± 0.3	2.8 ± 0.3
Z/γ^* +jets	3700	1789.5	203.8 ± 7.5	161.1 ± 6.9	8.3 ± 1.6	6.2 ± 1.4
$t\bar{t}$	317	944	223.3 ± 3.9	72.1 ± 2.2	0.4 ± 0.2	0.3 ± 0.1
W +jets	40000	119.5	10.3 ± 2.9	0	0	0
QCD	0.15mb	133607	2927.8 ± 659	0	0	0
Σ SM	-	136479	3372.4 ± 660	239.7 ± 7.2	13.4 ± 1.3	9.3 ± 1.4

Table 5.5: Statistics for the final selection of trimuon events for an integrated luminosity of $\mathcal{L}_{acc} = 200 \text{ pb}^{-1}$. The errors are given by the size of MC samples.

The third column shows the number of events with three muons ($PT > 3 \text{ GeV}$, $|\eta| < 2.1$) at generator level. For the signal (LM0 point) this is the number of events with exactly three prompt muons. For the background channels the number of events corresponds to events with at least three MC muons, either prompt or fake. The contribution of the QCD processes is the major background at this stage, the W +jets contribution is already small compared to the other background with fake muons.

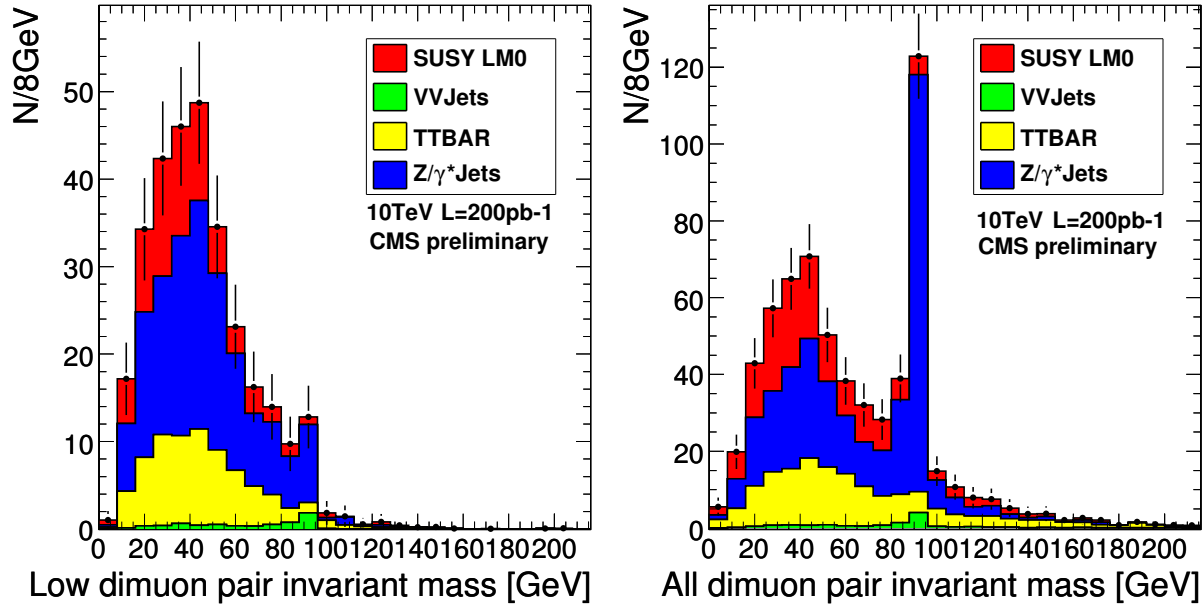


Figure 5.30: Invariant mass distribution of the lowest mass OS muon combination (left) and all OS combinations (right) after requiring 2 'tight' muons and at least one 'loose' muon for SUSY (LM0) and SM background processes at $\mathcal{L}_{acc} = 200 \text{ pb}^{-1}$ and $\sqrt{s} = 10 \text{ TeV}$.

After the requirement of at least 3 'loose' muons i.e. muons with an acceptable track quality, the QCD background still dominates the selected data sample but is strongly suppressed. Expectedly, the number of signal events with at least 3 muons is larger than the number with exactly three prompt muons at generator level, since also for SUSY fake muons contribute to the trimuon signature. The corresponding number of selected events is shown in the fourth column.

The fifth column shows the number of events with 2 'tight' and at least 1 'loose' muon. Expectedly, the SM background with 2 prompt muons dominates (Z/γ^* +jets and $t\bar{t}$) because of the large cross section compared to the SUSY and SM diboson (VV +jets) production. Fig. 5.30 shows the corresponding invariant mass distribution of the lowest mass OS muon combination and all OS combinations. At this stage of selection, the QCD contribution is already expected to be completely rejected. With real data the selected sample will be required to reproduce the shown distributions. This will serve as an additional verification of the used MC model and the QCD rejection. Since the large cross section prevents the detailed analysis, also a muon enriched QCD data and a separate bb +jets sample has been used to check the QCD suppression and will be discussed in the course of this section.

Furthermore, the requirement of exactly three 'tight' muons reject a large part of the Z/γ^* +jets and $t\bar{t}$ events, since the additional third fake muon is rejected by the tight

muon selection. As shown in the sixth column, the largest background contribution comes from Z/γ^* +jets and diboson production.

Since the invariant mass distribution of opposite sign (OS) muon pairs from χ_2^0 decays exhibits a particular shape with $M_{\mu\mu} < M_Z$ for two-body decays via sleptons and three-body decays, the final trimuon event selection has used the OS muon invariant mass for further rejection of backgrounds. The contribution of backgrounds with Z bosons decaying to OS muon pairs can be suppressed by requiring the OS muon invariant mass below the mass of the Z boson ($M_{\mu\mu} < 86\text{GeV}$). The OS muon pairs from decays of heavy resonances Υ and J/Ψ will show up in the very low invariant mass region, since $m_\Upsilon \sim 10\text{ GeV}$ and $m_{J/\Psi} \sim 3\text{ GeV}$. They can be rejected by the invariant mass requirement $M_{\mu\mu} > 20\text{GeV}$.

It follows from the requirement of three muons with at least one OS muon pair, that always a second OS muon pair is found. For SUSY events, two opposite sign muons originate from decays of the neutralino χ_2^0 with an additional muon from chargino χ_1^\pm decays. Hence, there is an ambiguity since two combinations of OS muon pairs can be built: the high $M_{\mu\mu}^{high}$ and low invariant mass combination $M_{\mu\mu}^{low}$. The high invariant mass combination moves the background events out of the signal region $M_{\mu\mu}[20, 86]\text{GeV}$ to higher invariant masses, but also the SUSY events. The low invariant mass combination is beneficial, moving all signal and background events to lower invariant masses away from the Z peak.

The core of the trimuon analysis is the identification of prompt muons and the rejection of fake muons. Thereafter the final trimuon event selection presented in Table 5.6 requires three tight muons with two OS muon pairs and the invariant mass of the low mass OS muon pair in the range between 20 GeV and 86 GeV.

Number of 'tight' muons	$N_\mu = 3$
Number of OS muon pairs	$N_{\mu^+\mu^-} = 2$
Low OS muon pair invariant mass	$20\text{ GeV} < M_{\mu\mu}^{low} < 86\text{ GeV}$

Table 5.6: Final event selection used in the trimuon analysis.

The final trimuon event selection results in $N_{SUSY} = 15.3 \pm 1.3$ (stat) events expected from SUSY at the reference point LM0 with the SM background of $N_{bkg} = 9.3 \pm 1.4$ (stat) events at $\mathcal{L}_{acc} = 200\text{ pb}^{-1}$. The results are shown in the last column of Table 5.5. The largest background contribution originates from the Z/γ^* +jets production, followed by the SM diboson processes and the $t\bar{t}$ production. The invariant mass distributions of all OS pairs and the lowest invariant mass pair after the trimuon selection are presented in Fig. 5.31.

For an accumulated luminosity $\mathcal{L}_{acc} = 200\text{ pb}^{-1}$ the result of the trimuon event selection for LM0 corresponds to a significance of $\sigma = 3.86$ calculated with the profile likelihood method of RooStatsCMS including 8.1% systematic uncertainties, which are discussed in

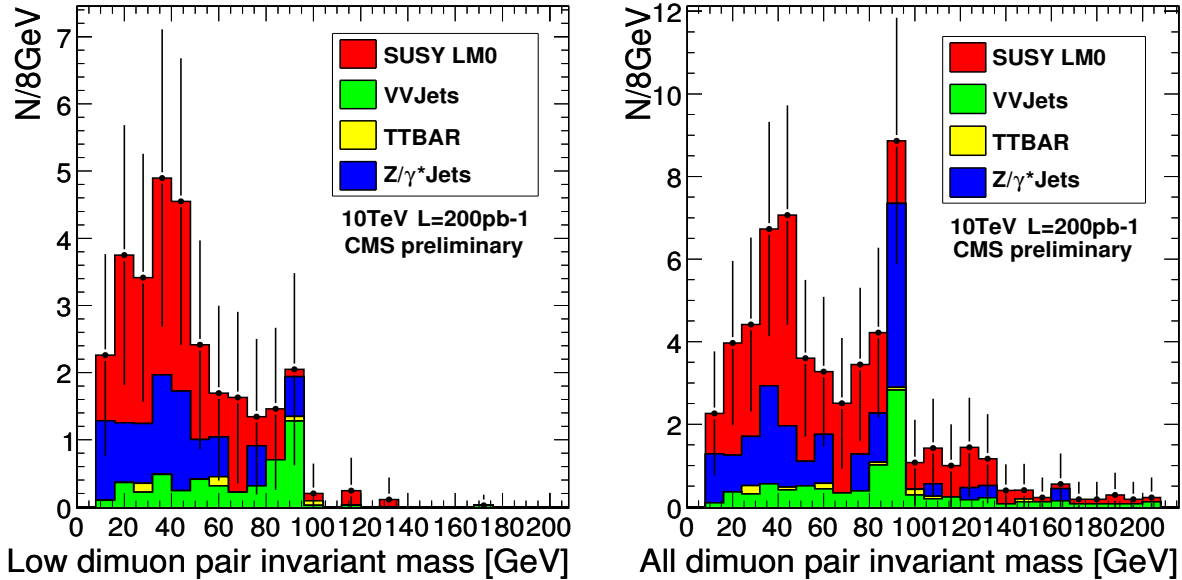


Figure 5.31: Invariant mass distribution of the lowest mass OS muon combination (L) and all OS combinations (R) after requiring 3 'tight' muons in SUSY (LM0) and SM backgrounds for a luminosity of $\mathcal{L}_{acc} = 200 \text{ pb}^{-1}$ at $\sqrt{s} = 10 \text{ TeV}$.

Section 5.7. The 5σ discovery for LM0 can be achieved with an accumulated luminosity of $\mathcal{L}_{acc} \sim 350 \text{ pb}^{-1}$.

The SUSY trimuon signature is produced by different SUSY processes. The gluino-gluino and squark-gluino production both contribute $\sim 45\%$ to the selected trimuon sample, whereas the direct neutralino-chargino production contributes only $\sim 10\%$. As already mentioned in Section 5.1.2, the trimuon events from gluino-gluino and squark-gluino production are expected to be produced with additional jets in the final state. The effect of a supplementary selection based on the jet properties, as well as on the missing transverse energy is reviewed in Section 5.10.

The large cross sections of QCD processes and the limited MC statistics of the considered samples lead to a high weighting factor per event. Therefore the suppression of the QCD processes has been checked with additional QCD samples. The statistics at different steps of selection is presented in Table 5.7 for an integrated luminosity of $\mathcal{L}_{acc} = 200 \text{ pb}^{-1}$.

Although already included in the considered QCD samples, the separate consideration of the bb +jets production offers the possibility to study the contribution to the trimuon selection with larger statistics. It has been shown that the majority of the QCD events with at least three loose muons are produced in bb +jets events.

The muon enriched QCD sample has a lower limit of $PT > 20 \text{ GeV}$ on the outgoing partons

	cs[pb]	$N_\mu \geq 3$ 'loose'	$N_\mu=1$ 'tight' $+\geq 2$ 'loose'	$N_\mu=2$ 'tight' $+\geq 1$ 'loose'	$N_\mu=3$ 'tight'
QCD ($b, c \rightarrow \mu$)	121 nb	5128.8 ± 151.7	130.1 ± 24.2	4.48 ± 4.48	0
QCD (bb +jets)	465 nb	2767.7 ± 366.1	0	0	0

Table 5.7: Statistics for the final selection of trimuon events for an integrated luminosity of $\mathcal{L}_{acc} = 200 \text{ pb}^{-1}$ cross checked with muon enriched QCD ($b, c \rightarrow \mu$) and bb +jets samples. The errors are given by the size of MC samples.

on the hard interaction and has been used to check the influence of the low PT bins. It is difficult to make a meaningful comparison, since the lack of the higher PT limit results in an overlap with the full QCD sample. In addition the long living mesons π^\pm and K^\pm have been forced to decay on generator level. Due to long mean live time of mesons a large part of the mesons will not decay but will be stopped in the hadronic calorimeter. Therefore the contribution of fake muons from long living mesons (π^\pm, K^\pm) is artificially enhanced. However the results support impressively the QCD rejection power of the final trimuon event selection.

5.6 Trigger

All events have been required to pass the high level triggers (HLT). The most suitable trigger streams for the trimuon signature are either the single muon Mu9 ($PT_\mu > 9 \text{ GeV}$) or the double muons DMu3 ($PT_\mu > 3 \text{ GeV}$). The selection efficiency for the SUSY LM points and SM backgrounds before and after offline selection is shown in Table 5.8 for these two trigger streams.

The streams population has been calculated as the number of events in the stream divided by the total number of events passing a HLT trigger for two different preselections. The numbers presented in the column 'inclusive' has been evaluated for all events in the used samples. The dimuon trigger stream has the advantage of having a smaller size ~ 10 in comparison with the single muon stream. The trigger efficiency for SUSY events with three prompt muons is shown in the column 'trimuon'. The single and dimuon trigger streams are efficient for all SUSY LM points. Due to the smaller size of the data sample, the double muon trigger stream has been chosen for the final selection of trimuon events.

5.7 Systematic Uncertainties

Although the presented analysis has attempted to search for SUSY using only muons and has avoided the selection on jets and missing transverse energy, the number of events after the final trimuon selection are sensitive to experimental and theoretical uncertainties.

channel	inclusive Mu9	inclusive DMu3	trimuon Mu9	trimuon DMu3
SUSY				
LM0	28.6	10.22	100	99.3
LM1	22.7	8.15	99.3	99.3
LM2	21.3	7.43	100	100
LM3	28.4	11.25	100	100
LM4	21.8	7.44	100	100
LM5	23.5	8.16	98.8	97.6
LM6	30.3	10.6	99.7	97.7
LM7	21.8	6.57	100	96.5
LM8	37.7	17.7	100	100
LM9	24.5	9.86	99.5	98.3
LM10	25.9	7.42	100	99.0
LM11	27.1	9.39	100	99.2
SM backgrounds				
$VV+\text{jets}(V=Z, W)$	42.1	10.1		
$Z \rightarrow \mu\mu$	59.1	36.5		
$Z \rightarrow \tau\tau$	6.9	0.1		
$t\bar{t}$	28.9	8.45		
$W+\text{jets}$	18.4	0.089		
QCD100to250	0.68	0.075		
QCD250to500	2.04	0.28		
QCD500to1000	4.17	0.74		
QCD1000toInf	7.31	1.88		

Table 5.8: Trigger efficiency [%] of single muon (Mu9) and double muon (DMu3) trigger streams before (left two columns) and after (right two columns) offline trimuon selection.

The anticipated experimental uncertainties include reconstruction uncertainties of the parameters used for the muon selection. On the one hand the tracker resolution affects the measurement of the momentum, the tracker isolation and the impact parameter significance of the muon. On the other hand the calorimeter energy scale uncertainties affect the measurement of the calorimeter isolation of the muon track. In order to evaluate the impact of the uncertainties, the parameters have been changed according to the anticipated uncertainties and the variation in the number of selected events $\Delta N/N$ has been counted. The isolation of the muon track in the tracker has been varied by the expected momentum resolution $\pm 2\%$ and in the calorimeter by the energy scale uncertainties $\pm 10\%$. The muon momentum has been changed in the range of the momentum measurement error $\pm \sigma_{PT}$. The systematic uncertainties of the impact parameter have been studied by Gaussian smearing of each impact parameter by σ_{dxy} . The summary of the anticipated instrumental uncertainties affecting the muon selection is presented in Table 5.9.

Theoretical uncertainties include uncertainties in the parton distribution functions (PDF) and uncertainties in the SM background cross section. The PDF uncertainties have been studied with the re-weighting technique using the LHPDF libraries and contribute $\sim 2\%$ [15]. The errors in the SM cross sections at $\sqrt{s} = 10$ TeV have been estimated by comparing the SM cross sections calculated with ALPGEN and SHERPA. For the Z +jets, W +jets, VV +jets and $t\bar{t}$ production the uncertainties in cross section are estimated to be below 5%. The luminosity uncertainties have been assumed as $\sim 5\%$.

Since no correlations between the different sources are assumed, the final systematic uncertainty has been calculated as $\sim 8.1\%$ by adding the evaluated uncertainties in quadrature. The considered uncertainties do not change the results significantly, especially since the SM backgrounds are experimentally determined from the sidebands using the ABCD method, as will be discussed in the next section. In this case the theoretical uncertainties are given by the data themselves and also a large fraction of the experimental uncertainties, like vertex uncertainties, is propagated from the sidebands to the signal region.

5.8 Data-Driven Background Estimation

The background decomposition after the trimuon selection is shown in Fig. 5.31, as obtained from MC-truth samples. But the real data collected by the CMS experiment does not show this truth. Therefore this study has attempted to estimate the background contribution from data. Two different approaches for two different kind of backgrounds have been developed and applied:

- The contribution of the diboson production (ZW, ZZ) with three prompt muons in the final state has been estimated from the Z -peak using a Monte Carlo correction factor to find the ratio of background events in the signal region and the Z -peak. This is called the Z -candle method and will be discussed in Section 5.8.2.

Observable	Source	Range	$\Delta N/N$
Tracker isolation	Tracker resolution	$\pm 2\%$	$\sim 0\%$
Calo isolation	Energy scale	$\pm 10\%$	1.6%
Muon PT	Tracker resolution	σ_{pt}	$\sim 0\%$
Tracker vertex $Sdxy$	Tracker resolution	σ_{dxy}	3.0%
SM cross section	theory		5 %
PDF	theory		2%
luminosity	detector		5%
Total syst. uncertainties			8.1%

Table 5.9: Summary of systematic uncertainties.

- However the largest background in the signal region comes from backgrounds with 2 prompt muons and a third muon originating from jets, preferentially from a heavy quark. As mentioned mentioned before, this one cannot be reliably estimated by Monte Carlo simulations, because of the uncertainty in the heavy quark production. Therefore one should try to estimate this background from the data itself. This is done by a so called ABCD method by extrapolating the fake muons in the sidebands of the isolation and impact parameter distributions to the signal region, as described in the following section.

5.8.1 ABCD Method

The ABCD method [109] has attempted to estimate the backgrounds with 2 prompt muons and a third muon originating from jets. Since the background has 2 prompt and 1 fake muon, one can select a data sample with 2 'tight' muons fulfilling the isolation and $Sdxy$ requirement and one muon with a good track quality but not accepted by the isolation and $Sdxy$ requirement ('non-accepted'), i.e. $iso > 0.15$ or $Sdxy > 4$ and with one low mass muon pair in the range $20 < M_{\mu\mu} < 86$ GeV.

The sample is now dominated by the background from $Z/\gamma^* + \text{jets}$ and $t\bar{t}$, as expected by allowing the third muon to be 'loose' (see Fig. 5.30). The ABCD method tries to extrapolate the number of trimuon events with 2 'tight' muons and 1 'non-accepted' muon towards the signal region, i.e. events with 3 'tight' muons. The ABCD procedure was used in the following way: the iso and $Sdxy$ parameters of the 'non-accepted' muon were entered into a 2-D scatter plot of these variables. By definition these tracks cannot enter into the signal region with ($iso \leq 0.15$ and $Sdxy \leq 4$), since in this case they would not be selected as 'non-accepted'. So these tracks occupy the sidebands of the signal region. Since the data sample was selected to have 2 'tight' and 1 'non-accepted' muon, every 'non-accepted' muon entry corresponds to one event.

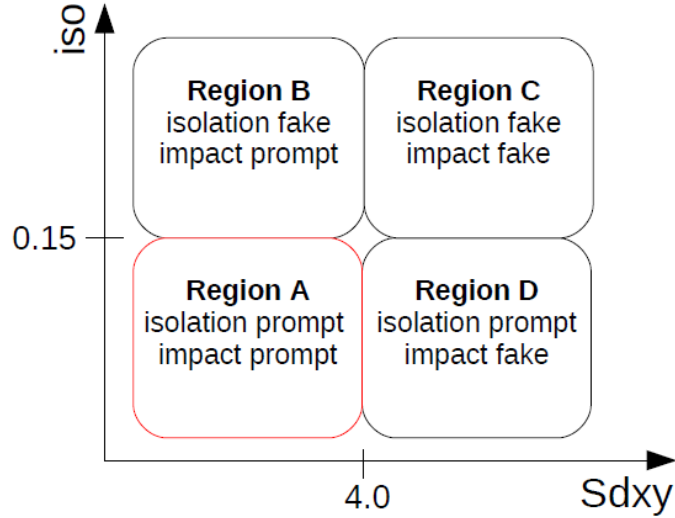


Figure 5.32: Sketch of the different regions used for the ABCD method, where region A corresponds to the signal region, and region B, C and D are the sidebands used for prediction of fake background events in region A.

This scatter plot was divided into 4 different regions, called A, B, C and D (see Fig. 5.32).

- Region A is the signal region and contains events with 3 'tight' muons, i.e. $iso \leq 0.15$ and $Sdxy \leq 4$.
- In region B the third muon is non-isolated but passing the $Sdxy$ selection, so $iso > 0.15$ and $Sdxy \leq 4$.
- In region D the third muon is isolated, but is not accepted the $Sdxy$ requirement, so $iso \leq 0.15$ and $Sdxy > 4$.
- In region C the third muon is non-isolated and does not pass the $Sdxy$ cut, so $iso > 0.15$ and $Sdxy > 4$.

The SUSY signal and the irreducible diboson background are predominantly populating region A. Region C is populated with the major part of the fake backgrounds. The regions B, C and D can be used as control regions, since they are mostly populated by the background.

Assuming only background in regions A, B, C and D the number of background events in

the different regions N_A , N_B , N_C and N_D can be obtained as

$$N_A = \int_0^{x_0} dx \int_0^{y_0} dy \rho(x, y) \quad (5.23)$$

$$N_B = \int_0^{x_0} dx \int_{y_0}^{\infty} dy \rho(x, y) \quad (5.24)$$

$$N_C = \int_{x_0}^{\infty} dx \int_{y_0}^{\infty} dy \rho(x, y) \quad (5.25)$$

$$N_D = \int_{x_0}^{\infty} dx \int_0^{y_0} dy \rho(x, y) \quad (5.26)$$

where x and y represents the $Sdxy$ and iso parameter, respectively. $\rho(x, y)$ is the probability density function of the background distribution as a function of x and y . If the variables x and y are uncorrelated, the probability function can be factorized as

$$\rho(x, y) = f(x) \cdot g(y) \quad , \quad (5.27)$$

where $f(x)$ and $g(y)$ are functions that depend only on x and y , respectively. Hence, if the data can be factorized in the selected parameters i.e. the parameters have no correlations, the ratio of the number of background events in the various regions fulfills the proportionality

$$N_A/N_B = N_D/N_C \quad . \quad (5.28)$$

If this relation is valid, the number of background events in region A can be determined by measuring the number of events in region B, C and D.

Such a relation can be compromised by intrinsic correlations between the variables and/or detector effects. E.g. region D with a large impact parameter $Sdxy$ and a low iso parameter can be generated by a slightly misaligned sector of the tracker.

The use of the selected trimuon sample is limited by relatively small statistics and contaminations coming from prompt (diboson) and fake muons from SUSY signal. On the other hand the QCD reference sample is almost free from the contamination and will provide large statistics of fake muons. So if the isolation and vertex parameters are not correlated for the fake muons, as expected for a perfect detector, a QCD sample is perfect for checking both, the intrinsic uncertainties from the method and possible biases from the detector, discussed above.

ABCD Method with the Fake Reference Sample

With the selected fake reference sample, the performance of the ABCD method can be checked by comparing the observed number of fake muons in region A, called N_A^{obs} , with

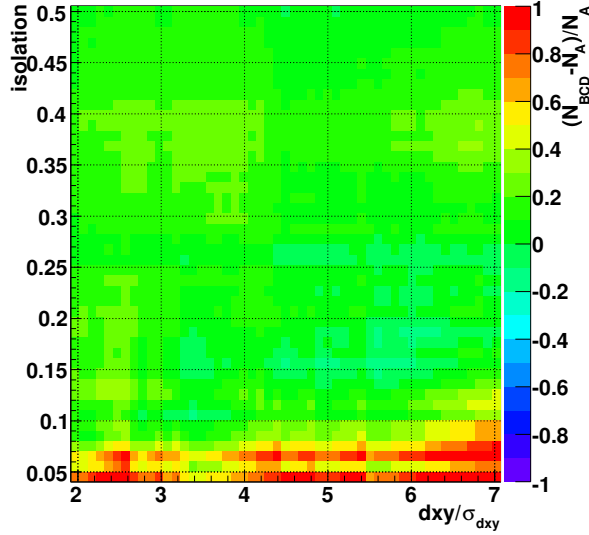


Figure 5.33: $R_{QCD} = (N_{BCD}^{\text{obs}} - N_A^{\text{obs}})/N_A^{\text{obs}}$ in the isolation- $Sdxy$ plane obtained from the selected fake reference sample as a variation of the region boundaries shown in Fig. 5.32. The size of the regions is defined by the value of the $Sdxy$ and iso cut, which is plotted on x and y axis, respectively, i.e. for the used selection cut in the trimuon event selection the ratio R_{QCD} is shown at $Sdxy = 4$ and $iso = 0.15$.

the predicted number of fake muons in region A from the extrapolation of the observed number of fake muons in the sidebands N_B^{obs} , N_C^{obs} and N_D^{obs} as

$$N_{BCD}^{\text{obs}} \equiv N_B^{\text{obs}} N_D^{\text{obs}} / N_C^{\text{obs}} \quad . \quad (5.29)$$

The difference of the predicted and the observed number of fake muons in region A can be calculated as

$$(N_{BCD}^{\text{obs}} - N_A^{\text{obs}}) \quad . \quad (5.30)$$

The ratio of this difference to the observed number of fake muons in region A

$$R_{QCD} = (N_{BCD}^{\text{obs}} - N_A^{\text{obs}})/N_A^{\text{obs}} \quad (5.31)$$

is shown in Fig. 5.33. Here the boundaries of the regions are defined by the axis, so for ($iso = 0.15$, $Sdxy = 4$) region A is defined by ($iso \leq 0.15$ and $Sdxy \leq 4$), region D is defined by ($iso > 0.15$ and $Sdxy > 4$) and the regions B and C are in between. One observes that the linearity for the high statistics QCD sample holds over the whole range with reasonable accuracy, independent of the choice of the region boundaries.

For such a QCD sample one does not expect any contribution from new physics, given the large QCD cross section. Thus one can assume that also in the data the ratio R_{QCD} should be close to zero for a perfectly aligned detector, so uncertainties from detector

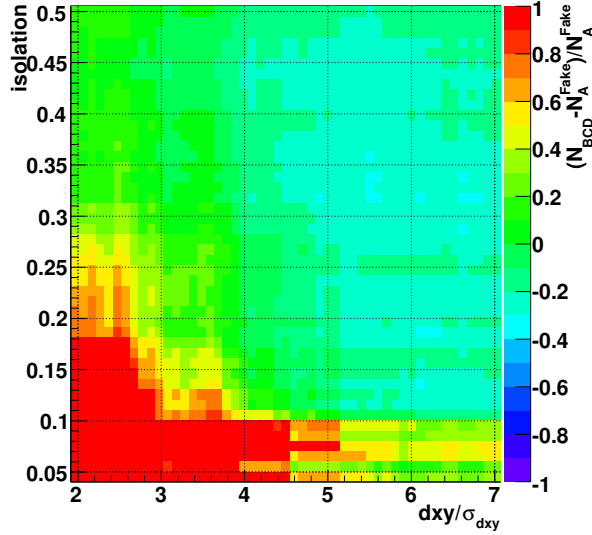


Figure 5.34: $R_{\text{Bkg}} = (N_{BCD}^{\text{MC}} - N_A^{\text{Fake}})/N_A^{\text{Fake}}$ in the isolation- $Sdxy$ plane for the selected background in the trimuon analysis as a variation of the region boundaries shown in Fig. 5.32.

correlations leading to systematic effects in the ABCD method can be quickly spotted. However the physical background in the signal region is mainly coming from $Z/\gamma^* + \text{jets}$ and $t\bar{t}$ events. The only possibility to check the ABCD method for these backgrounds is to rely on Monte Carlo simulation or one argues that fakes from QCD and other backgrounds have similar correlations, as suggested by the similarity of the isolation and impact parameter distributions, shown in Fig. 5.26 before.

ABCD Method for the Trimuon Event Selection

The validity of the ABCD method for the data-driven estimation of the background events with fake muons after the trimuon selection has been checked at MC level. This has been done by calculating the predicted background in region A

$$N_{BCD}^{\text{MC}} \equiv N_B^{\text{MC}} N_D^{\text{MC}} / N_C^{\text{MC}} \quad . \quad (5.32)$$

where N_B , N_C and N_D are the number of MC events in region B, C and D, respectively. The MC-truth value of the number of fake events in region A is obtained as

$$N_A^{\text{Fake}} \equiv N_A^{\text{QCD}} + N_A^{\text{Wjets}} + N_A^{\text{Zjets}} + N_A^{\text{tt}} \quad . \quad (5.33)$$

Again like for the fake reference sample, the performance of the ABCD method can be checked by comparing the number of predicted events with the MC-truth value of fake background events in region A by building the ratio

$$R_{\text{Bkg}} = (N_{BCD}^{\text{MC}} - N_A^{\text{Fake}})/N_A^{\text{Fake}} \quad . \quad (5.34)$$

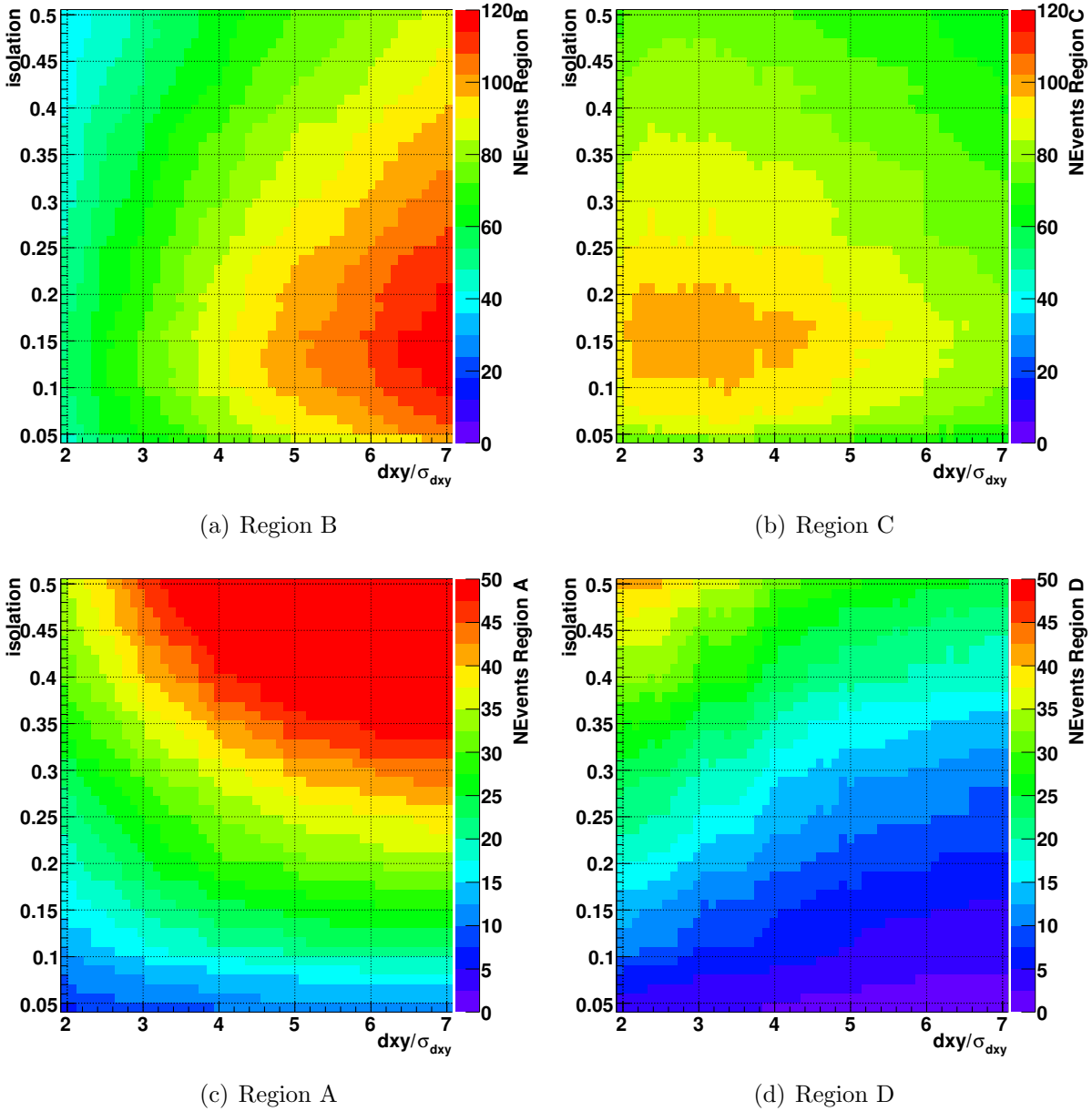


Figure 5.35: Number of events for SUSY signal plus SM backgrounds in the regions A, B, C, D for the trimuon analysis for a luminosity of $\mathcal{L}_{acc} = 200 \text{ pb}^{-1}$ as a variation of the region boundaries shown in Fig. 5.32.

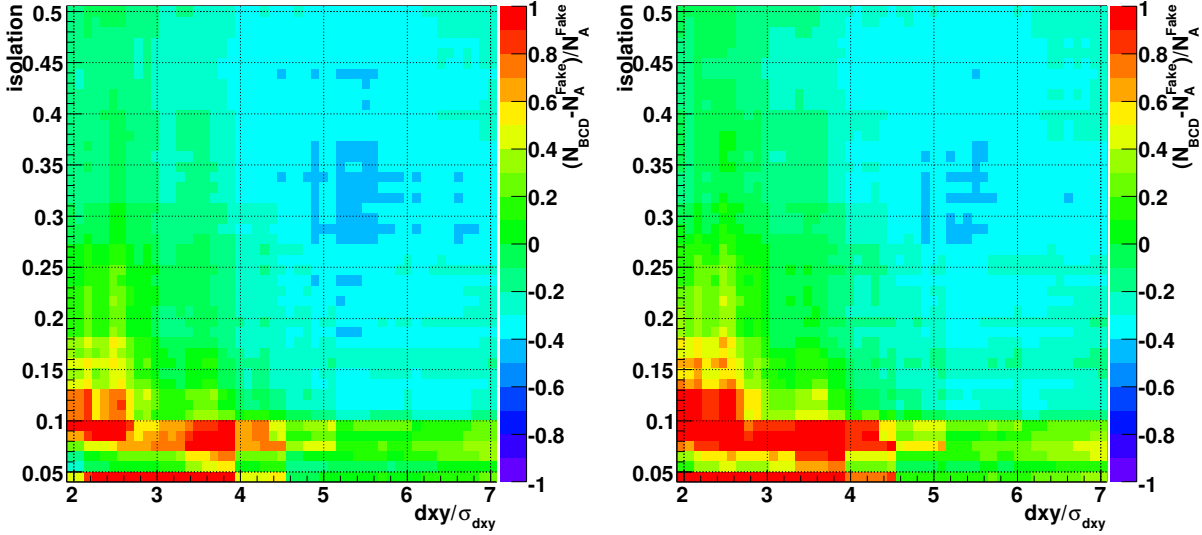


Figure 5.36: MC study of $R_{Bkg} = (N_{BCD}^{MC} - N_A^{Fake})/N_A^{Fake}$ in the isolation- $Sdxy$ plane as a variation of the region boundaries shown in Fig. 5.32 with only SM diboson production and fake backgrounds (L) in the B, C, and D region, but no SUSY signal and with only fake backgrounds (R) in the B, C, and D regions, but no SUSY signal or SM diboson production.

This has been done in Fig. 5.34 by using all data in the sidebands, i.e. contributions from SUSY signal, SM diboson production and all background processes with fake muons and plotting R_{Bkg} , again by varying the boundaries as for R_{QCD} . One observes a slight overestimation of about $\sim 10\%$ in the region of the cuts chosen, which leads to a conservative limit. However, the statistical errors are still in the order of 30% for the cuts in this region, as can be observed from the event numbers in the various regions in Fig. 5.35.

Additionally, the performance of the ABCD method has been checked without the presence of SUSY events i.e. using only contributions from SM diboson production and fake background processes in the sidebands. Without SUSY contribution, one observes a slight underestimation of about $\sim 10\%$ in the region of the cuts chosen. Fig. 5.36 shows the corresponding ratio R_{Bkg} , as well as the ratio obtained by using only fake background processes in the sidebands.

Although the statistical error is large, the tendency of overestimation or underestimation, respectively, in the region of the chosen cuts corresponds to a deviation from the perfect validity of the ABCD method. This 10% are taken as a systematic uncertainties of the method and they are added to the instrumental and theoretical systematic uncertainties discussed in the previous section.

The prediction with the ABCD method of the fake background events after the final trimuon event selection result in

$$N_{ABCD} = 6.8 \pm 2.6 \text{ (stat)} \pm 0.87 \text{ (sys)} \text{ events} \quad , \quad (5.35)$$

where the *stat*-error is the propagated statistical error from the sidebands. This number has to be compared with 6.5 ± 2.4 fake backgrounds events, as shown in Table 5.5. Without SUSY events in the sidebands the fake background contribution is estimated as

$$N_{ABCD} = 5.8 \pm 2.4 \text{ (stat)} \pm 0.74 \text{ (sys)} \text{ events} \quad , \quad (5.36)$$

which still agrees pretty well within the statistical error.

5.8.2 Z-Candle Method

The ZW and ZZ diboson production with leptonic decay of both bosons to muons has a similar topology as the SUSY signal and can be used as a control measurement for the trimuon SUSY search. The observation of the Z -peak (Z -candle) in the selected trimuon events can be used to calibrate the selection efficiency. On the other hand this channel is also an important background, especially with the off-shell Z boson and γ^* muonic decays.

The contribution of this background into the selected sample can be estimated from the events in the $M_{\mu\mu} = M_Z[86, 96]$ GeV invariant mass range, mostly populated by diboson events, as it can be seen in the plot of the lowest mass OS muon combination in Figure 5.31. The number of events in the signal region $M[20, 86]$ GeV can be calculated from the number of events in the Z -peak by

$$N_{\text{sig}} = N_{M[86,96]} \cdot R_{\text{MC}} \quad , \quad (5.37)$$

where R_{MC} is the MC correction factor, which can be calculated from the invariant mass distribution of the low mass OS muon pair of the MC-truth ZW and ZZ production as

$$R_{\text{MC}} = N_{M[20,86]} / N_{M[86,96]} \quad . \quad (5.38)$$

For this purpose the VV +jets sample has been preselected with three prompt muons ($PT \geq 8$ GeV and $|\eta| \leq 2.1$) on MC level. The corresponding invariant mass distribution is shown in Fig. 5.37. The ratio R_{MC} without detector simulation, trigger requirement has been calculated as

$$R_{\text{MC}} = 1.72 \pm 0.14 \text{ (stat)} \pm 0.03 \text{ (sys)} \quad , \quad (5.39)$$

where the statistical error corresponds to the size of the MC sample. The ratio R_{MC} evaluated with detector simulation, trigger requirement and final muon selection result in $R_{\text{MC}} = 1.75 \pm 0.25 \text{ (stat)}$. Due to the smaller statistical uncertainties, the previous value has been used. The systematic error corresponds to the theoretical uncertainties obtained

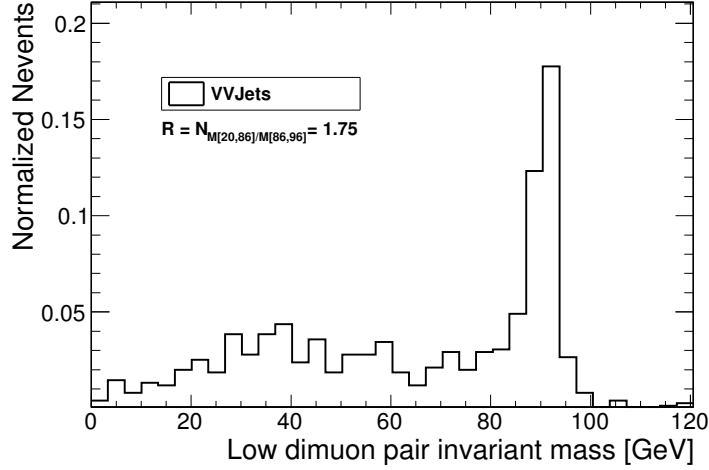


Figure 5.37: Low mass OS muon invariant mass distribution of the VV +jets sample used for the calculation of the MC correction factor $R = N_{M[20,86]}/N_{M[86,96]}$ of the Z -candle method.

by comparing cross section predictions from ALPGEN and SHERPA.

As for the ABCD method, such an estimation suffers from contaminations coming from SUSY and SM background with fake muons (Z +jets and $t\bar{t}$), see Figure 5.31. The estimation of the diboson background contribution using the Z -candle method with SUSY contamination in the Z -peak result in

$$N_{Z\text{-candle}} = 4.0 \pm 2.7 \text{ (stat)} \pm 0.32 \text{ (sys)} \text{ events} \quad (5.40)$$

in the low mass invariant mass range $M[20,86]$ GeV at $\mathcal{L}_{acc} = 200 \text{ pb}^{-1}$. The error is the statistical error which has been propagated from of the number of events in the Z -candle to the signal region with the statistical uncertainties of the MC correction factor. This number has to be compared with 2.8 ± 0.3 diboson background events, as shown in Table 5.5. The assumed systematic uncertainties include the systematic uncertainties considered in the previous section and the systematic uncertainties on the MC correction factor.

The Z -candle method without SUSY signal contamination in the Z -peak predicts

$$N_{Z\text{-candle}} = 3.8 \pm 2.6 \text{ (stat)} \pm 0.31 \text{ (sys)} \text{ events} \quad . \quad (5.41)$$

5.8.3 Summary

The SM background estimation from the data-driven methods yields for low mass pairs

$$N_{Bkg}^{DD} = 10.8 \pm 3.7 \text{ (stat)} \pm 0.9 \text{ (sys)} \text{ events} \quad , \quad (5.42)$$

	incl. SUSY	no SUSY
	N \pm stat \pm sys	N \pm stat \pm sys
$N_{\text{Bkg}}^{Z\text{-candle}}$	$4.0 \pm 2.7 \pm 0.32$	$3.8 \pm 2.6 \pm 0.31$
$N_{\text{Bkg}}^{\text{ABCD}}$	$6.8 \pm 2.6 \pm 0.87$	$5.8 \pm 2.4 \pm 0.74$
$N_{\text{Bkg}}^{\text{DD}}$	$10.8 \pm 3.7 \pm 0.93$	$9.6 \pm 3.5 \pm 0.80$

Table 5.10: Background contributions from diboson production, as estimated with the Z -candle method and from events with fake muons, as estimated with the ABCD method, both with and without a SUSY signal in the control regions.

	low mass OS muons $M[20,86]\text{GeV}$
NSignal(LM0)	15.3 ± 3.9 (stat) ± 1.2 (sys)
NBkgMCTruth	9.3 ± 3.0 (stat) ± 0.8 (sys)
NBkgDD total	10.8 ± 3.7 (stat) ± 0.9 (sys)

Table 5.11: Summary of data-driven (DD) estimation of SM backgrounds for an integrated luminosity of $\mathcal{L}_{acc} = 200 \text{ pb}^{-1}$.

to be compared with 9.3 ± 3.0 (stat) ± 0.8 (sys) events obtained from the event selection based on the MC-truth information, see Table 5.5. Without the presence of SUSY the SM background estimation results in

$$N_{\text{Bkg}}^{\text{DD}} = 9.6 \pm 3.5 \text{ (stat)} \pm 0.8 \text{ (sys)} \text{ events} \quad . \quad (5.43)$$

The summary of the contribution of the two complementary data-driven methods for the estimation of fake and prompt background events is given in Table 5.10, both in case a SUSY signal would be present in the control regions and without SUSY.

The signal, ZW and ZZ contamination in the sidebands and the double counting result in an overestimate of the background but no correction for this was applied in order to obtain completely data-driven conservative limits for the discovery reach. The summary of the data-driven background estimation is shown in Table 5.11.

5.9 Discovery Reach

In order to compare the discovery reach of the trimuon search at the LHC with the exclusion limits obtained with the searches for trileptons at the Tevatron, the mSUGRA parameters $\tan\beta = 3$, $A_0 = 0$ and $\mu > 0$ were chosen. Then the m_0 - $m_{1/2}$ plane in the range $m_0 = [0, 300] \text{ GeV}$ and $m_{1/2} = [150, 300] \text{ GeV}$ was divided into 450 points, corresponding to steps of $\Delta_{m_0, m_{1/2}} = 10 \text{ GeV}$, and 10000 events for each point were simulated with the fast simulation of the CMS detector, which has been validated to agree with the full simulation. Thereafter the number of expected SUSY signal events were selected with

the final trimuon event selection. For the SM backgrounds the data-driven estimation has been used, which was introduced in the last section. The data-driven estimation suffers from the contribution of SUSY events in the sidebands increasing the predicted background by 1.2 events at LM0, as shown in Table 5.10. Since the influence of SUSY events depends on the SUSY cross section, for each mSUGRA point with cross section σ this number has been weighted with the factor $\sigma/\sigma_{\text{LM0}}$. The significance for each point has been calculated with the RooStatsCMS package using the profile likelihood method as described in Section 4.4.

The discovery reach has been evaluated with the leading order (LO) calculation of the cross section for the SUSY signal and SM backgrounds. The k -factor, which is defined as the cross section ratio of LO to next-to-leading-order (NLO) calculations, $k = \sigma_{\text{NLO}}/\sigma_{\text{LO}}$, is large for SUSY production, where $k(\tilde{g}\tilde{g}) \sim 1.7$, $k(\tilde{g}\tilde{q}) \sim 1.2$ and $k(\tilde{q}\tilde{q}) \sim 1.3$ in the low SUSY mass region [98, 99]. The influence of the NLO calculations on the SM background processes have been evaluated with MC@NLO [110]. For the main SM background processes of the trimuon search, which are the Z/γ^* +jets and VV +jets production, the k -factors are moderate ($k \sim 1.16$). The NLO calculations have a large influence on the cross section of the $t\bar{t}$ production ($k \sim 1.7$). However, the contribution to the total SM background after the final trimuon event selection is only $\sim 3\%$. Since the NLO corrections would enhance the SUSY signal by 48% and the SM backgrounds by only 18%, the LO cross sections have been used in order to obtain a conservative estimation of the discovery reach.

Fig. 5.38 shows the discovery reach of the trimuon SUSY search for an accumulated luminosity of $\mathcal{L}_{\text{acc}} = 200(500) \text{ pb}^{-1}$ at $\sqrt{s} = 10 \text{ TeV}$ calculated with the data-driven estimation of the SM backgrounds. The shape of the discovery reach is driven by the relation of gaugino and slepton masses throughout the plane and shows three regions corresponding to different gaugino decay modes:

- The white corridor starting at $m_0 = 70 \text{ GeV}$ in Fig. 5.38 represents the transition region between two-body decays $\chi_2^0 \rightarrow \tilde{\mu}\mu$ and three-body decays $\chi_2^0 \rightarrow \mu\mu\chi_1^0$. The smuon mass increases with m_0 , so three-body decays are on the right side of the corridor. At the transition region, where the mass of the smuon and the neutralino are similar, the muons are too soft for efficient detection (see Fig. 5.8), so this region is not excluded.
- To the right the branching ratio to muons via three-body decays decreases from $\sim 20\%$ to $\sim 3\%$ at large m_0 (see Fig. 5.39), which is the expected value for three-body decays mediated via a virtual Z boson. In between the branching ratio becomes slightly below 3%, which can happen due to interference of different diagrams contributing to the same final state (see Fig. 5.5).
- To the left, where the slepton mass decreases and two-body decays take place, the branching ratio becomes $\sim 30\%$. At smaller m_0 the branching ratio decreases, since

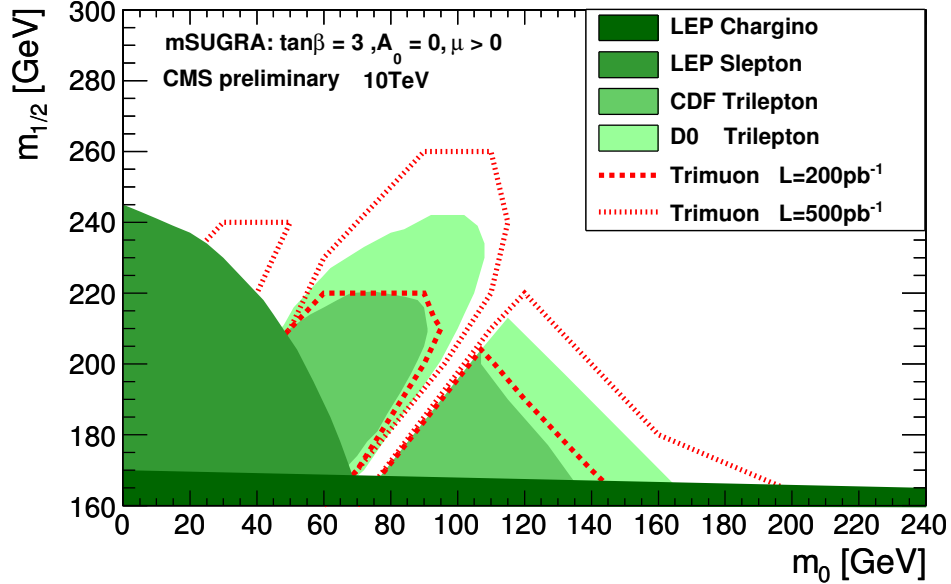


Figure 5.38: The SUSY trimuon 5σ discovery reach for a collected luminosity of $\mathcal{L}_{acc} = 200(500) \text{ pb}^{-1}$ at $\sqrt{s} = 10 \text{ TeV}$ (mSUGRA: $\tan\beta = 3$, $A_0 = 0$, $\mu > 0$).

here sneutrinos become lighter than the neutralino and two body decays $\chi_2^0 \rightarrow \tilde{\nu}\nu$ open up, thus leading to smaller branching ratio to muon final states (see Fig. 5.8). In the second transition region at $m_0 \sim 40 \text{ GeV}$, the small mass difference between sneutrino and chargino in the decay $\chi_1^\pm \rightarrow \tilde{\nu}l$ leads to a reduced selection efficiency of the muon.

5.9.1 Comparison with Tevatron Results

The trimuon search at the LHC allows to probe the low mass mSUGRA region already in the first year of LHC running with $\sqrt{s} = 10 \text{ TeV}$ and reach a similar sensitivity as the Tevatron experiments, where the SUSY trilepton signature has been intensively searched for at $\sqrt{s} = 1.96 \text{ TeV}$. Since here protons are collided with antiprotons, energetic antiquarks are present, the direct gaugino production is the dominant SUSY production channel. Therefore SUSY trilepton events are dominantly produced in direct production of neutralino-chargino pairs.

The latest results of the search for trileptons from neutralino-chargino pair production at the Tevatron are consistent with the Standard Model prediction, but regions in the m_0 - $m_{1/2}$ plane within the reference model of mSUGRA have been excluded. For reason of comparison the exclusion limits from D0 and CDF are also shown in Fig. 5.38. The analyses can be briefly summarized as follows:

- The CDF collaboration analyzed data corresponding to an integrated luminosity

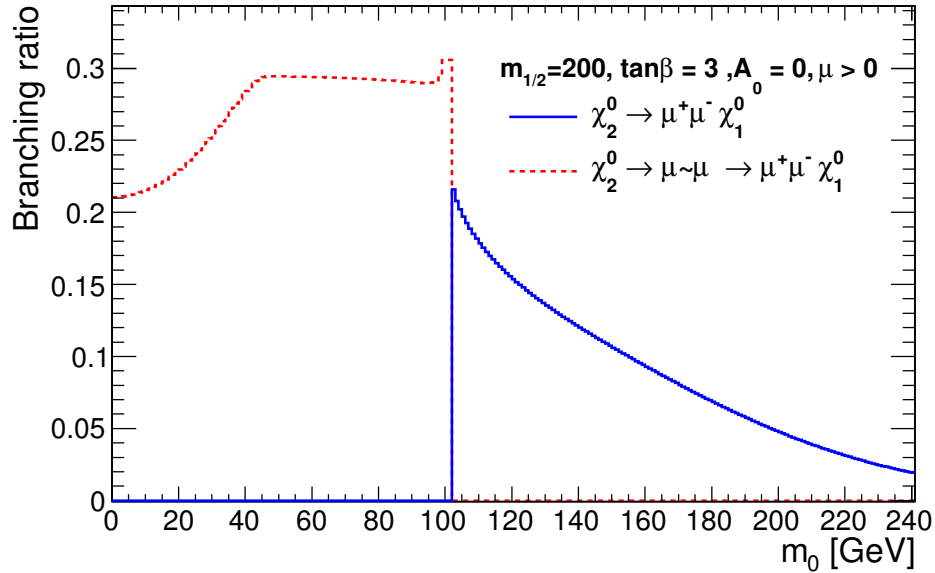


Figure 5.39: Branching ratio of neutralino decays to muons as a function of m_0 for $m_{1/2} = 200$ GeV, $\tan\beta = 3$, $A_0 = 0$, $\mu > 0$.

of $\mathcal{L}_{acc} = 2.0 \text{ fb}^{-1}$. In addition to muon and electron final states, also isolated tracks have been considered, but restricting the objects to the central part of the CDF detector defined by pseudorapidity $|\eta| < 1.1$. Furthermore, the characteristic topology of the direct gaugino pair production was taken into account by allowing no more than one jet with $ET > 15$ GeV and $|\eta| < 2.5$ and requiring $\text{MET} > 20$ GeV. The exclusion limit has been obtained by combining the results from four individual trilepton final states defined by the quality of the three leptons [13].

- The trilepton search with the D0 experiment used data corresponding to an integrated luminosity of $\mathcal{L}_{acc} = 2.3 \text{ fb}^{-1}$. Four dedicated trilepton event selections have been applied by combining muon, electron and τ final states with a selection based on jets and MET. In comparison with CDF a larger exclusion limit has been obtained mainly because of the larger accumulated luminosity and the acceptance of physics objects, since muons, electrons and τ 's have been accepted in a range of $|\eta| < 2.0$, $|\eta| < 3.2$ and $|\eta| < 2.5$, respectively [14].

5.10 Prospects of an Extended Selection

The presented trimuon analysis has attempted to select SUSY using only muons, all other observables, including missing energy and jets have been avoided in order to reduce the systematic uncertainties of the search. However, since the SM background can be further rejected with an additional selection on jets and MET, this section discusses the prospects

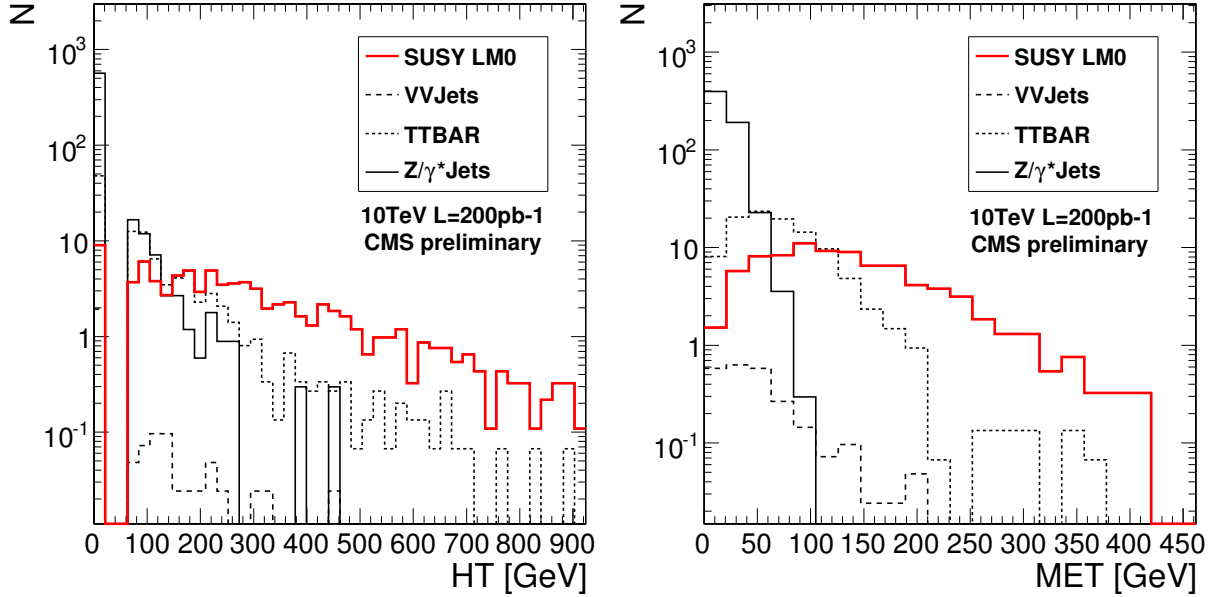


Figure 5.40: The HT (R) and MET (L) distribution for SUSY signal at LM0 and SM backgrounds after the selection of two tight and at least one quality muon for a luminosity of $\mathcal{L}_{acc} = 200 \text{ pb}^{-1}$.

	Trimuon	$HT > 100 \text{ GeV}$	$MET > 50 \text{ GeV}$
LM0	15.3 ± 1.3	11.3 ± 1.1	10.0 ± 1.0
$VV+\text{jets}$	2.8 ± 0.3	0.28 ± 0.08	0.17 ± 0.06
$Z/\gamma^*+\text{jets}$	6.2 ± 1.4	0	0
$t\bar{t}$	0.3 ± 0.1	0.07 ± 0.07	0
ΣSM	9.3 ± 1.4	0.35 ± 0.11	0.17 ± 0.06

Table 5.12: Statistics for the extended trimuon selection for an integrated luminosity of $\mathcal{L}_{acc} = 200 \text{ pb}^{-1}$. The errors are given by the size of MC samples.

of an extended trimuon event selection.

At LHC the SUSY trimuon signature is dominantly produced in gluino and squark cascade decays, leading to events with large jet multiplicity and high energetic jets. The HT parameter calculated as the sum of ET of all jets

$$HT = \sum_{jet} ET_{jet} \quad (5.44)$$

has been found as the best discriminating observable for further reduction of the SM background processes after ranking of the parameters N_{jet} , ET_{jet1} , ET_{jet2} , ET_{jet3} and MET

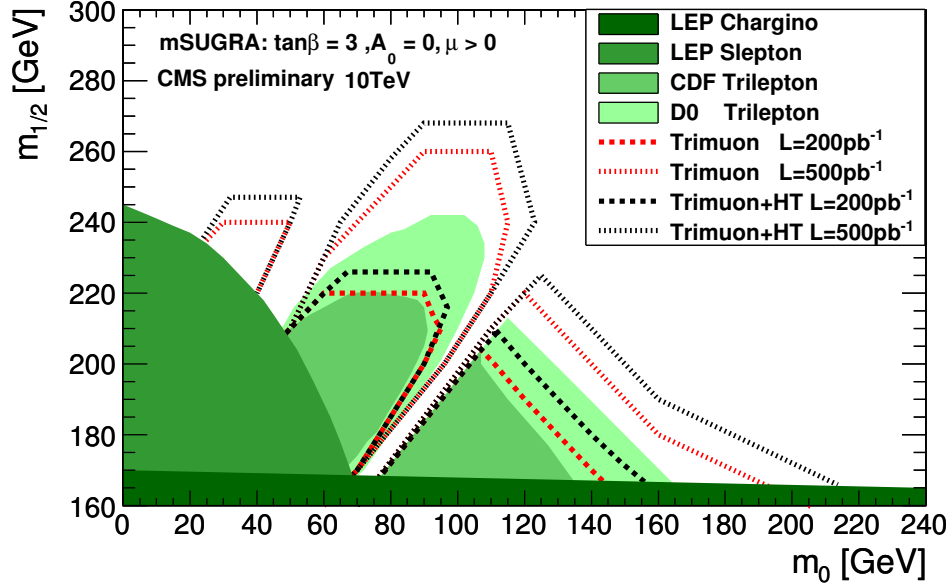


Figure 5.41: The SUSY trimuon 5σ discovery reach with an additional selection $HT > 100$ GeV for a collected luminosity of $\mathcal{L}_{acc} = 200(500)$ pb^{-1} at $\sqrt{s} = 10$ TeV (mSUGRA: $\tan\beta = 3$, $A_0 = 0$, $\mu > 0$).

with the Genetic Algorithm. The jets have been reconstructed with the iterative cone algorithm using a cone size $\Delta R < 0.5$ and corrected using MC jet energy corrections. The MET is based on the calorimeter information and is corrected for muon energy deposition and the jet energy scale.

Fig. 5.40 shows the corresponding HT distribution of SUSY signal at LM0 and SM background processes after the requirement of two tight muons and at least one quality muon. The optimization of the HT selection cut at LM0 results in $HT > 100$ GeV counting all jets with $ET > 70$ GeV and the jet axis within $|\eta| < 3$.

The final trimuon selection with the additional HT requirement results in 11.3 ± 1.1 SUSY signal and 0.35 ± 0.11 SM background events for an accumulated luminosity of $\mathcal{L}_{acc} = 200$ pb^{-1} . The results of the selection are shown in Table 5.12.

The HT selection is prone to jet energy scale uncertainties assumed as 10% in the first year of LHC running. In order to evaluate the impact of the uncertainties, the jet energy has been changed according to the anticipated uncertainties and the variations in the number of selected events $\Delta N/N$ was counted. The impact of the jet energy scale uncertainties is 33%, resulting in a total systematic uncertainty of 34% by including the systematic uncertainties considered in Table 5.9 and adding them in quadrature.

For an accumulated luminosity of $\mathcal{L}_{acc} = 200$ pb^{-1} the significance at LM0 increases to

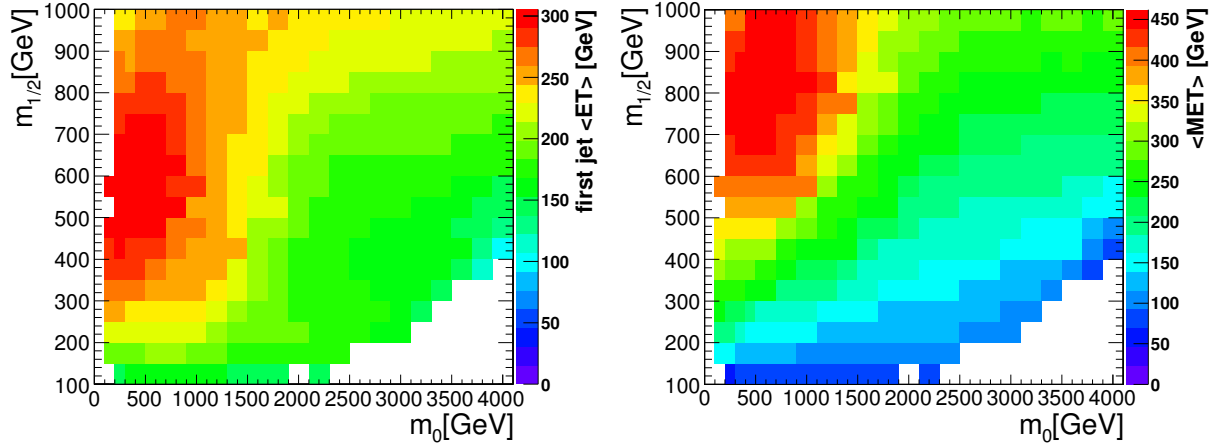


Figure 5.42: SUSY model dependence of the average ET of the first jet (L) and the missing transverse energy (R) in the mSUGRA m_0 - $m_{1/2}$ plane for $\tan\beta=50$, $A_0 = 0$, $\mu > 0$ and $\sqrt{s} = 14$ TeV collision energy.

$\sigma = 7.3$ as calculated with the profile likelihood method including systematic uncertainties. Figure 5.41 shows the improved discovery reach of the trimuon+ HT selection in the m_0 - $m_{1/2}$ plane for $\tan\beta = 3$, $A_0 = 0$ and $\mu > 0$.

However, a selection based on jets would essentially require dedicated data-driven methods to control and understand the HT distribution of the VV +jets, Z +jets and $t\bar{t}$ production in order to minimize the experimental and theoretical uncertainties of the corresponding jet distributions, which is out of the scope of this document.

In addition the selection has been optimized taking into account the HT and MET parameter, resulting in the same HT selection cut and in $MET > 50$ GeV. The results are shown in the last column of Table 5.12. The MET variable is a difficult object to understand, prone to large systematic uncertainties and a long dedicated study will be necessary to turn it into a useful physics analysis variable [91]. In addition the significance improves only to $\sigma = 7.7$ without considering systematic uncertainties on the missing transverse energy. Hence the best selection for further SM background rejection remains the additional HT requirement.

SUSY Model Dependence

Furthermore, the average jet energy in SUSY events depends on the chosen SUSY model. Figure 5.42 shows the SUSY model dependence of the average jet ET in the m_0 - $m_{1/2}$ plane for $\tan\beta = 50$ at $\sqrt{s} = 14$ TeV collision energy. The difference is mostly related to the mass spectrum of particles participating in the cascade decays: the larger the mass difference, the larger the energy of jets. In the region with large jet ET at around $m_0 \sim 500$ GeV and $m_{1/2} \sim 800$ GeV both squark and gluino masses are in the order of 1.5 TeV and

the gauginos are comparable light $m_{\chi_1^0} \sim 300$ GeV, $m_{\chi_2^0} \sim m_{\chi_1^\pm} \sim 600$ GeV, leading to high energetic quarks produced in squark and gluino decays to quarks and gauginos. In the region near the electroweak symmetry breaking constrain at large m_0 , the squarks are heavy (~ 2 TeV) and gluinos are heavier than the gauginos, which are all in the same mass range. Consequently the gaugino production carries most of the SUSY cross section and quarks produced in decays of heavier gauginos to lighter gauginos are rather soft. The same behavior is observed for the missing transverse energy of the SUSY events mostly caused by the lightest neutralinos, which are produced at the end of each SUSY particle cascade: the smaller the energy of the LSP, the smaller the missing transverse energy.

Chapter 6

Conclusion

As mentioned in the introduction, the trimuon signature originating from decays of neutralinos and charginos has only a small background contribution from Standard Model processes, for this reason it is sometimes called the *golden* signature. This property allows to search for SUSY using only muons for selection without need for requirements on jets and MET, which are prone to experimental uncertainties in the first years of LHC running. In the low mass SUSY region more than 90% of the neutralino-chargino pairs are produced in decays of gluinos and squarks, since the squark and gluino production carries the major fraction of the SUSY cross section. The direct neutralino-chargino production contributes less than 10%. A distinctive feature of the trimuon signature is the kinematical edge in the invariant mass spectrum of muons from neutralino decays at $M_{\mu\mu}^{\max} = m_{\chi_2^0} - m_{\chi_1^0}$.

There are two types of background processes for the trimuon SUSY search. On the one hand one has the background contribution from three prompt muons in the SM diboson production (ZW, ZZ) followed by leptonic boson decays. This background can be reduced by requiring $M_{\mu\mu} < M_Z$. On the other hand backgrounds including fake muons can be reduced by requiring muons to be strongly isolated from jet activity and associated with the primary vertex. Selecting a reference sample of prompt muons from the Z +jets production and a reference sample of fake muons from QCD processes allows to check the detector performance with respect to muon isolation and vertex reconstruction of prompt and fake muons. With the cuts described in Section 5.4.4 a purity of $\sim 0.8(1.4) \times 10^{-4}$ has been obtained for fake muons in the prompt sample (prompt muons in the fake sample).

With an accumulated luminosity as small as $\mathcal{L}_{acc} = 200 \text{ pb}^{-1}$ the final trimuon selection at the SUSY benchmark point LM0 ($m_0 = 200 \text{ GeV}$, $m_{1/2} = 160 \text{ GeV}$, $\tan\beta = 10$, $A_0 = -400$, $\mu > 0$) results in

- 15 events from SUSY production
- 3 events from SM diboson production
- 6 events from SM processes with fake muons,

where the Z/γ^* +jets production forms 95% of the fake background processes. The remaining 5% originate from the $t\bar{t}$ production. Data-driven methods have been developed to control the SM background contribution after the final trimuon event selection: i) the Z -candle method estimates the SM diboson contribution from the number of events in the Z -peak using a MC correction factor and ii) the ABCD method extrapolates the contribution of the backgrounds with fake muons from the sidebands in the 2-dimensional distribution of the isolation and impact parameter to the signal region. Using the selected fake reference sample the performance of the ABCD method can be checked with data for fake muons from QCD events. The contamination from SUSY signal in the sidebands of the ABCD method as well as from SUSY signal and fake backgrounds in the Z -peak result in a small overestimation of $\sim 16\%$. The uncertainty of the data-driven methods is dominated by the extrapolated statistical error from the sidebands, which is $\sim 35\%$ for the luminosity of $\mathcal{L}_{acc} = 200 \text{ pb}^{-1}$ considered in this thesis.

Applying the trimuon selection to other points of the SUSY parameter space allows to determine the discovery reach of the trimuon SUSY search. In order to compare the discovery reach of the trimuon search at the LHC with the exclusion limits obtained with the searches for trileptons at the Tevatron, the SUSY parameters $\tan\beta = 3$, $A_0 = 0$ and $\mu > 0$ have been chosen. The m_0 - $m_{1/2}$ plane in the range $m_0 = [0, 300]$ GeV and $m_{1/2} = [150, 300]$ GeV has been divided into 450 points and 10000 events for each point have been simulated with the fast simulation of the CMS detector, which has been validated with the full simulation. For large branching ratios of gauginos to muon final states (i.e. small m_0) gluino masses up to 600(700) GeV can be discovered with 5 sigma significance for $\mathcal{L}_{acc} = 200(500) \text{ pb}^{-1}$ as can be deduced from Fig. 5.38 using the relation $m_{\tilde{g}} = 2.7m_{1/2}$. Hence, already after the first year of LHC the trimuon SUSY search reaches a similar sensitivity as the Tevatron experiments, where the trilepton signature from direct neutralino-chargino production ($p\bar{p} \rightarrow \chi_2^0\chi_1^\pm$) has been intensively searched for with an accumulated luminosity of $\mathcal{L}_{acc} = 2000 \text{ pb}^{-1}$.

Appendix A

Track Reconstruction Performance

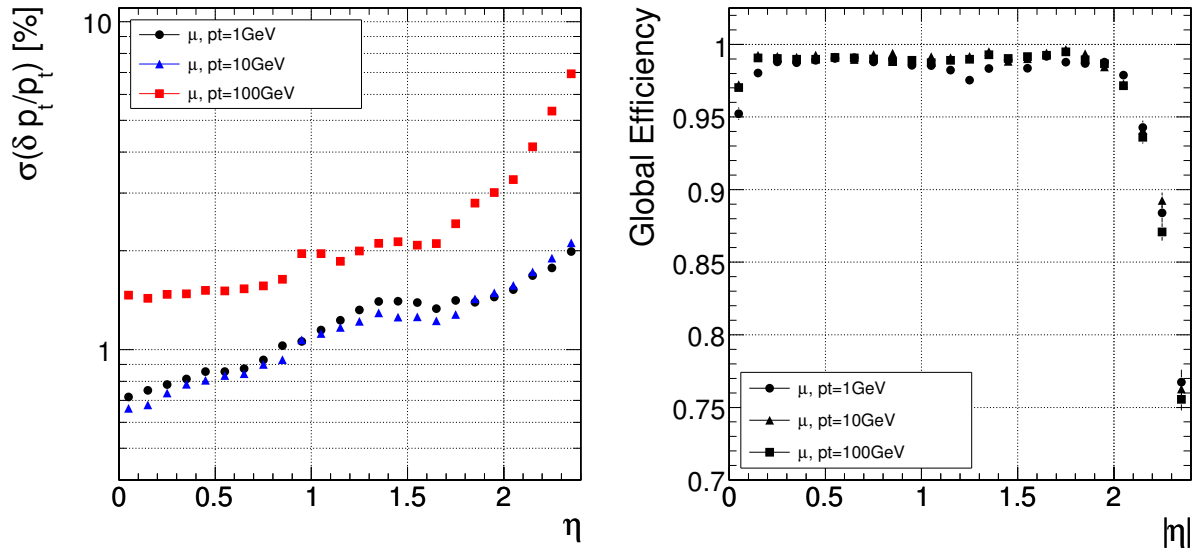


Figure A.1: The track resolution (L) as well as the track reconstruction efficiency (R) as a function of PT of single muons with $PT = 1$ GeV, $PT = 10$ GeV and $PT = 100$ GeV [60]. The track resolution is excellent ($< 2\%$) for low momentum muons. The tracking system offers high efficiencies $\sim 98\%$ also for low momentum particles, which is essential for the muon identification, since muons are identified by the track activity around the muon track (isolation). The efficiency drops in pseudorapidity region $|\eta| > 2$.

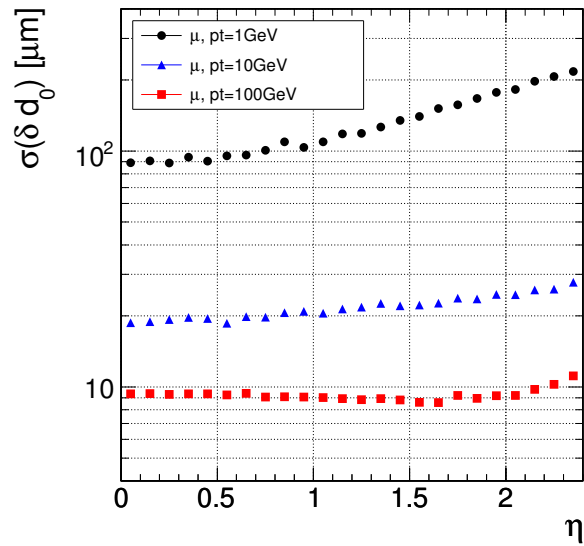


Figure A.2: The impact parameter resolution as a function of PT of single muons with $PT = 1 \text{ GeV}$, $PT = 10 \text{ GeV}$ and $PT = 100 \text{ GeV}$ [60]. The vertex position is determined with an excellent resolution of $\sim 20 \mu\text{m}$ for muons with $PT = 10 \text{ TeV}$ and $\sim 10 \mu\text{m}$ for muons with $PT = 100 \text{ TeV}$.

Appendix B

SUSY Particle Decay Modes

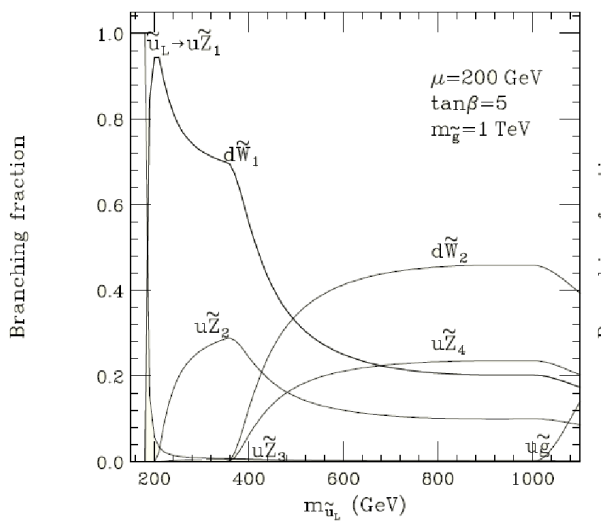


Figure B.1: The decay modes of left-handed squarks [4]. The decay to the lightest chargino and next-to-lightest neutralino dominates at small squark masses. At larger squark masses, the branching fraction to heavier gauginos increases.

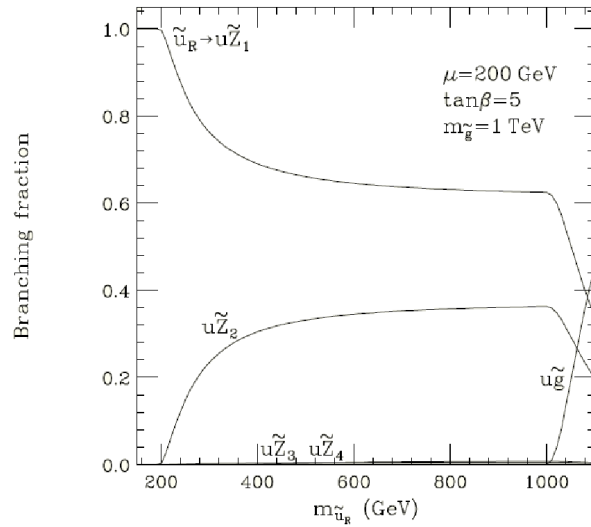


Figure B.2: The decay modes of right-handed squarks [4]. The decay to the lightest neutralino dominates. At larger squark masses, the branching fraction to the next-to-lightest neutralino increases.

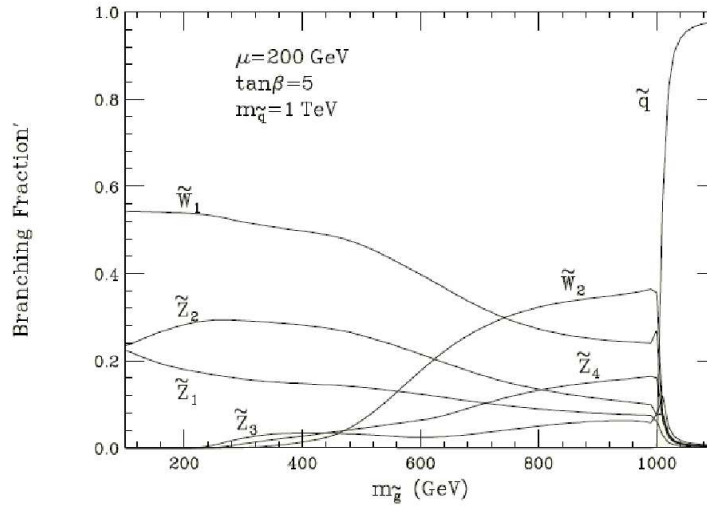


Figure B.3: The decay modes of gluinos to gaugino and squark pairs [4]. The decay to the lightest chargino is dominant, followed by the decay to the next-to-lightest neutralino. For larger gluino masses the contribution to heavy gauginos increases.

Bibliography

- [1] **ATLAS** Collaboration, “ATLAS: Technical proposal for a general-purpose pp experiment at the Large Hadron Collider at CERN,” CERN-LHCC-94-43.
- [2] **CMS** Collaboration, R. Adolphi et al., “The CMS experiment at the CERN LHC,” *JINST* **0803** S08004, doi:10.1088/1748-0221/3/08/S08004, 2008.
- [3] **Particle Data Group** Collaboration, C. Amsler et al., “Review of particle physics,” *Phys. Lett.* **B667** doi:10.1016/j.physletb.2008.07.018, 2008.
- [4] H. Baer and X. Tata, “Weak scale supersymmetry: From superfields to scattering events”, Cambridge University Press, 2006.
- [5] **WMAP** Collaboration, G. Hinshaw et al., “Five-Year Wilkinson Microwave Anisotropy Probe (WMAP) Observations:Data Processing, Sky Maps, Basic Results,” *Astrophys. J. Suppl.* **180** 225–245, arXiv:0803.0732, 2009.
- [6] H. Nilles, “Supersymmetry, Supergravity and Particle Physics,” *Phys. Rept.* **110** 1–162, doi:10.1016/0370-1573(84)90008-5, 1984.
- [7] S. Martin, “A Supersymmetry Primer,” arXiv:hep-ph/9709356, 1997.
- [8] I. Aitchison, “Supersymmetry and the MSSM: An Elementary introduction,” arXiv:hep-ph/0505105, 2005.
- [9] W. de Boer, “Grand Unified Theories and Supersymmetry in Particle Physics and Cosmology,” *Progress in Particle and Nuclear Physics* **33** 201, arXiv:hep-ph/9402266, 1994.
- [10] M. Drees, “An Introduction to supersymmetry,” arXiv:hep-ph/9611409, 1996.
- [11] H. Haber and M. Schmitt, “Supersymmetry: in Review of Particle Physics,” *Eur. Phys. J.* **C3** 743–762, 1998.
- [12] U. Amaldi, W. de Boer, and H. Fuerstenau, “Comparison of grand unified theories with electroweak and strong coupling constants measured at LEP,” *Phys. Lett.* **B260** 447–455, doi:10.1016/0370-2693(91)91641-8, 1991.

- [13] **CDF** Collaboration, “Search for Supersymmetry in ppbar Collisions at $\sqrt{s}=1.96$ TeV Using the Trilepton Signature for Chargino-Neutralino Production,” *Physical Review Letters* **101** 251801, 2008.
- [14] **D0** Collaboration, “Search for associated production of charginos and neutralinos in the trilepton final state using 2.3 fb⁻¹ of data,” *Physics Letters B* **680** 34, 2009.
- [15] **CMS** Collaboration, W. de Boer, M. Niegel, et al., “Trilepton final state from neutralino chargino production,” CERN-CMS-NOTE-2006-113, 2006.
- [16] **CMS** Collaboration, “Alignment of the CMS Silicon Tracker during Commissioning with Cosmic Rays,” arXiv:0910.2505, 2009.
- [17] **CMS** Collaboration, “Performance Study of the CMS Barrel Resistive Plate Chambers with Cosmic Rays,” arXiv:0911.4045, 2009.
- [18] **CMS** Collaboration, “Time Reconstruction and Performance of the CMS Electromagnetic Calorimeter,” arXiv:0911.4044, 2009.
- [19] **CMS** Collaboration, “Alignment of the CMS Muon System with Cosmic-Ray and Beam-Halo Muons,” arXiv:0911.4022, 2009.
- [20] **CMS** Collaboration, “Precise Mapping of the Magnetic Field in the CMS Barrel Yoke using Cosmic Rays,” arXiv:0910.5530, 2009.
- [21] M. Kobayashi and T. Maskawa *Prog. Theor. Phys.* **49** 652, 1973.
- [22] C. Yang and R. Mills, “Conservation of isotopic spin and isotopic gauge invariance,” *Phys. Rev.* **96** 191–195, doi:10.1103/PhysRev.96.191, 1954.
- [23] M. Gell-Mann, “Symmetries of baryons and mesons,” *Phys. Rev.* **125** 1067–1084, doi:10.1103/PhysRev.125.1067, 1962.
- [24] V. Barnes et al., “Observation of a Hyperon with Strangeness -3,” *Phys. Rev. Lett.* **12** 204–206, doi:10.1103/PhysRevLett.12.204, 1964.
- [25] E. Fermi *Z. Phys.* **88** 161, 1932.
- [26] **UA1** Collaboration, G. Arnison et al., “Experimental observation of lepton pairs of invariant mass around 95GeV at the CERN SPS collider,” *Phys. Lett.* **B126** 398–410, doi:10.1016/0370-2693(83)90188-0, 1983.
- [27] **UA1** Collaboration, G. Arnison et al., “Experimental observation of isolated large transverse energy electrons with associated missing energy,” *Phys. Lett.* **B122** 103–116, 1983.
- [28] C. Wu et al., “Experimental Test Of Parity Conservation In Beta Decay,” *Phys. Rev.* **105** 1413–1414, doi:10.1103/PhysRev.105.1413, 1957.

- [29] S. Glashow *Nucl. Phys.* **22** 579, 1961.
- [30] A. Salam *Phys. Rev.* **127** 331., 1962.
- [31] S. Weinberg *Phys. Rev. Lett.* **19** 1264, 1967.
- [32] P. Higgs, “Broken symmetries, massless particles and gauge fields,” *Phys. Lett.* **12** 132–133, doi:10.1016/0031-9163(64)91136-9, 1964.
- [33] F. Jegerlehner and A. Nyffeler, “The Muon g-2,” *Phys. Rept.* **477** 1–110, arXiv:0902.3360, 2009.
- [34] **Super-Kamiokande** Collaboration, Y. Fukuda et al., “Evidence for oscillation of atmospheric neutrinos,” *Phys. Rev. Lett.* **81** 1562–1567, arXiv:hep-ex/9807003, doi:10.1103/PhysRevLett.81.1562, 1998.
- [35] W. Marciano, “Proceedings of the 8th Workshop on Grand Unification”, New York, 1987.
- [36] D. Kazakov, “Beyond the Standard Model (In search of Supersymmetry)”, 2001.
- [37] C. Sander, “Interpretation des Ueberschusses in diffuser galaktischer Gamma-Strahlung oberhalb 1GeV als Annihilationssignal dunkler Materie”, 2005.
- [38] L. Alvarez-Gaume, J. Polchinski, and M. B. Wise, “Minimal Low-Energy Supergravity,” *Nucl. Phys.* **B221** 495, doi:10.1016/0550-3213(83)90591-6, 1983.
- [39] **Muon g-2 Collaboration** Collaboration, G. W. Bennett and B. Bousquet, “Final report of the E821 muon anomalous magnetic moment measurement at BNL,” *Physical Review D* **73** no. 7, doi:10.1103/PhysRevD.73.072003, 2006.
- [40] **BABAR** Collaboration, “The BaBar detector,” *Nucl. Instrum. Meth.* **A479** 1–116, arXiv:hep-ex/0105044, 2002.
- [41] **CLEO** Collaboration, “The CLEO Detector,” *Nucl. Instr. Meth.* **211** 47, doi:10.1016/0167-5087(83)90556-2, 1983.
- [42] **Belle** Collaboration, “The Belle detector,” *Nucl. Instrum. Meth.* **A479** 117–232, doi:10.1016/S0168-9002(01)02013-7, 2002.
- [43] A. V. Gladyshev and D. I. Kazakov, “Supersymmetry and LHC,” *Phys. Atom. Nucl.* **70** 1553–1567, arXiv:hep-ph/0606288, 2007.
- [44] **CDMS** Collaboration, Z. Ahmed et al., “Search for Weakly Interacting Massive Particles with the First Five-Tower Data from the Cryogenic Dark Matter Search at the Soudan Underground Laboratory,” *Phys. Rev. Lett.* **102** 011301, arXiv:0802.3530, 2009.

- [45] **XENON** Collaboration, E. e. a. Aprile, “XENON: A 1-tonne liquid xenon experiment for a sensitive dark matter search,” [arXiv:astro-ph/0207670](https://arxiv.org/abs/astro-ph/0207670), 2002.
- [46] J. Gascon, “Direct Dark Matter Searches and the EDELWEISS-II Experiment,” [arXiv:0906.4232](https://arxiv.org/abs/0906.4232), 2009.
- [47] “LEP Supersymmetry Working Group, ALEPH, DELPHI, L3, and OPAL experiments,” Technical Report LEPSUSYWG/02-06.2, CERN, 2002. <http://lepsusy.web.cern.ch/lepsusy/Welcome.html>.
- [48] **D0** Collaboration, “Search for squarks and gluinos in events with jets and missing transverse energy using 2.1 fb⁻¹ of ppbar collision data at sqrt(s)=1.96 TeV,” *Physics Letters B* **660** 449, 2008.
- [49] **CDF** Collaboration, “Inclusive Search for Squark and Gluino Production in ppbar Collisions at sqrt(s)=1.96 TeV,” *Physical Review Letters* **102** 121801, 2009.
- [50] **ALEPH** Collaboration, “ALEPH: technical report”, Technical Design Report CMS, CERN, 1983.
- [51] **DELPHI** Collaboration, “DELPHI: technical proposal,” Technical Report CERN-LEPC-83-3. DELPHI-83-66. LEPC-P-2, CERN, Geneva, 1983.
- [52] **L3** Collaboration, “Technical proposal: L3,” Technical Report CERN-LEPC-83-5. LEPC-P-4, CERN, Geneva, 1983.
- [53] **OPAL** Collaboration, “The OPAL detector: technical proposal,” Technical Report CERN-LEPC-83-4. LEPC-P-3, CERN, Geneva, 1983.
- [54] **D0** Collaboration, “The Upgraded D0 Detector,” *Nucl. Instrum. Meth.* **A565** 463–537, [arXiv:physics/0507191](https://arxiv.org/abs/physics/0507191), 2006.
- [55] **CDF** Collaboration, F. Abe et al., “The CDF detector: an overview,” *Nucl. Instr. Meth.* **A271** 387–403, doi:10.1016/0168-9002(88)90298-7, 1988.
- [56] <http://press.web.cern.ch/press/PressReleases/Releases2009/PR13.09E.html>.
- [57] **LHCb** Collaboration, “LHCb : Technical Proposal”, Tech. Proposal, CERN, 1998.
- [58] **ALICE** Collaboration, “ALICE: Technical proposal for a Large Ion collider Experiment at the CERN LHC”, LHC Tech. Proposal, CERN, 1995.
- [59] <http://bigscience.web.cern.ch/bigscience/en/lhc/lhc2.html>.
- [60] **CMS** Collaboration, “CMS physics”, Technical Design Report CMS, CERN, 2006.
- [61] <http://cms.web.cern.ch/cms/Detector/FullDetector/index.html>.

- [62] D. Kotlinski, “The design of the CMS pixel detector system,” *Nucl. Instrum. Methods Phys. Res., A* **477** no. 1-3, 446–50, 2002.
- [63] **CMS** Collaboration, “The CMS tracker system project”, Technical Design Report CMS, CERN, 1997.
- [64] **CMS** Collaboration, “The CMS electromagnetic calorimeter project”, Technical Design Report CMS, CERN, 1997.
- [65] **CMS** Collaboration, V. Adzic et al., “Energy Resolution of the Barrel of the CMS Electromagnetic Calorimeter,” Technical Report CMS-NOTE-2006-148, CERN, 2006.
- [66] **CMS** Collaboration, “The Hadron Calorimeter”, Technical Design Report CMS, CERN, 1997.
- [67] C. Kerem et al., “CMS HCAL installation and commissioning”, Conf. Ser.160 012055 (8pp), J. Phys., 2009.
- [68] **CMS** Collaboration, “The Magnet Project”, Technical Design Report CMS, CERN, 1997.
- [69] **CMS** Collaboration, “The CMS muon project”, Technical Design Report CMS, CERN, 1997.
- [70] **CMS** Collaboration, “CMS TriDAS project: The trigger systems”, Technical Design Report CMS, CERN, 1997.
- [71] V. Buege, “Virtualisation of Grid Resources and Prospects of the Measurement of Z Boson Production in Association with Jets at the LHC”, Vdm Verlag, 2008.
- [72] **CMS** Collaboration, “CMS computing”, Technical Design Report CMS, CERN, 2005.
- [73] R. Brun et al., “ROOT: An Object-Oriented Data Analysis Framework: Users Guide 5.16”, 2007.
- [74] C. Jones et al., “The new CMS Event Data Model and Framework,” in *Proceedings of the CHEP06 Conference*. CERN, Mumbai, India, 2006.
- [75] K. Amako et al., “Geant4 and its validation,” *Nuclear Physics B - Proceedings Supplements* **150** 44–49, doi:10.1016/j.nuclphysbps.2004.10.083, 2006.
- [76] M. Mangano et al., “ALPGEN, a generator for hard multiparton processes in hadronic collisions,” *JHEP* **07** 001, arXiv:hep-ph/0206293, 2003.
- [77] S. Catani, F. Krauss, R. Kuhn, and B. R. Webber, “QCD Matrix Elements + Parton Showers,” *JHEP* **11** 063, arXiv:hep-ph/0109231, 2001.

- [78] T. Sjostrand et al., “Pythia 6.3 physics and manual,” `arXiv:hep-ph/0308153`, 2003.
- [79] F. Maltoni and T. Stelzer, “MadEvent: Automatic event generation with MadGraph,” *JHEP* **02** 027, `arXiv:hep-ph/0208156`, 2003.
- [80] T. Gleisberg et al., “SHERPA 1.alpha, a proof-of-concept version,” *JHEP* **02** 056, `arXiv:hep-ph/0311263`, 2004.
- [81] F. Krauss, R. Kuhn, and G. Soff, “AMEGIC++ 1.0: A Matrix element generator in C++,” *JHEP* **02** 044, `arXiv:hep-ph/0109036`, 2002.
- [82] F. Krauss et al., “APACIC++ 2.0: A Parton cascade in C++,” *Comput. Phys. Commun.* **174** 876–902, `arXiv:hep-ph/0503087`, 2006.
- [83] M. Merschmeyer and M. Niegel, “The SherpaInterface of the CMS Software Framework”. <https://twiki.cern.ch/twiki/bin/view/CMS/SherpaInterface>.
- [84] B. Allanach, “SOFTSUSY: A C++ program for calculating supersymmetric spectra,” *Comput. Phys. Commun.* **143** 305–331, `arXiv:hep-ph/0104145`, 2002.
- [85] A. Djouadi and M. Muhlleitner, M. and Spira, “Decays of Supersymmetric Particles: the program SUSY-HIT (SUSpect-SdecaY-Hdecay-InTerface),” *Acta Phys. Pol. B* **38** no. hep-ph/0609292. CERN-PH-TH-2006-200, 635–644. 8 p, 2006.
- [86] T. Gleisberg et al., “Event generation with SHERPA 1.1,” *JHEP* **02** 007, `arXiv:hep-ph/0811.4622`, 2009.
- [87] R. Kalman, “A New Approach to Linear Filtering and Prediction Problems,” *Journal of Basic Engineering* **82** 35–45, 1960.
- [88] **CMS** Collaboration, “Jet energy calibration with photon+jet events,” JME-09-004, 2009.
- [89] **CMS** Collaboration, “Plans for Jet Energy Corrections at CMS,” JME-07-002, 2007.
- [90] **CMS** Collaboration, “Jet energy correction using Z to mumu Jet PT balance,” JME-09-009, 2009.
- [91] **CMS** Collaboration, “Performance of missing ET reconstruction,” JME-07-001, 2007.
- [92] S. Abdullin et al., “GARCON: Genetic algorithm for rectangular cuts optimization. User’s manual for version 2.0,” `arXiv:hep-ph/0605143`, 2006.

- [93] S. Abdullin, “Genetic algorithm for SUSY trigger optimization in CMS detector at LHC,” *Nucl. Instrum. Meth.* **A502** 693–695, doi:10.1016/S0168-9002(03)00546-1, 2003.
- [94] J. Holland, “Adaptation in natural and artificial systems”, The University of Michigan Press, Ann Arbor, 1975.
- [95] D. Goldberg, “Genetic algorithms in search, optimization and machine learning”, Addison Wesley, 1989.
- [96] D. Piparo, G. Schott, and G. Quast, “RooStatsCms: a tool for analysis modelling, combination and statistical studies,” arXiv:0905.4623, 2009.
- [97] R. Cousins et al. *Nucl. Inst. Meth. Phys. Res. A* **595** 480, doi:10.1016/j.nima.2008.07.086, 2008.
- [98] W. Beenakker, “Squark and gluino production at hadron colliders,” *Nucl. Phys.* **B492** 51–103, arXiv:hep-ph/9610490, 1997.
- [99] W. Beenakker et al., “The Production of charginos, neutralinos and sleptons at hadron colliders,” *Phys. Rev. Lett.* **83** 3780–3783, arXiv:hep-ph/9906298, 1999.
- [100] H. Baer, “Supersymmetry at the Large Hadron Collider”, 2007, Lectures at the SUSY07 conference.
- [101] CMS Collaboration, “CMS physics”, Technical Design Report CMS, CERN, 2006.
- [102] U. Blumenschein, “Suche nach assoziierter Chargino-Neutralino Produktion in Proton-Antiproton Kollisionen bei 1.96TeV”, 2005.
- [103] U. Baur, T. Plehn, and D. Rainwater, “Determining the Higgs Boson Self Coupling at Hadron Colliders,” *Physical Review D* **67** 033003, 2003.
- [104] G. Salam, “Fall and rise of the gluon splitting function,” *Int. J. Mod. Phys.* **A20** 4450–4455, arXiv:hep-ph/0407368, 2005.
- [105] ALEPH Collaboration, A. Heister et al., “A measurement of the gluon splitting rate into c anti-c pairs in hadronic Z decays,” *Phys. Lett.* **B561** 213–224, arXiv:hep-ex/0302003, 2003.
- [106] SLD Collaboration, K. Abe et al., “Improved measurement of the probability for gluon splitting into b anti-b in Z0 decays,” *Phys. Lett.* **B507** 61–69, arXiv:hep-ex/0102002, 2001.
- [107] CMS Collaboration, W. Erdmann, “Vertex reconstruction at the CMS experiment,” *J. Phys. Conf. Ser.* **110** 092009, doi:10.1088/1742-6596/110/9/092009, 2008.

- [108] C. Saout, “Impact of Tracker Misalignment on the CMS b-Tagging Performance”, Talk at LHC Det. Alignment Workshop, 2009.
- [109] M. Cepeda et al., “Data Driven Methods for QCD Background Estimation in Electroweak muon analysis: the ABCD and the Template methods”, CMS AN2008/113, 2008.
- [110] S. Frixione and B. Webber, “Matching NLO QCD computations and parton shower simulations,” [arXiv:0204244](https://arxiv.org/abs/0204244), 2002.

List of Figures

2.1	Higgs potential	14
2.2	Unification of the coupling constants	20
2.3	SUSY constraints from WMAP	31
2.4	LEP SUSY constraints	32
2.5	Tevatron SUSY constraints from squark-gluino searches	33
2.6	Tevatron constraints from trilepton searches	33
3.1	CERN accelerator complex	37
3.2	Compact Muon Solenoid experiment	38
3.3	Measurement of particles in different subsystems	40
3.4	Layout of the CMS tracking system	41
3.5	Layout of the electromagnetic calorimeter	43
3.6	Layout of the hadron calorimeter	44
3.7	Layout of the muon system	45
3.8	Design of the CMS L1-Trigger	47
3.9	Illustration of the Tier structure	48
4.1	CMS software event model	50
4.2	Event seen from the perspective of MC event generators	52
4.3	Global muon reconstruction efficiency	53
4.4	Jet transverse energy resolution	54
4.5	Jet energy scale uncertainty	55
4.6	Resolution of the missing transverse energy	56
5.1	Gluino and squark production	60
5.2	Direct neutralino-chargino pair production	61
5.3	Total SUSY cross section and cross section fractions of SUSY channels	62
5.4	Three-body decays of gluinos to neutralinos and charginos	63
5.5	Three-body decays of neutralinos to muon final states	64
5.6	Three-body decays of charginos to muon final states	64
5.7	Gaugino decay modes to leptons in the mSUGRA plane	65
5.8	Transverse momentum of muons from two-body neutralino decays to sleptons	66
5.9	Dimuon invariant mass distribution of muons from neutralino decays	67

5.10	Cross section fraction of several muon multiplicity final states	68
5.11	Contribution of different SUSY channels to the trimuon signature	69
5.12	Jet multiplicity for gaugino and gluino-squark production	70
5.13	Diagrams for the trimuon production	70
5.14	Kinematics of muons and jets for the SUSY and SM trimuon production	72
5.15	Observables for the SUSY and SM trimuon production	73
5.16	Diagrams for the ZW and ZZ diboson production	74
5.17	Diagrams for the Z +jets production	74
5.18	Diagrams for the $t\bar{t}$ production	75
5.19	Diagrams for the W +jets production	75
5.20	Muon selection efficiency for the track quality criteria	79
5.21	PT - η distribution of prompt muons from SUSY and Z +jets	79
5.22	Diagrams for heavy flavor production	80
5.23	PT distribution of fake muons for different generators	81
5.24	Distribution of parameters used for the prompt sample selection	85
5.25	Distribution of parameters used for the fake sample selection	86
5.26	Distribution of relative isolation and impact parameter significance	88
5.27	Efficiency, significance and sensitivity of muon selection variables	89
5.28	Optimization of PT selection	91
5.29	Efficiency of the final muon selection	92
5.30	Invariant mass after the selection of two tight muons plus one quality muon	93
5.31	Invariant mass after the final trimuon selection	95
5.32	Sketch of the different regions used for the ABCD method	100
5.33	Validity of the ABCD method for the fake reference sample	102
5.34	Validity of the ABCD method for the trimuon analysis	103
5.35	Number of events in ABCD regions	104
5.36	Validity of the ABCD method for the trimuon analysis without SUSY	105
5.37	MC correction factor for the Z -candle method	107
5.38	SUSY trimuon 5σ discovery reach	110
5.39	Branching ratio of neutralino decays to muons	111
5.40	HT and MET after the selection of two tight muons plus one quality muon	112
5.41	SUSY trimuon+ HT 5σ discovery reach	113
5.42	SUSY model dependence of jet energy and missing energy	114
A.1	Track resolution and reconstruction efficiency	119
A.2	Impact parameter resolution	120
B.1	Decay modes of left-handed squarks	121
B.2	Decay modes of right-handed squarks	122
B.3	Decay modes of gluinos	122

List of Tables

2.1	Particle spectrum of the Standard Model	8
2.2	Particle spectrum of the MSSM	23
5.1	SUSY and SM background data samples and cross sections	76
5.2	Selection criteria and results for the prompt reference sample	84
5.3	Selection criteria and results for the fake reference sample	87
5.4	Final muon selection	91
5.5	Statistics for the final trimuon event selection for SUSY and SM backgrounds	92
5.6	Final trimuon event selection	94
5.7	Statistics for the final trimuon event selection for additional QCD samples	96
5.8	Trigger efficiency	97
5.9	Summary of systematic uncertainties	99
5.10	Results for the ABCD and Z -candle method	108
5.11	Summary of data-driven estimation	108
5.12	Statistics for the trimuon selection with HT and MET	112

Acknowledgments

I am heartily thankful to my supervisor, Prof. Dr. Wim de Boer, whose encouragement, guidance and support from the initial level enabled me to develop an understanding of the subject.

I would also like to thank Prof. Dr. Guenter Quast for both co-supervising this thesis and his continuous dedication in providing computing power for every student.

It is a pleasure to me to thank Dr. Valery Zhukov. Without his work and advice this thesis would not have been possible.

My friend and colleague Dr. Altan Cakir deserves special mention for supporting and accompanying me on my way through the dissertation during the last years, for fruitful discussions about physics and for the gorgeous atmosphere in the office.

Additionally I would like to thank Markus Bensch, Daniel Troendle, Eva Ziebarth, Tim Hanisch, Dr. Iris Gebauer, Daniel Stricker, Daniel Daeuwel, Sabine Reisser, Dr. Christian Sander for the friendly and productive atmosphere in our working group.

I would like to thank Dr. Valery Zhukov, Dr. Jan Lueck, Dr. Altan Cakir, Dr. Julia Bauer, Eva Ziebarth, Tim Hanisch and Jens Stricker for carefully reading and commenting on this manuscript.

Last, but of course not least, I would like to thank my friends and my family for their help and support.